January 2013

Static and Dynamic Components of Droplet Friction

Peter Robert Griffiths
University of South Florida, prgriffiths@mail.usf.edu

Static and Dynamic Components of Droplet Friction

by

Peter R. Griffiths

A thesis submitted in partial fulfillment
of the requirements for the degree of
Master of Science in Mechanical Engineering
Department of Mechanical Engineering
College of Engineering
University of South Florida

Major Professor: Nathan Crane, Ph.D.
Nathan Gallant, Ph.D.
Rasim Guldiken, Ph.D.

Date of Approval:
November 14, 2013

Keywords: digital microfluidics, contact line, contact angle, hysteresis

DEDICATION

To my father, who helped guide me onto the path of engineering and to the rest of my family who put up with the two of us.

"Learn as if you were to live forever."

~ Mahatma Gandhi

ACKNOWLEDGMENTS

There were multiple people who without their help, this thesis would not have been possible. I would like to take the time to acknowledge them here:

Jose Carballo prepared some of the cover slips used in the testing as well assisted in the video setup on several runs. He was also very helpful on multiple occasions listening and providing feedback when I encountered difficulty.

Professors Nathan Gallant and Rasim Guldiken served on my thesis committee and provided me with very helpful comments and insights to help further expand upon my research and conclusions.

Qi Ni created LabView program used to collect the test data and prepared the majority of the cover slips and all the substrates used in testing. He also did the extreme difficult task of attaching the glass fiber to the sensor. This thesis is built upon his earlier work measuring the force on droplets using the same setup and equipment and he was instrumental in developing the test plan and the initial procedure used. He helped get me up to speed in an area I had no previous experience and past many road blocks through many conversations and by sending me several papers.

Professor Nathan Crane was kind enough to allow me to work in his research group and to build upon previous work which led to this thesis. I very much appreciated his kindness, patience and support when setbacks occurred in testing and while gaining a knowledge base in this subject. His keen perspectives on how data and conclusions should be presented were very helpful in changing my presentation to more an academic tone.

TABLE OF CONTENTS

LIST OF TABLES

LIST OF FIGURES

ABSTRACT

As digital microfluidics has continued to mature since its advent in the early 1980's, an increase in new and novel applications of this technology have been developed. However, even as this technology has become more common place, a consensus on the physics and force models of the motion of the contact line between the fluid, substrate, and ambient has not been reached. This uncertainty along with the dependence of the droplet geometry on the force to cause its motion has directed much of the research at specific geometries and droplet actuation methods.

The goal of this thesis is to help characterize the components of the friction force which opposes droplet motion as a one dimensional system model based upon simple system parameters independent from the actuation method. To this end, the force opposing the motion of a droplet under a thin rectangular glass cover slip was measured for varying cover slip dimensions (widths, length), gap height between the cover slip and substrate, and bulk droplet velocity. The stiffness of the droplet before droplet motion began, the force at which the motion initiated, and the steady-state force opposing the droplet motion were measured. The data was then correlated to hypothesized equations and compared to simple models accounting for the forces due to the contact angle hysteresis, contact line friction, and viscous losses.

It was found that the stiffness, breakaway force, and steady-state force of the droplet could be correlated to with an error standard deviation of 8 %, 14%, and 10 % respectively. Much of the error was due to an unexpected height dependence for the breakaway and steady-state forces and testing error associated with the velocity. The models for the stiffness and breakaway force over predicted the results by 36% and 16% respectively. During testing, stability issues with the cover slip were observed and simple dye testing was conducted to visualize the droplet flow field.

INTRODUCTION

Motivation

In recent years the increased interest in digital microfluidic systems for multiple applications has led to a growth in research and development in this field. One of the challenges that face users of this technology is that the forces evolved are largely dependent upon the geometry of the droplets. Because of this, much of the research and modeling of these systems have been focused on specific geometries and the relevant force data is often tied to these configurations. As new and novel ways of utilizing this technology becomes more prevalent, simplified models of the droplet forces, broken down into components which are applicable to multiple geometries and configurations would assist in the design of digital microfluidic systems.

Background

Digital Microfluidics

Microfluidics is a regime of fluid dynamics in which the small scale of the system leads to surface tension forces becoming dominant over pressure, inertia, and body forces [1, 2]. Digital microfluidics is a subset of microfluidics in which discrete droplets are utilized instead of continuous flows [1, 3]. Using discrete droplets allows for the precise manipulation of fixed volumes of fluids [3, 4, 1] and by utilizing surface tension control techniques, the absence of moving mechanical controls which are complex and costly at the relevant size scales [1, 4].

Applications

One of the first applications of digital microfluidics in the 1980's was the inkjet printer [5]. Since then, the prime driver of microfluidic development has been the biotechnology field [5] with one of the most well-known developments being Lab-on-Chip technology [6]. As the technology has continued to expand and mature, newer and more diverse applications have been developed. The small size scale lends itself to MEMS applications. One such technology is Self-assembly, such as the positioning of silicon dies used in the manufacturing of computer chips using capillary forces [7]

Droplet Actuation

Several different surface tension control and droplet actuation methods have been developed. Thermocapillary pumping uses the inverse relationship between surface tension and temperature to cause droplet motion [1, 6, 4]. Photochemical pumping utilizes liquids which have a relationship between surface tension and light exposure [1, 6]. Most commonly, electrowetting uses the reduction in interfacial tension in the presence of an electrical field to cause droplet motion [1, 3, 6, 8]. All of these techniques utilize a decrease in the surface tension at one point to cause a surface tension gradient resulting in droplet motion [2, 4].

Forces

Contact Line Friction

Contact line friction is the most important [2] yet is the least understood of the forces involved in droplet motion [1, 9]. Contact line friction refers to the force that arises due to the absorption and desorption processes that occur at the moving contact line [6, 10]. Several proposed mechanisms exist to explain the motion of the contact line, the resulting friction force, and how it relates to the droplet bulk velocity [9, 10, 11, 12]. The two main theories are the Hydrodynamic and Molecular-kinetic theories. In general, the differing models all relate through differing mechanism the dynamic contact angle to the static equilibrium contact angles [9]. The general empirically derived expressed for this is [13]:

$$\theta_{dyn} = \theta_{st} + \left(\frac{U}{C}\right)^{1/m} \tag{1}$$

where θ_{dyn} is the dynamic contact angle, θ_{st} is the static contact angle, and U and m are constants. The force required to move the contact line per unit width is then [9]:

$$\frac{F_{CL}}{w} = \gamma\left(\cos\theta_{st} - \cos\theta_{dyn}\right) \tag{2}$$

Often equations (1) and (2) are combined in to a simplified linear representation for the contact line friction of a droplet [1]:

$$\frac{F_{CL}}{w} = A + BU \tag{3}$$

where A is the contribution due to the difference in advancing and receding contact angles and B is the friction constant.

Wall Shear

Depending upon the system parameters, the viscous loss due to shear at the walls can contribute to the overall droplet friction force [2, 1]. This typically presents a challenge to accurately predicting these forces as the internal flow of the droplet is not usually known [6] and the stick-slip motion of the contact line makes analytical models using typical methods difficult [1]. The usual work around is to use approximations of the shear force based upon the velocity profiles with zero slip boundary conditions for similar geometries [1]. An approximation of the velocity gradient at the substrate is made assuming it to be proportional to the bulk velocity divided by the droplet height [1, 4]. However the model predictions from this technique often show poor results when compared to empirical results for even simple geometries [6].

External Drag

Depending upon the ambient surrounding the droplet, the external drag due to the motion of the droplet through the ambient can also contribute to the droplet friction force [6]. This force is typically modeled by approximating the droplet as a shape with well documented drag correlations or models [1].

Contact Angle Hysteresis

Contact angle hysteresis refers to the difference in the apparent contact angles at the advancing and receding contact line immediately before droplet motion begins [10, 14]. The wetting angles at which the advancing and receding surfaces start motion are functions of the three phase contact line of the droplet, substrate, and ambient. They are independent of the droplet geometry and are a property of the fluid, ambient environment, substrate material, and substrate structure [10]. The difference in these angles gives rise to the static friction force resisting the motion of the droplet. Like the contact line friction, the underlying causes of the hysteresis are still under investigation [6, 9, 13].

Testing

Due to the small scale and deformable nature of micro droplets and the restrictive geometry of many actuation methods, measuring the forces directly provides a significant challenge. The most common method is to derive the actuation force from the droplet mass and acceleration calculated from optical measurements of the droplet position versus time [4, 15]. Alternatively, the actuation energy is used to derive the actuation force [2]. The individual force components are then approximated from empirical relationships.

Previous work from Crane *et al* has explored direct measurement of electrowetting actuation forces for specific geometries using low force sensors [16]. Ni *et al* investigated the contact line friction for droplets between a fixed and moving surface [17] using a custom build low force sensor system [18]. This thesis is an expansion on this work.

Modeling

Modeling of microfluidic systems can be divided into two methods: forced and energy based. Both of these methods can incorporate analytical and computational methods. Forced based methods for dynamic droplets typically solve the velocity and pressure fields inside the droplet utilizing the Navier-Stokes equation [6] or by using a one-dimensional Navier-Stokes approximation and applying a pressure gradient upon the droplet [3]. Static droplet models typically find the equilibrium between the surface tensions and fluid pressures [19, 20, 11, 21].

Energy based methods derive the forces acting on the droplet by determining the change in total system energy for small displacements [1, 7, 2, 22, 23].

One of the challenges of modeling digital microfluidic system is tracking the surfaces as they can move and distort due to the dynamics of the system. Several different methods are utilized to deal with this challenge. The simplest method is to approximate the surface using a defined geometry [7, 1], such as an arc or a line which is then scaled or transformed. This method often sacrifices the exactness of the solution for ease of computation and as such can often lead to significant error as the actual droplet geometry deviates from the approximations [7, 16].

For more detailed analysis finite element schemes are utilized. The discretization for this method usually falls into a finite volume scheme or a variable mesh scheme [24, 23]. These methods allow for the droplet geometry to change in response to the changing flow and external force conditions [25]. This leads to an increase in the accuracy and robustness of the solution [6].

Several one dimensional droplet transport models have been proposed for electrowetting between to substrates. Ren *et al* first proposed a model where the external force per unit length on the droplet (f_m) is equal to the difference between force due to the actuation voltage (f_a), a threshold initiation force due to contact angle hysteresis (f_{CA}), the internal viscous friction force of the droplet (f_{vis}), the external drag and friction forces of the ambient on the droplet (f_0), and the contact line friction (f_{CL}) [2]:

$$f_m = f_a - f_{CA} - f_{vis} - f_0 - f_{CL} = \frac{\varepsilon_0 \varepsilon_d}{2d} V^2 - f_T - B\left(\frac{\mu_d U}{\gamma}\right)^{0.3} - \left(\frac{mL}{h} + s\right)\mu_0 U + \zeta U \qquad (4)$$

Bahadur and Garimella used as similar approach but calculated the actuation force as a function of the droplet shape and used simpler relationships to estimate the viscous forces and external drag on the droplet [1]:

$$F_m = F_a - F_{vis} - F_0 - F_{CL} = F_a - \left(\frac{6\mu U}{h}\right)(2\pi r^2) - (0.5 C \rho_0 U^2)(2rh) - (\zeta U)(4\pi r) \qquad (5)$$

Both Ren *et al* and Bahadur and Garimella found that the contact line friction force was the primary force opposing the droplet motion [1, 2].

Modeling the surface tension equilibrium and dynamics at the three phase contact line is a difficult problem due to the non-slip boundary condition breaking down at the contact line [13]. To address this, analytical models for the flow field are usually based upon simplifying assumption which neglect the slip at the contact line, relax continuity equations in the field near the line, or use jump equations across the interface [13, 26].. Baird and Mohseni used this method to approximate the velocity profile for a droplet between two parallel plates [3]. Utilizing a quasi-one-dimensional form of the Navier-Stokes equation:

$$\rho \frac{\partial u}{\partial t} + \frac{dP}{dx} = \mu \frac{\partial^2 u}{\partial y^2} \tag{6}$$

the velocity as a function of the height of the droplet is found. The actuation force on the droplet is modeled as acting over the cross-sectional area of the droplet and is transformed into an equivalent pressure gradient [3]:

$$\frac{dP}{dx} = \frac{\Delta P}{l} = \frac{F_a w h}{l} \tag{7}$$

For steady-state motion of the droplet, the velocity profile is approximated as:

$$u(y) = 6\bar{u}\left(\frac{y}{h} - \frac{y^2}{h^2}\right) \tag{8}$$

where the average velocity is:

$$\bar{u} = \frac{h^2}{12\mu}\frac{\Delta P}{L} \tag{9}$$

To more accurately model the velocity profile inside the droplet, Ahmadi *et al* created a pseudo-three dimensional finite volume numerical model where the two dimensional velocity profile was solved in the vertical mid plane of the droplet. The solution was then scaled and applied to planes parallel to the mid plane [6]. The resulting pressure field in the droplet was then used to correct the shape of the droplet and iterations were done until the solution converged. Using this numerical method, Ahmadi *et al* found an increase in the calculated shear force as compared to

simplified parabolic velocity profile approximations. However, the contact line forces still dominated the viscous losses [6].

Purpose

While the friction force for droplet motion has been addressed by other sources, most of the information available is either theoretical in nature or is tied to specific configurations and actuation methods. For the latter, force values are usually derived from actuating method, such as electrowetting, and the resulting droplet motion rather than directly measured. Therefore the results found for the friction forces are often tied to the method of actuation and configuration, such as sessile droplets or channel flows. For the theoretical and micro scale methods, only the contact line friction is usually considered being modeled from gas dynamics or micro scale fluid dynamic phenomenon. Possible interactions with other forces and phenomena acting on the droplet are neglected.

Goals

The overall all goal of this thesis is to provide a simple, one-dimensional model which can be used as a design tool to determine the frictional forces, both static and dynamic, of a droplet moving under a rectangular cover slip across a hydrophobic surface for varying system geometries. To accomplish this goal, the frictional forces will be experimentally measured using a low force sensor and then decomposed into their contributions; for static friction: the contact line pinning and contact angle hysteresis forces, and for dynamic friction: contact line friction, contact angle hysteresis, and viscous dissipation forces.

Methodology

Testing

The first step in this analysis is to gather a bank of friction force data from testing. As the focus of this analysis is the effects of the droplet configuration on the friction, the variable system parameters were limited to droplet geometry and bulk velocity. Figure 1 illustrates these

parameters. In order to allow the data to be useful for the most possible configurations, a rectangular droplet configuration was selected to help eliminate curvature from the contact lines and surfaces so that they could be approximated as linear and either parallel (length) or perpendicular (width and height) to the velocity and the data could be correlated to a first order approximation as a function of the droplet width, length, height, and bulk velocity. To this end a hydrophilic glass rectangular cover slip was selected so that the droplet would conform as much as possible to the ideal rectangular prism shape [16].

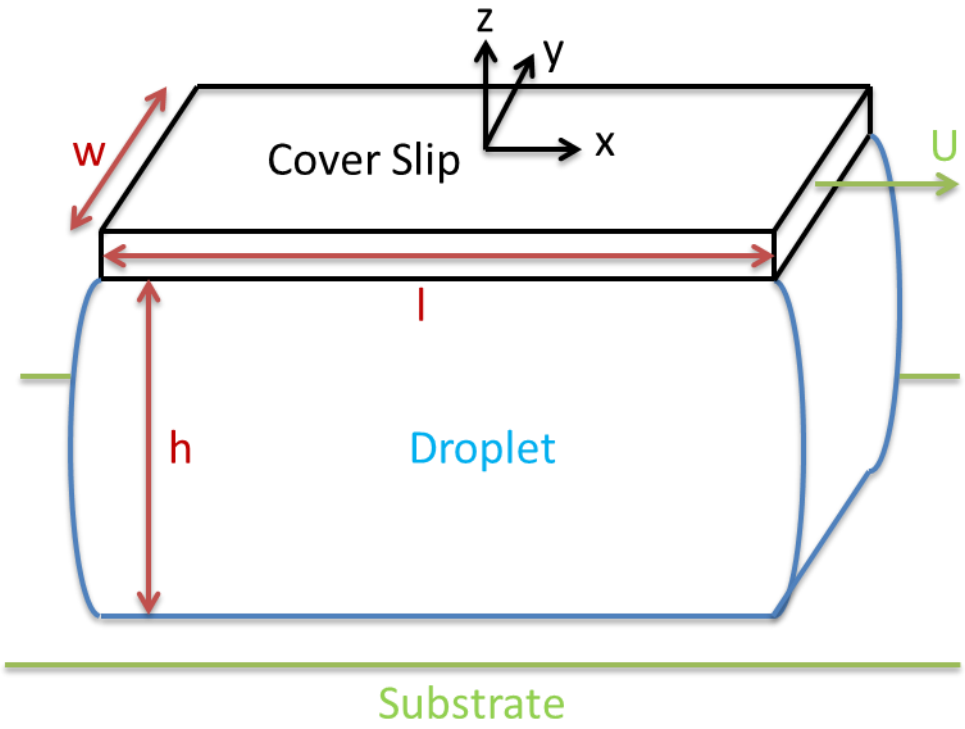

Figure 1: Droplet schematic with variable system parameters

A testing plan was then created which varied the system parameters of the bulk droplet velocity, cover slip width and length, and the gap height between the cover slip and the substrate while holding constant the cover slip, substrate, and fluid properties.

Analysis

Three hypothesized relationships were developed to characterize the relationship between the static and dynamic friction force components and the geometric and velocity droplet

system parameter (equations (14), (15), and (17)). The relationships were based upon the assumed droplet shape and relevant force components. The test data was then fit to these relationships by minimizing the error between the actual and predicted forces.

Modeling

Two simple models were also created based upon the assumed droplet geometry and contact line behavior to determine how well they would predict the static forces. The droplet stiffness was calculated assuming no surface curvature during the droplet deflection using energy methods [7]. The droplet breakaway force was calculated using the droplet width and contact angle hysteresis values (equation (11)). The two models were then compared to the test data.

Validation

Additional testing varying the system parameters outside of the initial test schedule was conducted to determine the robustness of the correlations and model predictions.

Hypothesis

The guiding hypothesis of this thesis is that the total force acting upon the droplet can be broken down into a linear combination of component forces, each of which can be treated as independent from the others, allowing analysis of each force component by varying the system parameters affecting them. Additionally, deformation and the movement of the droplet can be divided into two distinct phases: static deformation and dynamic motion, with the force components of these two phases treated separately.

Static

During the static phase, the cover slip displaces while the contact lines of the droplet remained pinned to the substrate resulting in a deformation of the droplet from its equilibrium state. As the droplet deforms, a resisting force to the cover slip displacement results from imbalance of the contact angles at the advancing, θ_1, and receding, θ_2, contact lines, as shown in Figure 2. This phase exists until the critical contact angles (θ_a and θ_r) are met at the respective

contact lines resulting in their motion. Until the critical angles are reached, the contact angles can vary such that:

$$\theta_r < \theta_1, \theta_2 < \theta_a \tag{10}$$

This limiting imbalance is the contact angle hysteresis. The droplet forces at which the contact lines start their respective motion will be referred to as the breakaway forces. It is assumed for the analysis of the testing data that the advancing contact angle is met before the receding contact angle and as a result the advancing contact line will being motion before the receding. However, for the modeling of the system this difference will be neglected as it is minimal with respect to the displacement of the slide and only the maximum force is used. Therefore for the static phase the force acting upon the droplet, F_{st}, can be expressed as a function of the advancing and receding contact angles, $\theta_1$and θ_2, the width of the droplet w, and the surface tension, γ, by:

$$F_{st} = \gamma w(\cos\theta_2 - \cos\theta_1) < F_{break} \tag{11}$$

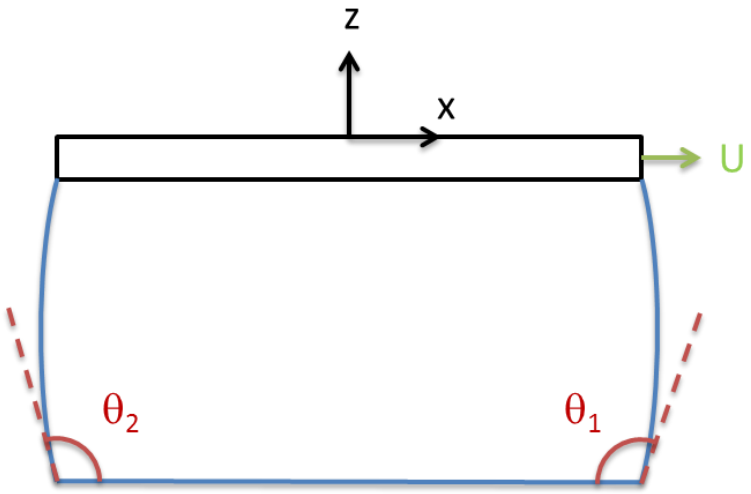

Figure 2: Advancing and receding contact angles with respect to bulk velocity

It is assumed for this analysis that the contact angles at the advancing and receding contact lines can be expressed as functions of the gap height, h, and cover slip displacement, x, and therefore the static force can be expressed as a function of the variable system parameters:

$$F_{st} = f(h, w, x) \tag{12}$$

Since for a given system, the gap height and width are constant, the static force can therefore be expressed in terms of a stiffness, k:

$$F_{st} = kx \tag{13}$$

For a given small displacement the change in angle is approximately inversely related to the droplet height, therefore the stiffness can be approximated by:

$$k = C_k \gamma \frac{w}{h} \tag{14}$$

The breakaway of the droplet occurs when the critical contact angles are met. These contact angles are a property of the fluid, substrate, and surrounding medium and therefore the breakaway force, F_{break}, is assumed to be only a function of the width:

$$F_{break} = C_{break} \gamma w \tag{15}$$

Figure 3 illustrates the relationship between the static force, stiffness, and breakaway force with the variable system parameters and the cover slip displacement.

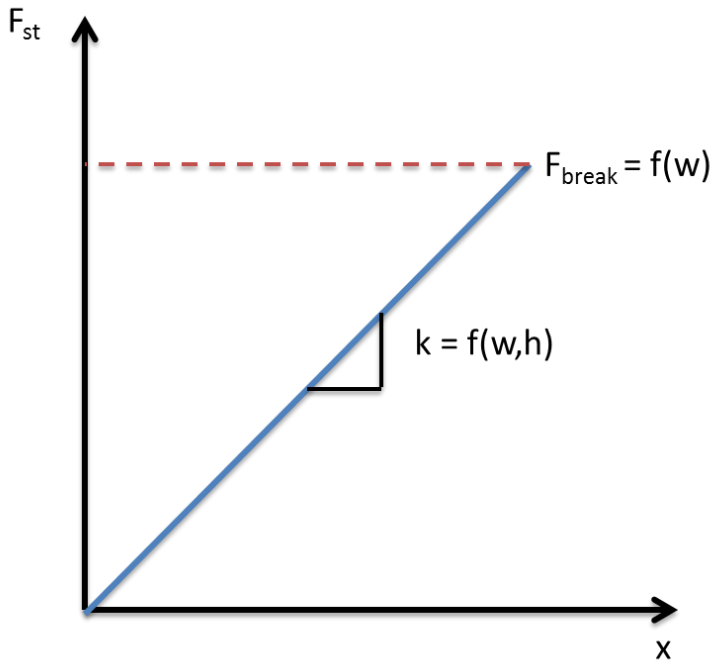

Figure 3: Static force versus displacement showing expected linear droplet stiffness

Dynamic

The dynamic phase begins at the onset of droplet motion after breakaway and continues until the beginning of droplet deceleration. The forces during the deceleration of the droplet are not addressed in this analysis. The force on droplet during the dynamic phase, F_{dyn}, can be decomposed into three forces: the dynamic contact angle force, F_{CA}, the contact line drag force, F_{CL}, and the force due to viscous losses, F_{vis}:

$$F_{dyn} = F_{CA} + F_{CL} + F_{vis} \tag{16}$$

Similarly to the static phases, the dynamic contact angle force arises from the difference between the advancing and receding contact angles. For the purpose of this analysis, it is assumed that the dynamic contact angles are not a function of the velocity and that the contact line forces related to the velocity are addresses by the contact line drag. The dynamic contact angle force is then:

$$FCA = C_{CA}\gamma w \tag{17}$$

Ideally, the dynamic contact angle force should be equal to the breakaway force. However, due to the simplifying assumptions for the dynamic contact angle behavior with the bulk droplet velocity some discrepancy between the breakaway force constant, C_{break}, and the dynamic contact angle force constant, C_{CA}, may exist.

The contact line force, F_{CL}, is due to the gas dynamics at the contact line and is assumed to be a function of the length of the contact line and the bulk velocity, U [6]:

$$F_{CL} = C_{CL}Uw \tag{18}$$

The dynamic force on the droplet due to the viscosity of the fluid is a function of the shear force acting on the droplet at the substrate and the internal viscous loss of the fluid. It is assumed that the internal flow is laminar and that the shear force at the substrate is much larger than that of the internal viscous loss due to turbulence. The shear loss at the substrate is given by:

$$F_{vis} = \mu \left.\frac{du}{dz}\right|_{sub} A \tag{19}$$

It is assumed that the shear force is equal over the wetted area of the substrate and the velocity gradient at the substrate can be approximated by a constant times the bulk velocity and the gap height such that:

$$F_{vis} = C_{vis}\mu\frac{U}{h}wl \tag{20}$$

The total dynamic force can then be expressed:

$$F_{dyn} = C_{CA}\gamma w + C_{CL}Uw + C_{vis}\mu\frac{U}{h}wl \tag{21}$$

Figure 4 illustrates the relationship between the dynamic and contact angle forces with the variable system parameters and bulk velocity.

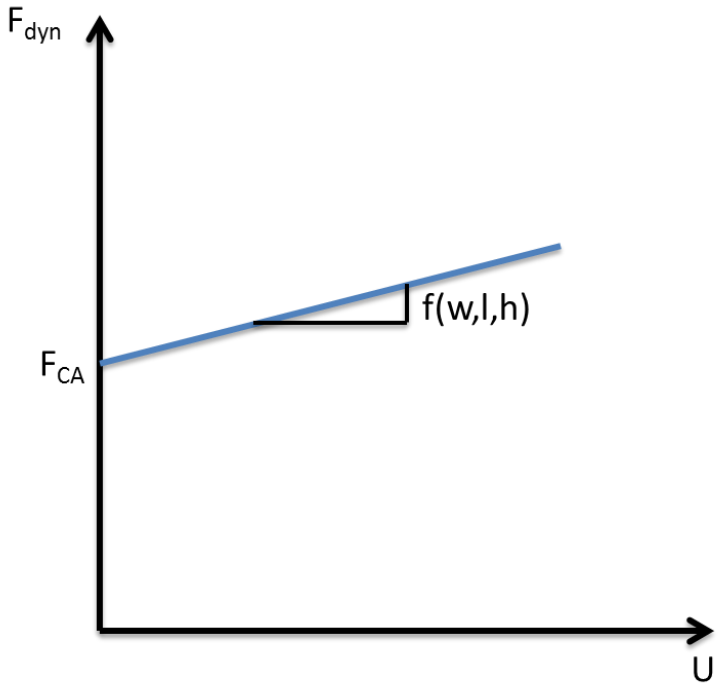

Figure 4: Dynamic force versus bulk velocity showing expected linear relationship with velocity

TESTING

The goal of this thesis is to find a simple, one-dimensional model to predict droplet friction. To determine how the friction forces vary on a droplet with droplet geometry and bulk velocity a series of tests were conducted varying the droplet width, length, height, and steady-state bulk velocity. The data from this testing was then used to derive the constants to the hypothesized force components.

System Parameters

The fluid, cover slip, substrate system can be characterized by a combination of variables and parameters related to the geometry, fluid and substrate properties, and system dynamics. To focus upon the effects of the system geometry and bulk velocity upon the friction force, the parameters relating to fluid and substrate properties were held constant, while the cover slip width and length, gap height, and velocity were varied. Figure 1 illustrates the variable system parameter of the droplet. Table 1 summarizes the assumed values for the constant fluid and surface properties [17].

Table 1: Constant system parameters

Parameter	Value	Units
a	10	mm/s^2
γ	72.0	μN/mm
θ_a	116.2	deg
θ_r	103.6	deg
μ	1.00E-3	μN*s/mm^2
g	9.81	m/s^2
ρ	998	kg/m^3

Approach

A series of tests were designed to test the hypothesized relationships summarized in equations (11) and (21) between the variable system parameters and the components of the friction force.

Static

For the static friction force (F_{st}), two system parameter were of interest: the relationship between the cover slip displacement (the stiffness), and the force at which droplet motion starts (the breakaway force).

Stiffness

From equation (14), the stiffness of the droplet (k) is a function of only the width and height of the droplet. By holding the width constant and varying the height, the stiffness constant (C_k) can be determined

Breakaway Force

From equation (15), the breakaway force (F_{break}) of the droplet is a function of the contact angle hysteresis. For a given droplet width, the breakaway force at which the droplet starts motion should be constant. The breakaway force constant (C_{break}) can be found by varying the droplet width.

Dynamic

The dynamic friction of the droplet is assumed to be composed of three components: the contact angle hysteresis, the contact line friction, and the viscous losses, as expressed by equation (21).

Contact Angle Hysteresis

For this analysis, during the dynamic phase, a constant force independent of the velocity due contact angle hysteresis, (F_{CA}) is assumed to resist the motion of the droplet. From equation (21), this force component varies only with the width. The contact angle force constant (C_{CA})) can be found by varying the width of the droplet while holding the length, height, and velocity constant.

Contact Line Friction

The contact line friction (F_{CL}) is the component of the total dynamic friction force which can be attributed to advancing the contact line independent of the contact angle hysteresis. From equation (21), the contribution of this force and therefore the contact line force constant (C_{CL}) can be found by holding the height, width, and length of the droplet constant and varying the velocity.

Viscous Losses

The viscous loss contribution (F_{vis}) is the component of the total dynamic friction force which results from the internal droplet flow field and fluid viscosity. By varying the droplet length and height, while holding the width and velocity constant, the contribution of the viscous loss and the viscous force constant (C_{vis}) can be found.

Table 2: Testing schedule

Test #	w (mm)	l (mm)	h (mm)	U (mm/s)
1	9	9	0.75	1
2	9	9	0.75	2
3	9	9	0.75	4
4	9	9	1	1
5	9	9	1	2
6	9	9	1	4
7	9	9	1.25	1
8	9	9	1.25	2
9	9	9	1.25	4
19	4.5	9	1.25	1
20	4.5	9	1.25	2
21	4.5	9	1.25	4
22	9	4.5	1.25	1
23	9	4.5	1.25	2
24	9	4.5	1.25	4
28	4.5	4.5	1.25	1
29	4.5	4.5	1.25	2
30	4.5	4.5	1.25	4

Testing Schedule

Table 2 shows a summary of the testing schedule with the varying droplet widths, lengths, heights, and bulk velocities used. A minimum of five runs was conducted for each test. Additional runs were conducted if anomalies in the data were observed.

Testing Setup

Hardware

The force measurements were conducted using a custom designed measurement apparatus for measuring droplet friction utilizing a low force sensor and single degree of freedom stage which moves relative to the fixed position of the droplet [18] shown in Figure 5. The test droplet was placed on a glass substrate coated with Cytop to give it a hydrophobic equilibrium contact angle of 111 degrees. A rectangular, thin (0.13 mm to 0.18 mm) glass cover slip with an attached glass fiber was then placed onto the droplet, as shown in Figure 6, through the use of a vacuum suction cup positioned by a 3-axis micro-positioner system. The opposite end of the glass fiber was attached to a nanoScience low force sensor (FT-S540 or FT-S1000 depending on the test). The sensor was fixed to another 3-axis micro-positioner system mounted on a pneumatic vibration isolation table, as shown in Figure 5. The FT-S540 sensor has a force range of 180 μN with a sensitivity of 90 μN/V with a resolution of 0.3 μN at 1000 Hz sampling frequency [27]. The FT-S1000 sensor has a force range of ±1000 μN with a sensitivity of 500 μN/V with a resolution of 0.5 μN at 1000 Hz [28]. The glass substrate was taped to an intermediate glass plate fixed via double sided tape to a Newport Micro-controle UTS100CC single degree of freedom stage, as shown in Figure 7. This stage was also attached to the vibration isolation system. The entirety of the described system was housed inside a custom build isolation box as to prevent external perturbations (such as air currents) from effecting the measurements. The stage was controlled by a Newport model ESP301 Motion Control system. The force sensor power input and output voltage was handled by a National Instruments USB-6343 data acquisition system, with the output voltage being first run through a 1000 Hz analog low pass

filter. Video of the testing was captured using a UI 155 digital camera with a Computar M1214-MP2 lens and brass spacers. The data from the stage motion control system and data acquisition system and the digital camera were all sent to a PC which controlled the entire setup and preformed the initial data analysis.

Additionally, the contact angles of the glass substrates were measured using a UI 221 digital camera with a Edmunds Optics model number 63745 1.0x40 mm lens utilizing a Rame'-Hart NRL C.A. Goniometer.

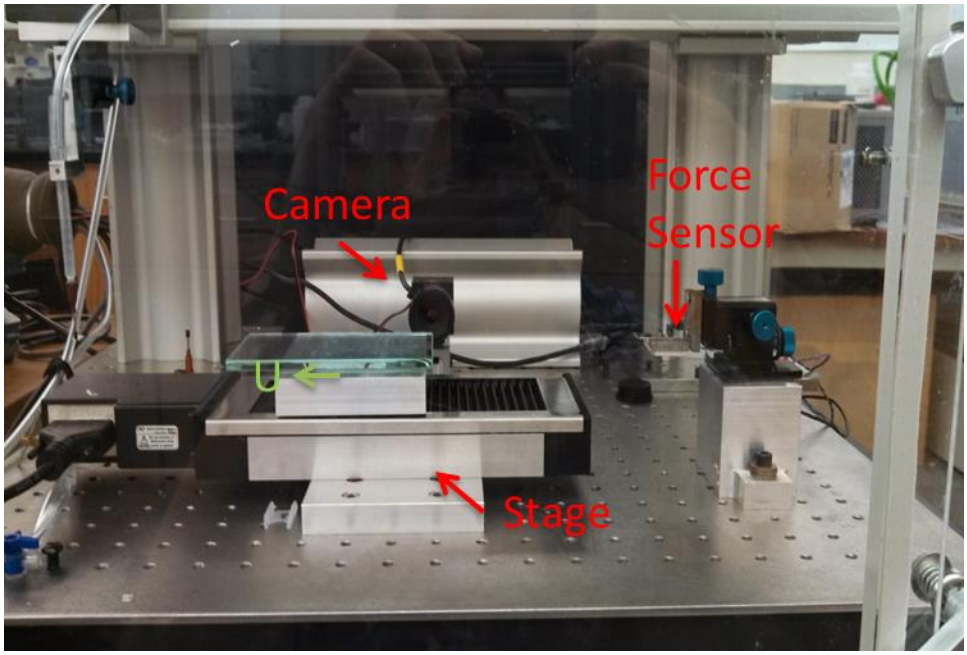

Figure 5: Test setup to measure droplet friction. The single axis stage, controlled for position, velocity, and acceleration, provides the relative motion between the droplet and the substrate. The low force sensor measures the resisting force to the droplet motion as a voltage which is supplied to the data acquisition system. The digital camera captured video of the droplet during testing use to diagnose cover slip stability issues.

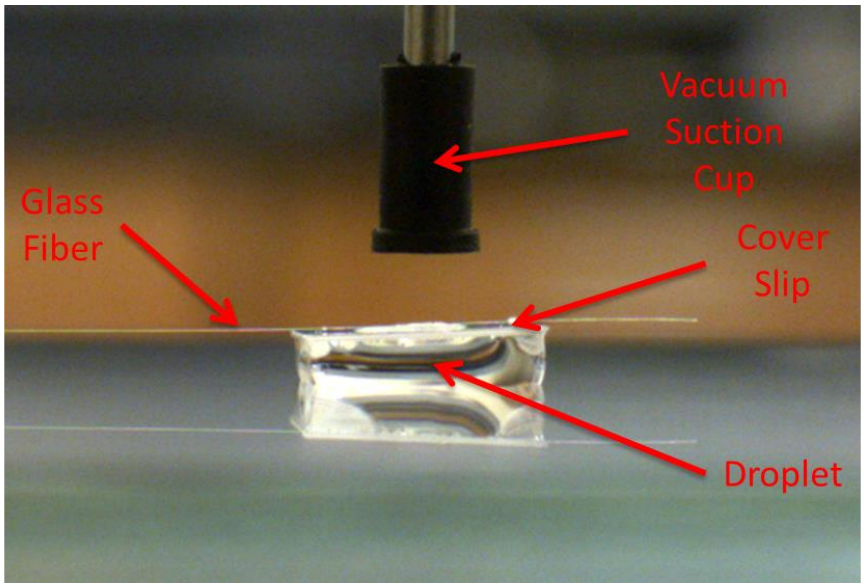

Figure 6: Deionized water droplet on Cytop coated substrate with thin glass rectangular cover slip on top. Cover slip is placed and removed from droplet using a vacuum suction cup attached to a micro-positioner. The cover slip is attached to a low force sensor by glass fiber secured by super glue.

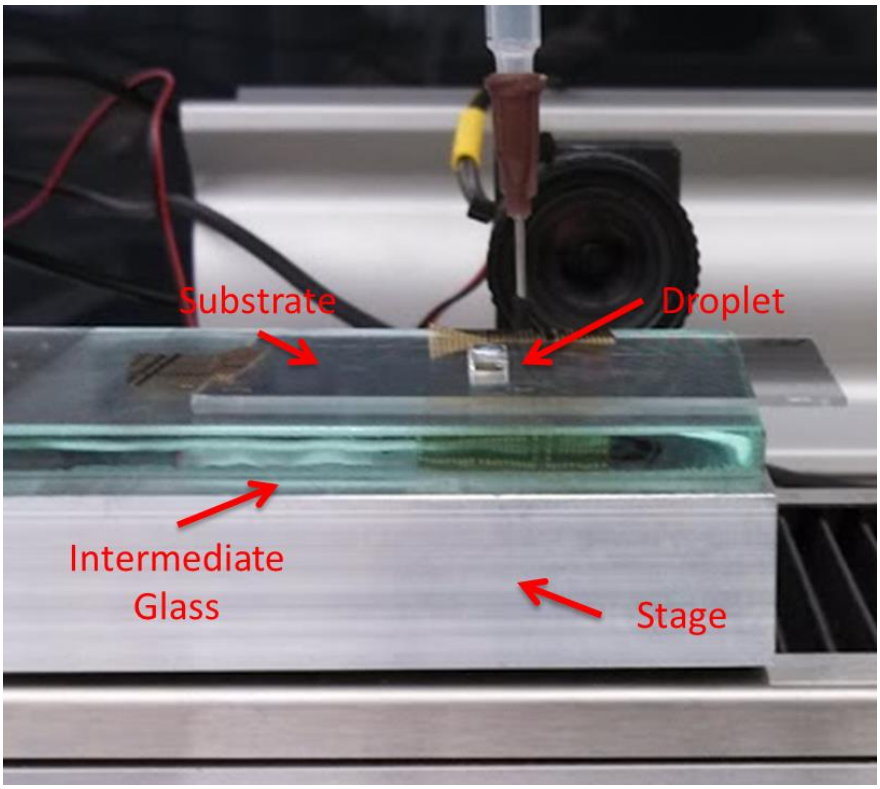

Figure 7: Substrate taped to intermediate glass plate. The intermediate glass plate was then attached to stage using double sided tape to allow for large repositioning of substrate relative to sensor.

Software

LabView

A custom LabView program was provided to handle the control of the stage and sensor data acquisition. This program had several important functions and features. A user graphical user interface allowed for the control of the stage velocity, acceleration, and distance as well as the data sampling frequency from the force sensor, and the location of data output. Internally the program synced the position and velocity data from the stage and the output voltage from the force sensor. The force sensor voltage went through an additional low pass digital filter and then was converted to force data using the manufacture supplied calibration data specific to each force sensor. The raw and processed data was then shown graphically in the GUI to allow for almost instantaneous inspection. All of the raw and converted data was then output as a tab delimited data file for further post processing in Excel.

Excel

All of the data post processing was done using Excel 2007. The data output from the LabView program was copied into a custom spreadsheet which was used to segment the data and extract system performance data. Linear interpolation of individual run data was done using the Linest function. The Solver add-in was utilized to fit the system data to the hypothesized equations.

Imaging

The uEye software [29] was used to capture video of the testing runs and to take still photos used in contact angle analysis of the substrates. The still photos were then post processed using the ImageJ software [30] with the DropSnake [31] plugin to calculate the contact angles for each test substrate.

Procedure

Preparation

Substrate

The glass substrate was cleaned using the Pirahna solution (sulfuric acid H202, 3 to 1 ration) with a 30 minute soak to remove any organic containment. After the clean, the substrate was dried in a nitrogen spinner and then the Cytop coating was applied by spin coating. After the coating was applied, the solvent of the Cytop was evaporated on a hot plate and then was baked in a convection oven at 200°C for one hour. The final Cytop coating thickness was 1.2 μm. The substrates were then stored in a vacuum storage container until testing.

Cover Slip

The cover slips for the dimensions other than 9 x 9 mm^2 were cut from a 25 x 25 mm^2 microscope cover slip by use of a micro automatic dicing saw.

Glass Fiber

A single strand of glass fiber with an approximate diameter of 10 to 20 μm was used as a line between the force sensor and the droplet cover slip. To attach the fiber to the force sensor it was first inserted into a small diameter glass tube with a small portion sticking out to help align and position it. The glass tube was then held in place while the tip of the force sensor was positioned in proximity using the micro positioner. A small drop of superglue was placed on the tip of force sensor and it was then guided into contact with the fiber. After the glue had dried, the glass tube was slid off the fiber.

Cover Slip Attachment

The hardest and most critical step for constant results, as discussed later in the error section, was the attachment of to cover slip to the glass fiber. Because of the delicate nature of the force sensor, it is less likely to damage the sensor by leaving it mounted to the isolation table with the glass fiber attached throughout the testing. The cover slip is changed by cutting it free from the fiber and gluing on a new cover slip. Two methods were used during testing for reattachment of the cover slip to the fiber.

The original method used was to first lay the attached fiber straight out from the sensor on to a glass plate. The end location of the fiber was noted and the fiber was carefully moved to the side. The cover slip to be attached was then placed at the noted location and aligned so that it was centered and its leading edge would be perpendicular to the axis sensor. A drop of superglue was then placed in the center of the cover slip. The fiber was then lifted using a bent wire and aligned over the drop. Using a small amount of tension to straighten the fiber, the wire was dragged along the length of the fiber allowing it to fall onto the drop of superglue. The fiber was then allowed to dry in place.

This method had several issues which led to difficulties reattaching the cover slip precisely. The main issue was that all the steps took place inside the isolation box making it hard to access and get proper alignment. The secondly, the wettability of the superglue to the cover slip led to a thin coating which sometimes resulted in poor adhesion of the fiber. The wettability also resulted in fast drying times so that alignment error could not be corrected. Lastly, the line had to drop perfectly to get good alignment.

In the second method, the ends of a new unattached fiber are taped down to straighten it under tension. The cover slip was then placed under the fiber and was positioned so that it was centered and aligned with the front edge perpendicular to the fiber. A drop of gel type superglue was then applied simultaneously to both the fiber and the center of the cover slip. After the glue dried, the fiber was trimmed so that approximately one inch longer on one side of cover slip and flush with the other. A piece of Plexiglas with a one inch hole was placed inside the isolation box. The fiber attachment to the sensor was then laid out straight with the end centered in the middle of the hole. The cover slip was then positioned so that both fibers were aligned in close proximity with a small overlap in the length of the fibers. A thin superglue was then gently applied to the overlap of the fibers using the wetting action of the glue to further align and pull the fiber ends together. The glue was then allowed to dry.

The main benefit to this method was the critical fiber/cover slip alignment outside of the isolation box where it was easier to control. Keeping constant tension on the fiber also assisted in

this. The slower drying time of the gel type superglue also allowed for small corrections to alignment errors and the thicker coating improved adhesion.

Substrate Attachment

The glass substrate was attached to the stage by an intermediate piece of glass using two small pieces of tape, one on a side edge and the other on the end, to secure it from translation or rotation. The intermediate glass piece was then attached to the stage by the use of double sided tape to allow for its removal.

Fluid

Room temperature deionized water was used from a lab line supply and was degased in a vacuum jar overnight.

Testing

Droplet

A Huawei pipet used to place a measured drop on to the test substrate. The droplet was placed so that it would not travel over previously used section of substrate. The volume of the droplet was selected for the target height and cover slip dimensions by assuming full wetting of the cover slip and no curvature of the droplet sides:

$$\forall = wlh \tag{22}$$

Cover Slip Placement

The cover slip was held by a vacuum suction cup system off of the substrate when not in use. For testing, it was positioned above droplet with micro positioners with a slight bias towards the sensor and then slowly lowered to make contact. As the cover slip is hydrophilic, the droplet is pulled under the cover slip, wetting it. The bias in the positioning of the cover slip insures that the path the droplet will travel was not wetted by the droplet. If the droplet did not fully wet over the entire cover slip, the cover slip was further lowered, "squishing" droplet between cover slip and substrate forcing it to wet to the corners. The vacuum holding the cover slip was then released and suction cup raised allowing the cover slip to self-align on the droplet. The cover slip was then rotated as needed to align with the sensor. Tension was applied by moving the micro

positioner on which the sensor was mounted to check the alignment of the cover slip, fiber, and sensor. Any corrections were made by moving the sensor vertically or laterally so that the fiber was appeared parallel to the direction of travel in both planes. Figure 6 shows the cover slip on the droplet after tension has been applied to the glass fiber.

Alignment Run

The LabView program was then set to droplet dragged 10mm at the testing velocity. This served to further align the cover slip and sensor before the testing runs. The force sensor data was checked on the GUI to insure that it had reached a steady state at the end of the run indicating the cover slip had reached alignment.

Testing Runs

Before each testing run, the fiber was slacked to allow the droplet to return to an equilibrium position and return the sensor as close to zero force as possible. Test settings were then entered into LabView, the camera set to record, and the run started.

The data output from the generated output Excel file was then copied to the master test file. The force versus distance data for the run was immediately plotted to insure the data was free of alignment, tension, wetting, or contamination from dust, dirt, or surface defects on the substrate.

If sufficient room was left on the substrate after a run, the same droplet was used again until no more unused space to drag the droplet was left on the substrate. The line was slacked between each run and new video and test run was started.

A minimum of 5 runs of each test condition were conducted, with more runs taken if an error was seen.

Droplet Removal

When a new droplet volume was needed or insufficient room remained on a substrate for another testing run, the droplet was removed. To remove the droplet, a large amount of slack was put into the fiber to prevent damaging the sensor. The suction cup was then centered above the cover slip and lowered to make contact. The vacuum was then applied and cover slip slowly

raised until droplet detached from substrate and was suspended underneath the cover slip. A Kimwipe was then used to absorb droplet from bottom of cover slip. If further unused space on the testing substrate was available to the side of the previous run, the under lying glass which the substrate was taped to was repositioned so that the unused portion of the substrate was underneath the cover slip. A new droplet was then placed and the alignment sequence repeated.

Contact Angle Testing

After a substrate had been completely used, it was positioned on the goniometer and 5 µL droplet of the testing water was placed on the substrate. A picture was then taken of the droplet, and the contact angle was calculated using the ImageJ software to verify the consistency of the wetting properties of the substrate.

Analysis

The analysis of the testing data was broken down into three phases: post processing of the individual runs, computation of test group average force data, and fitting of the force models to the data.

Individual Runs

The first step in post processing the individual test runs was copying the raw data into a custom spreadsheet for the analysis. The raw data as outputted from the LabView program contained segments of data before and after the test run that was used to align the force sensor and stage data. This data was deleted leaving only the relevant test data.

A correction in the raw data was also made to account for the initial tension in the fiber before the relative cover slip displacement. The LabView program zeroed the force data based upon the initial output voltage of the sensor. This zero would subtract the fiber tension from the data and create a small error. To correct for this, a correction was calculated by multiplying the difference between the initial voltage and zero voltage for the sensor by the calibration factor for the sensor. The force correction was then added to the raw force data.

The custom spreadsheet was then used to conduct a segmented linear regression analysis. The data for each run was divided into five main regimes: start/fiber slack, static deflection, flow development, steady-state, and deceleration/relaxation. Figure 8 shows a representation of the force/displacement data showing the five regimes. The dividing point between each regime was found by inspection of the force/displacement data for each run.

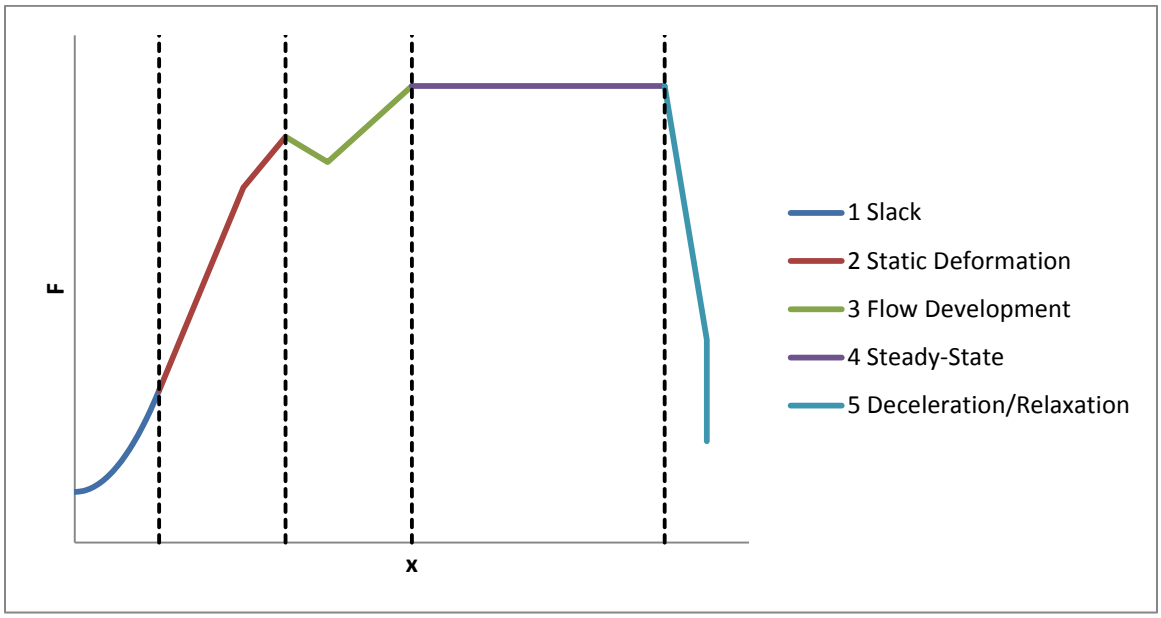

Figure 8: Data regime illustration showing five regimes used to divide the test run data for analysis

Start/Line Slack

Due to the slack in the fiber, the initial movement of the stage does not cause significant deflection in the droplet. As the stage continues to move, the tension in the fiber slowly starts to increase until the fiber becomes taut. This gradual increase in tension acts to "soften" the measured stiffness of the droplet. Because of this error, this initial section of data is not included in the droplet stiffness calculations. This data regime is shown as segment 1 in Figure 8.

Static Deflection

Due to the contact line pinning, the droplet initially undergoes a static deformation. From the contact angle hysteresis between the advancing and receding surfaces, this deformation results in a resisting force versus the relative displacement of the cover slip as illustrated in Figure 8 as segment 2. For small displacements, this force/displacement relationship is approximately linear and is analogous to spring stiffness. The stiffness is constant until the displacement is large enough that the critical advancing contact angle is met and the advancing contact line begins movement. Until the critical receding contact angle is met and the receding contact line begins movement, a secondary softer stiffness is measured. Figure 9 shows an example of this phenomenon for a droplet with a width, length, and height of 9 by 9 by 0.75 mm respectively.

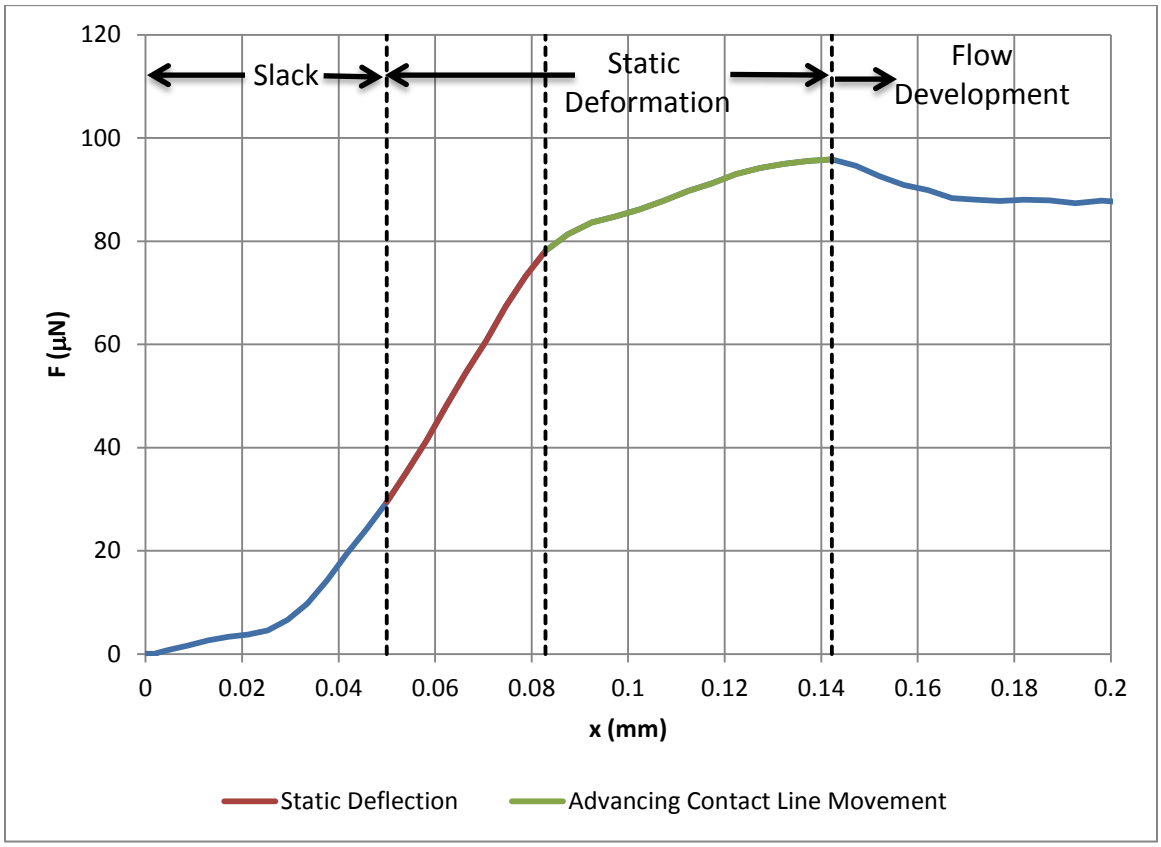

Figure 9: Sample static deflection data for a 9 x 9 x 0.75 (w x l x h) mm^3 droplet showing the key stages in the force evolution as described in the text.

Several system parameters were calculated for this static deflection regime. First, the breakaway force for the initiation movement of each contact line was found by determining the point at which the force/displacement slope changed. The apparent stiffness for before and after the advancing contact line as well as the overall stiffnesses were calculated using the Excel linear regression function. Lastly, the displacement to the initiation contact line movement was determined. Due to the initial softening from the slack in the fiber, an approximation for zero displacement had to be found. The slope of the force/displacement relationship before contact line movement was used to find the stage displacement at which the force should have been zero without the softening effect, as shown in Figure 10.

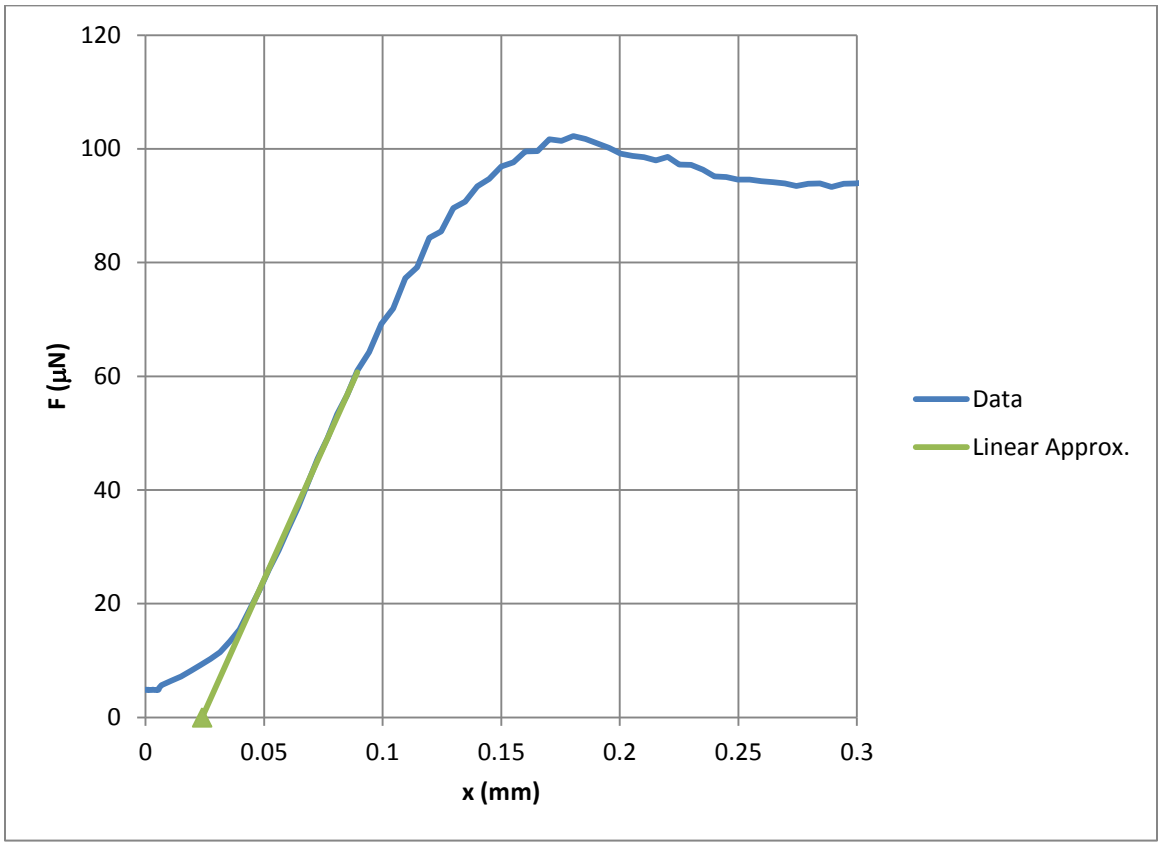

Figure 10: Displacement approximation using linear approximation of droplet stiffness

Flow Development

After the initiation of movement for both the advancing and receding contact lines, the force/displacement data would sometimes exhibit two separate phenomena. The first was a

relaxation in the force. This relaxation is thought to be cause by a release in energy stored by the droplet during its initial static deflection. During some test runs, the initial relaxation in the force was followed by a corresponding increase in force and a decaying oscillation would occur analogous to a spring-damper system. The displacement from the breakaway force to the final relaxation was recorded along with the corresponding force.

The second phenomenon was a gradual increase in the force. This occurred when the droplet breakaway happened before the test velocity was reached by the stage. The slope of the force versus the velocity was calculated by linear regression. Both of these phenomena are illustrated by segment 3 in Figure 8.

Steady-State

After the stage has finished its acceleration and the droplet dynamics have decayed, the force/displacement data reached a steady-state regime marked by an approximately constant force. The key system parameter for this regime is the average force value. Line segment 4 in Figure 8 represents this regime.

During some of the testing runs, large increases in the force data were observed on individual runs that were not indicative of the group average. By reviewing the test video, it was seen that instabilities due to cover slip tilting or yawing corresponded to the force spikes. The data for steady-state average for these runs was truncated before the onset of the instabilities. The overall test maximum force was recorded to capture the effect of these instabilities.

Deceleration/Relaxation

After the steady-state velocity regime, the stage decelerates at approximately the same rate as the initial acceleration. The force data sharply decreases with the decrease in velocity. After the stage velocity has reached zero, there is a more gradual decay in the force as the advancing and receding surfaces and contact angles return to their static equilibrium shapes. This regime is shown as line segment 5 in Figure 8. This data was not used but is saved for future analysis.

Test Group Data

The test group data was compiled by averaging the system parameters from each of the individual runs with the standard deviation for the test group calculated. This method was chosen, instead of compiling the test data into an average run, to avoid the problem of trying to align the data as the varying initial slack in the fiber causes offset in the droplet deflection with stage displacement.

System Performance

The relationship between the variable system parameters and the stiffness, the breakaway force, and the dynamic force was determined by using a least-squared error regression to solve for the coefficients in equations (14), (15), and (21). A spreadsheet was created in Excel 2007 which utilized the Solver add-in. Initial guess of the coefficients were used to calculate the system values for each test group. The error in the calculated value was then found compared to the average value from the data of each test group. The error for each test group was then normalized by the test data value and then squared, with the total normalized error found by the sum of each group's error. The Solver add-in was used to find the value of the coefficient that minimized the total error.

Summary

With the goal of deriving a simple one-dimensional model for the droplet static and dynamic friction as a function of the droplet geometry and velocity, a series of test were derived which varied the droplet width, length, height, and steady-state velocity while holding the fluid, substrate, and ambient properties and droplet acceleration constant. The droplet geometry is varied by using a thin glass rectangular cover slip and by changing the droplet volume. The friction force measurements are found by attaching the cover slip to a low force sensor via a thin glass fiber and the velocity and acceleration is controlled by a single axis stage. The data is analyzed using linear regressions to determine the stiffness, breakaway force, and steady-state force for each individual run and the test group averages are correlated to hypothesized

equations by means of least-squared error regression. The results of this testing will be compared to two analytical models based upon the assumed droplet geometry and measured contact angle hysteresis

MODELING

The goal of this thesis is to find a simple, one-dimensional model to predict droplet friction. In addition to the empirical correlations used to predict the droplet static friction behavior, two simple analytical models were derived: an analytical model of the stiffness of the droplet based upon a simplified geometry and the breakaway force based measured values of the critical contact angles. These two models can be used to show how changes in the droplet geometry affect static friction.

Stiffness

The force and the resulting stiffness of the droplet during the static deflection can be approximated by assuming the shape of the droplet and using the principle of virtual work [7]. The principle of virtual work states that the force due to a displacement is equal to the rate of change of the energy of a system due to the displacement [7]:

$$F = -\frac{\partial E}{\partial x} \tag{23}$$

During the static deformation the contact lines on the substrate and cover slip are pinned so that it can be approximated that the only change in energy is due to the change in area of the free surface of the droplet. The energy as a function of the surface tension and the total surface area (A_T) is then:

$$E = \gamma A_T \tag{24}$$

It was assumed that the curvature of the droplet surfaces is small and therefore the volume of the droplet can be calculated by approximating the droplet as a rectangular prism. By extending this assumption, Figure 11 shows a schematic of the droplet after a small displacement of the cover slip relative to the substrate. The advancing (A_a) and receding areas (A_r) are then:

$$A_a = A_r = w\sqrt{x^2 + h^2} = wh\sqrt{1 + \left(\frac{x}{h}\right)^2} \tag{25}$$

And the side surface areas (A_s):

$$A_s = lh \tag{26}$$

The total surface area of the droplet is then:

$$A_T = 2A_s + A_a + A_r = 2lh + 2wh\sqrt{1 + \left(\frac{x}{h}\right)^2} \tag{27}$$

As a check for this model, the volume of the droplet must be conserved such that:

$$\frac{d\cancel{V}}{dx} = 0 \tag{28}$$

The volume of the droplet can be found from the width and side area:

$$\cancel{V} = wA_s = wlh \tag{29}$$

As equation (33) is not a function of the displacement, the volume is conserved. The energy of the droplet is then:

$$E = \gamma A_T = \gamma\left[2lh + 2wh\sqrt{1 + \left(\frac{x}{h}\right)^2}\right] \tag{30}$$

Taking the derivative with respect to the displacement, the static deflection force is then:

$$F = -2\gamma\frac{w}{h}\frac{x}{\sqrt{1 + \left(\frac{x}{h}\right)^2}} \tag{31}$$

Stiffness is defined as the change in the force for a change in the displacement by:

$$k = -\frac{\partial F}{\partial x} \tag{32}$$

Taking the derivative with respect to the displacement of the force equation:

$$k = 2\gamma\frac{w}{h}\left\{\frac{1}{\sqrt{1 + \left(\frac{x}{h}\right)^2}} + \left(\frac{x}{h}\right)^2\frac{1}{\left(1 + \left(\frac{x}{h}\right)^2\right)^{3/2}}\right\} \tag{33}$$

If the displacement is small compared to the gap height, the stiffness can be further approximated as:

$$k \approx 2\gamma \frac{w}{h} \tag{34}$$

Of interest in equation (34) is that the stiffness is only a function of the droplet width, height, and the surface tension for a droplet that has minimal surface curvature and perfectly conforms to the rectangular shape of the top cover slip.

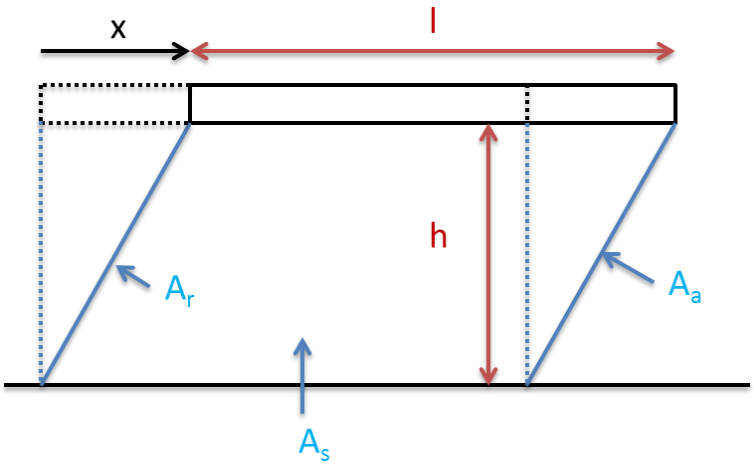

Figure 11: Droplet stiffness model schematic assuming negligible droplet surface curvature showing the droplet height (h), length (l), advancing (A_a), receding (A_r), and side areas (A_s), and displacement (x). The force required to deform the droplet can be calculated from the change in surface energy due to the surface tension and surface area change required to conserve volume.

Breakaway Force

From equation (11) the breakaway force can be modeled as a function of the width and the contact angle hysteresis between the advancing and receding surfaces. Ni *et al* [17] measured the critical contact angles for droplet motion for deionized water on Cytop coated glass substrates. From these measured surface properties summarized in Table 1, the breakaway force is modeled as:

$$F_{break} = 0.206\gamma w \tag{35}$$

Two models were proposed for static friction properties: a stiffness model based upon an assumed droplet shape and a breakaway force model based upon measured values of the critical contact angles. These two models will be compared to the testing results to determine how well they predict the actual droplet behavior.

VALIDATION

The goal of this thesis is to find a simple, one-dimensional model to predict droplet friction. To this end a series of tests were designed which varied the droplet width, length, height, and velocity while holding the acceleration and fluid, substrate, and ambient properties constant. This data is to then be correlated to hypothesized equations to predict the system performance. Three additional series of tests were conducted to determine the robustness of the data correlation and system models to changes in the system parameters away from the test points. The steady-state velocity and acceleration were changed to determine how the system would perform as the velocity approached zero, the acceleration was high enough that the steady-state velocity was reached before breakaway, and as the velocity slowly increased after droplet breakaway.

Low Speed

The testing used in the data correlation was limited to three velocities: 1 mm/s, 2 mm/s, and 4 mm/s. Two low speed validation tests were conducted to determine the effect upon the stiffness, breakaway force, and steady state force as the bulk velocity approached zero. A steady-state velocity of 0.05 mm/s with the acceleration of 10 mm/s^2 was run for droplets of 4.5 x 9 x 1.25 mm^3 and 9 x 4.5 x 1.25 mm^3.

High Acceleration

During the data correlation runs, the acceleration was held to a constant 10 mm/s^2. Two high acceleration tests were conducted to determine the effect upon the stiffness and the breakaway force of the stage acceleration. A steady-state velocity of 4 mm/s and the maximum stage acceleration of 160 mm/s^2 run for droplets of 4.5 x 9 x 1.25 mm^3 and 9 x 4.5 x 1.25 mm^3.

The combination of velocity and acceleration ensured that the stage had reached steady-state velocity before the droplets started motion.

Ramping Velocity

During the data correlation runs, the velocity was held constant after the initial acceleration so that the steady-state data could be averaged for the velocity test point. The final validation test was to slowly ramp the bulk velocity while the droplets were in motion to determine if the steady-state data would be valid for transient velocities. The maximum velocity was set for 4 mm/s with an acceleration of 0.5 mm/s^2 for droplets of 4.5 x 9 x 1.25 mm^3 and 9 x 4.5 x 1.25 mm^3.

RESULTS & CONCLUSIONS

The goal of this thesis is to find a simple, one-dimensional model to predict droplet friction. To determine the component of the static and dynamic friction on a droplet as a function of the droplet width, length, height, and velocity, the test were run varying these parameters and the results were correlated to the hypothesized equations using the procedure outlined in the testing section. Additional validation test runs were conducted to see the effect of the velocity and acceleration for data points away from the standard test values. These results were then compared to the two proposed models predicting the droplet stiffness and breakaway force.

Stiffness

Testing Results

As shown in Figure 12, the stiffness data followed the hypothesized trends of increasing with the cover slip width and decreasing with gap height. Using the data regression technique, the stiffness constant in equation (14) was found to be:

$$k = 1.47\gamma\frac{w}{h} \tag{36}$$

The average error was for the correlation was -3.0% with a standard deviation of 7.8%. The largest source of error in the correlation was due to the variation in the stiffness with the bulk velocity. This can be seen in the vertical spread for each geometry group in Figure 12. Figure 13 shows the stiffness versus velocity for the 4.5 x 9 x 1.25 mm^3 and 9 x 4.5 x 1.25 mm^3 (w x l x h) droplet testing results in addition to the low velocity and high acceleration validation runs. While Figure 13 shows some variation of the stiffness with the bulk velocity, of more significance is the increase in the standard deviation with the increased bulk velocity for the test data as the variation of the stiffness with the velocity is negligible above 1 mm/s. As will be explained further in the error sources section, for the higher velocity test runs the instantaneous acceleration rate

varied and was observed to affect the stiffness. It is believed that this is the main source of the error in the stiffness data from the correlation.

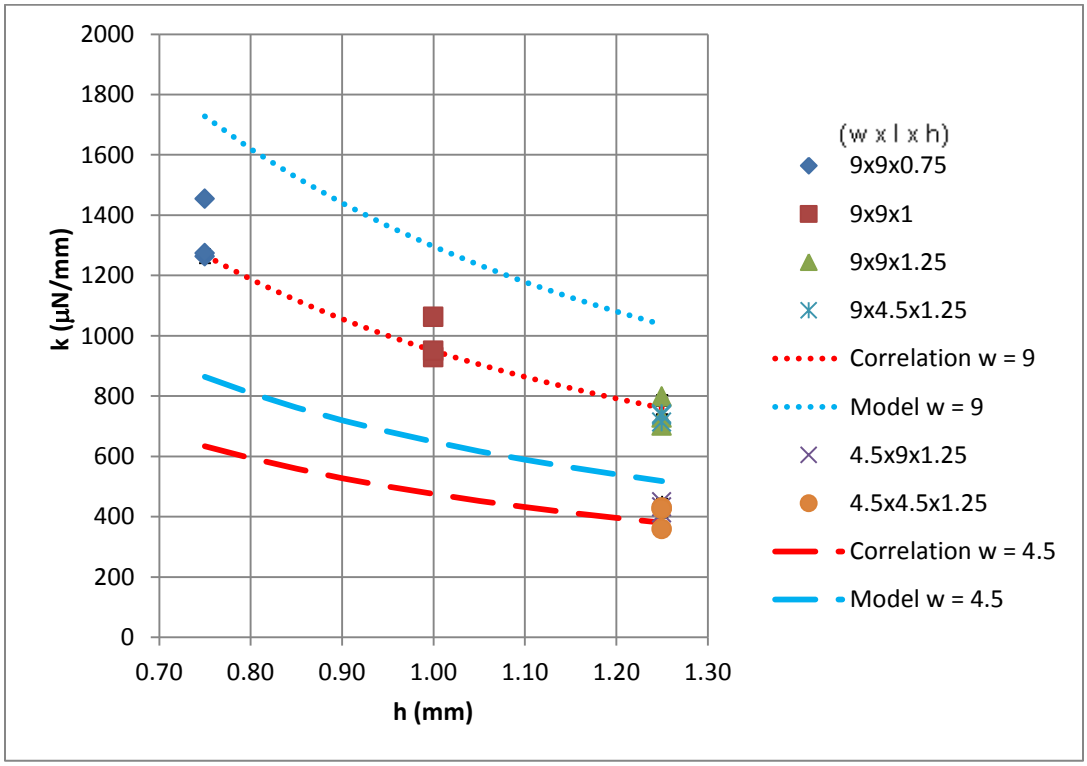

Figure 12: Stiffness test data versus gap height for 9 mm and 4.5 mm wide data. Results are compared to correlation and model curves for cover slip width of 9 & 4.5 mm. Data correlates well with hypothesized stiffness equation with error due to velocity from acceleration control.

Modeling Results

While the model showed the same trend in stiffness with the width and height as the test data, it over predicted the stiffness as compared to the correlation by 36%. This over prediction is in agreement with previous attempts modeling attempts [7, 16] and it has been shown that the error increases with the gap height [16] as the negligible surface curvature assumption begins to break down. The average error for the stiffness model compared to the individual test results was 32.3% with a standard deviation of 10.6%.

Table 3 summarizes the stiffness test results and compares the results to the data correlation and stiffness modeling.

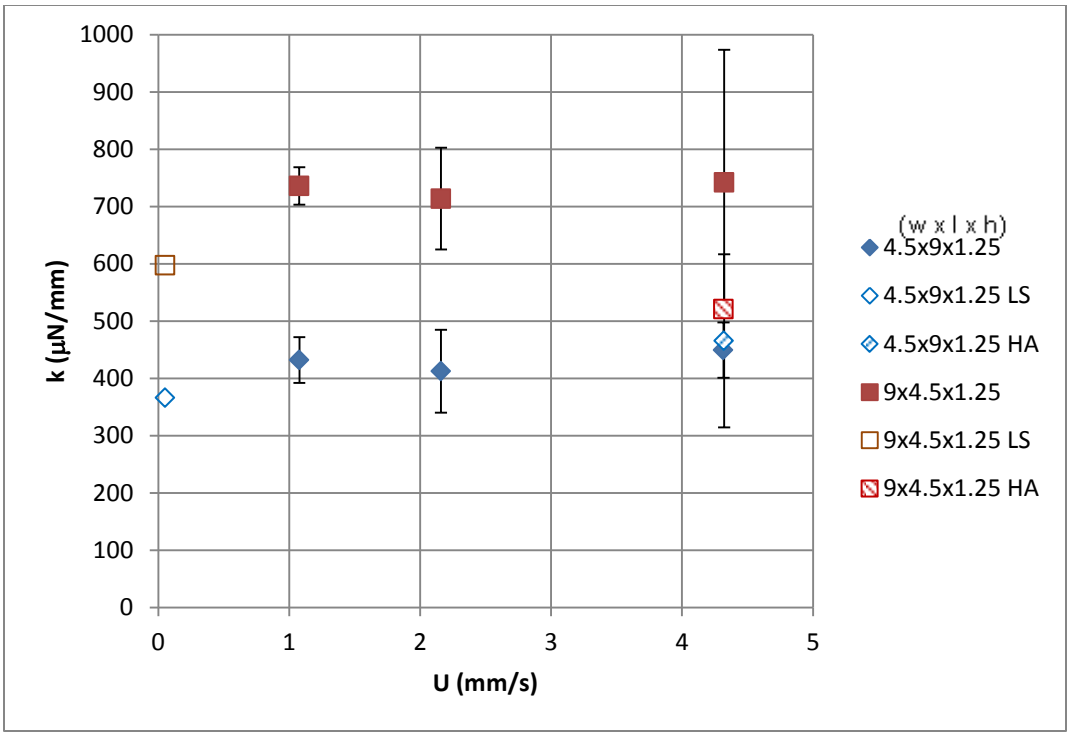

Figure 13: Stiffness variation with bulk velocity for test data and low velocity and high acceleration validation runs for 4.5 x 9 mm^2 and 9 x 4.5 mm^2 cover slips. Results show little velocity dependence above 1 mm/s and increasing error with velocity due to stage control error.

Table 3: Stiffness testing, correlation, and modeling results

Test #	w mm	l mm	h mm	U mm/s	Data μN/mm	Corr. μN/mm	Error %	Model μN/mm
1	9	9	0.75	1.08	1455	1267	-12.9%	1728
2	9	9	0.75	2.16	1263	1267	0.3%	1728
3	9	9	0.75	4.32	1274	1267	-0.5%	1728
4	9	9	1	1.08	1063	950	-10.6%	1296
5	9	9	1	2.16	929	950	2.3%	1296
6	9	9	1	4.32	950	950	0.0%	1296
7	9	9	1.25	1.08	798	760	-4.8%	1037
8	9	9	1.25	2.16	728	760	4.4%	1037
9	9	9	1.25	4.32	702	760	8.2%	1037
19	4.5	9	1.25	1.08	432	380	-12.1%	518
20	4.5	9	1.25	2.16	413	380	-7.9%	518
21	4.5	9	1.25	4.32	449	380	-15.4%	518
22	9	4.5	1.25	1.08	736	760	3.3%	1037
23	9	4.5	1.25	2.16	714	760	6.5%	1037
24	9	4.5	1.25	4.32	742	760	2.5%	1037
28	4.5	4.5	1.25	1.08	430	380	-11.6%	518
29	4.5	4.5	1.25	2.16	426	380	-10.8%	518
30	4.5	4.5	1.25	4.31	360	380	5.6%	518

Breakaway Force

Testing Results

While the largest contributor to the breakaway force was the width as predicted by the hypothesis, the height of the droplet also had a significant contribution with the force increasing with droplet height, as shown in Figure 14. The contact angle hysteresis model for the breakaway force is based upon measurements and behavior of sessile droplets. As the gap height to cover slip width ratio increases, the disturbance in the shape due to the cover slip is minimized and the droplet shape begins to approach that of a sessile droplet. As the height decreases versus the width, the impact of the cover slip on the droplet shape increases and the droplet shape becomes closer to the assumed rectangular prism shape [7]. It is believed that the increase in the total droplet surface energy as it is forced to wet the hydrophobic substrate and deviates away from the minimum surface energy sessile shape acts to lower the energy barrier and therefore the forced needed to move the contact lines.

In addition to variation with the gap height, error can also be attributed to the bulk velocity as shown by the vertical spread in the geometry groups in Figure 14. Figure 15 suggests that the breakaway force has a small dependency upon the velocity and is similar in nature to the dynamic force as shown later. It is believed that this is due the internal flow of the droplet just prior to movement affecting the contact line equilibrium. It should also be noted that there is some error associated in the velocities listed when the droplet motion starts due to the error in the acceleration noted earlier.

Using the data regression technique, the breakaway force constant in equation (15) was found to be:

$$F_{break} = 0.177\gamma w \tag{37}$$

The average error was for the correlation was 1.1% with a standard deviation of 14.4%.

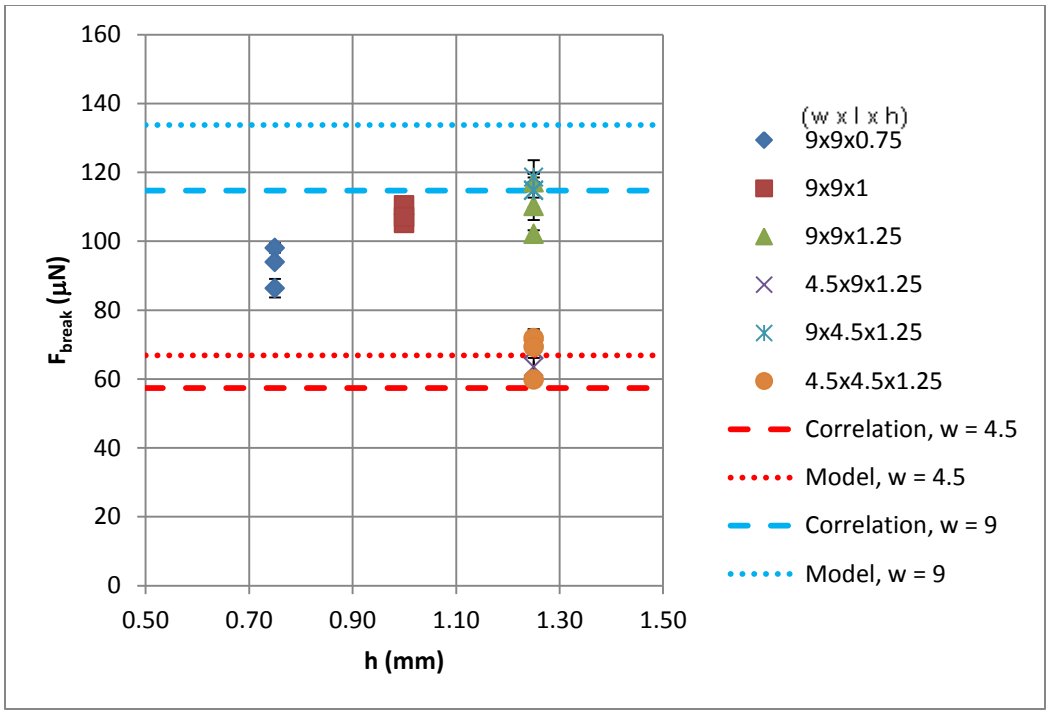

Figure 14: Breakaway force variation with gap height for test data with correlation and model curves. Thicker droplets and smaller widths approach model predictions.

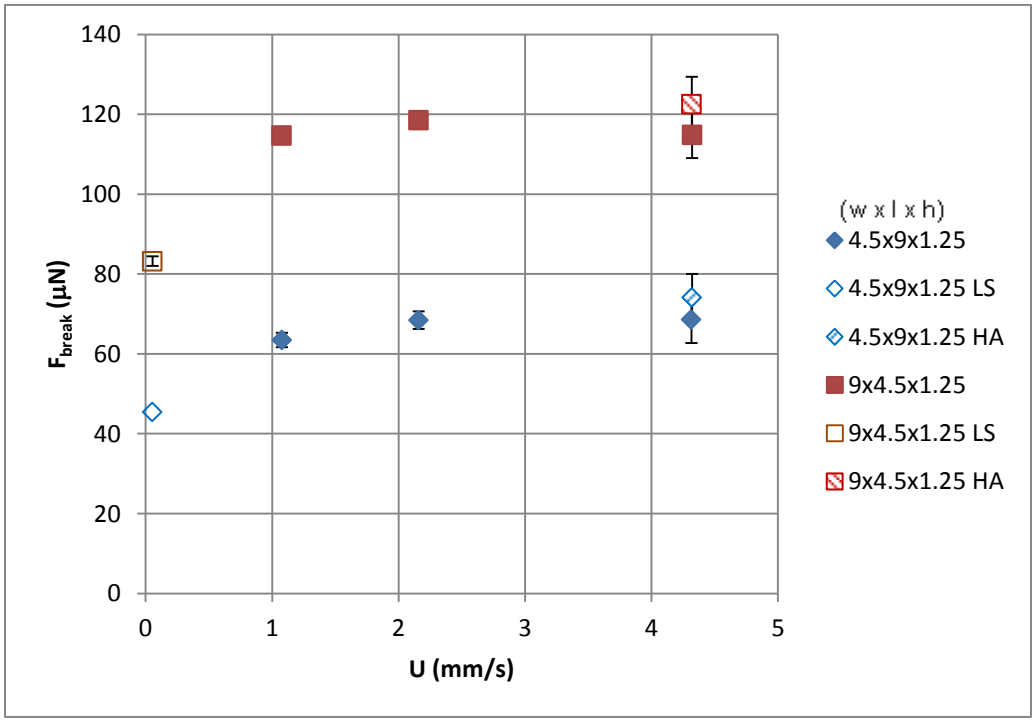

Figure 15: Breakaway force variation with bulk velocity for test data and low velocity and high acceleration validation runs for 4.5 x 9 mm^2 and 9 x 4.5 mm^2 cover slips. Shows increase in breakaway force with velocity. Error due to stage control is apparent for higher velocity tests.

Modeling Results

The contact angle hysteresis model over predicts the breakaway force by 16% when compared to the data correlation. Interestingly, the error decreases with the width and provides a good fit for the 4.5 mm widths. This result is counter intuitive as error in the droplet shape due to the inability to wet to the corner of the cover slip should be magnified as the width decreases. It is possible that the ratio of the droplet height to width plays an important role how closely the droplet conforms to the contact angle hysteresis model in the breakaway behavior, but the 9mm breakaway forces were closer to prediction values for larger thicknesses as well. More data is needed to draw solid conclusions on this relationship and to develop a more robust correlation. Table 4 summarizes the test results, and compares the results to the data correlation, and stiffness modeling.

Table 4: Breakaway force testing, correlation, and modeling results

Test #	w mm	l mm	h mm	U mm/s	Data μN	Corr. μN	Error %	Model μN
1	9	9	0.75	1.08	86.3	115	32.8%	134
2	9	9	0.75	2.16	98.1	115	17.0%	134
3	9	9	0.75	4.32	93.9	115	22.1%	134
4	9	9	1	1.08	105.2	115	9.0%	134
5	9	9	1	2.16	110.4	115	3.9%	134
6	9	9	1	4.32	107.0	115	7.2%	134
7	9	9	1.25	1.08	102.1	115	12.3%	134
8	9	9	1.25	2.16	117.0	115	-2.0%	134
9	9	9	1.25	4.32	110.2	115	4.0%	134
19	4.5	9	1.25	1.08	63.4	57	-9.6%	67
20	4.5	9	1.25	2.16	68.4	57	-16.2%	67
21	4.5	9	1.25	4.32	68.6	57	-16.4%	67
22	9	4.5	1.25	1.08	114.7	115	0.0%	134
23	9	4.5	1.25	2.16	118.5	115	-3.3%	134
24	9	4.5	1.25	4.32	114.8	115	-0.1%	134
28	4.5	4.5	1.25	1.08	71.8	57	-20.1%	67
29	4.5	4.5	1.25	2.16	69.3	57	-17.3%	67
30	4.5	4.5	1.25	4.31	59.9	57	-4.2%	67

Static System Properties Relationship

It is observed that droplet stiffness and breakaway force show similar trends with respect to the variable system parameter. Figure 16 shows the breakaway force normalized by the width decreases with increasing droplet stiffness. It is believed that this is due to the change in the curvature in the droplet surface. As the ratio of the gap height to cover slip width increases, the curvature increases approaching the minimum surface energy shape without the effect of the presence of the cover slip. As the ratio decreases, the droplet surfaces become flatter, effectively preloading the droplet by increasing the surface energy and requiring less work to overcome the energy barrier required to move the contact lines. As the model is based upon the critical contact angles measured for sessile droplets, the model predicted breakaway force is approached as the stiffness decreases and the droplet curvature is more pronounced.

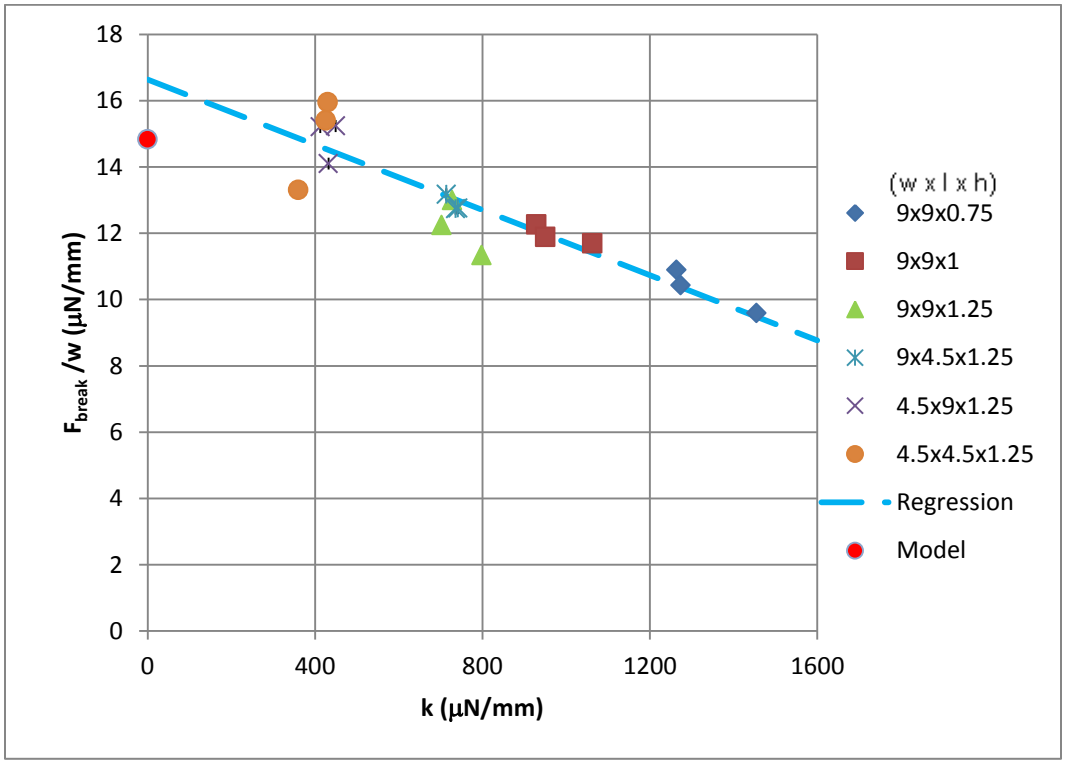

Figure 16: Breakaway force normalized by width versus stiffness with data regression showing linear trend. As stiffness decrease, breakaway force approaches model prediction

Dynamic Force

The dynamic force data follow the hypothesized trends of increasing with the width and bulk velocity, as shown in Figure 17. However, as with the breakaway force, the dynamic force also unexpectedly increased with the gap height as shown in Figure 18. Also, there was no correlation between the force and the area of the cover slip.

Using the data regression technique, the dynamic force constants in equation (21) were found to be:

$$F_{dyn} = 0.154\gamma w + 0.728Uw + 0.000\mu\frac{U}{h}wl \tag{38}$$

The average error was for the correlation was -1.2% with a standard deviation of 9.8%. Table 5 summarizes the test results and compares the results to the data correlation. Also shown in Table 5 are the individual force components for the correlation with their percent contribution to the total.

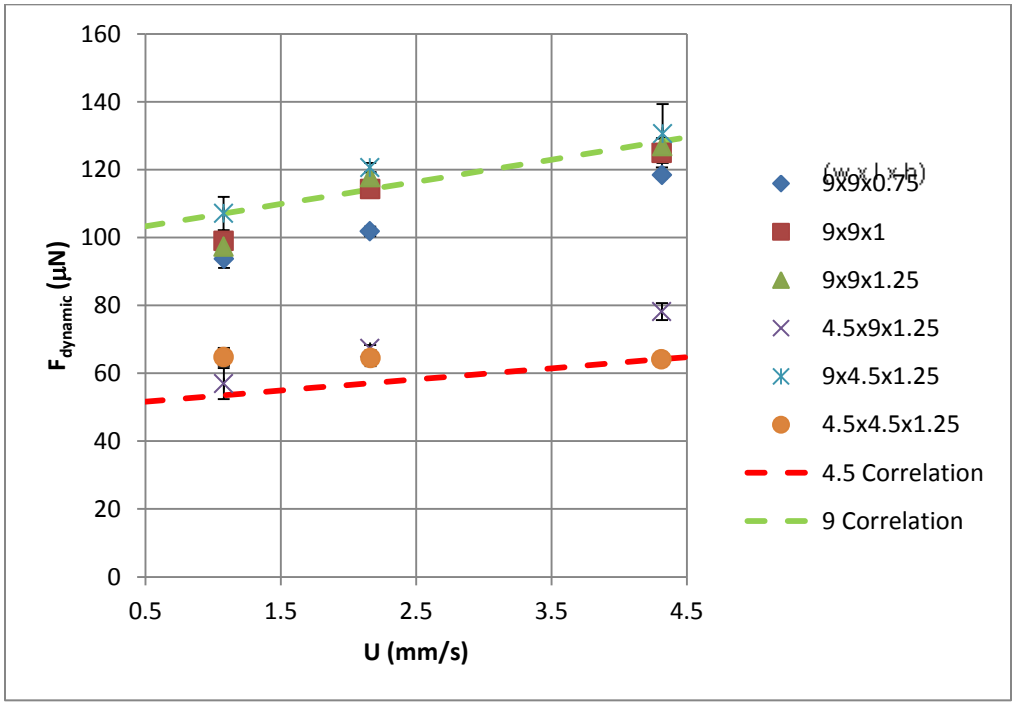

Figure 17: Steady-state force variation with bulk velocity for test data with correlation curves for 4.5 and 9 mm cover slip widths. A slight increasing trend in force is observed with velocity. Spread in force due to unknown contribution of height is also shown.

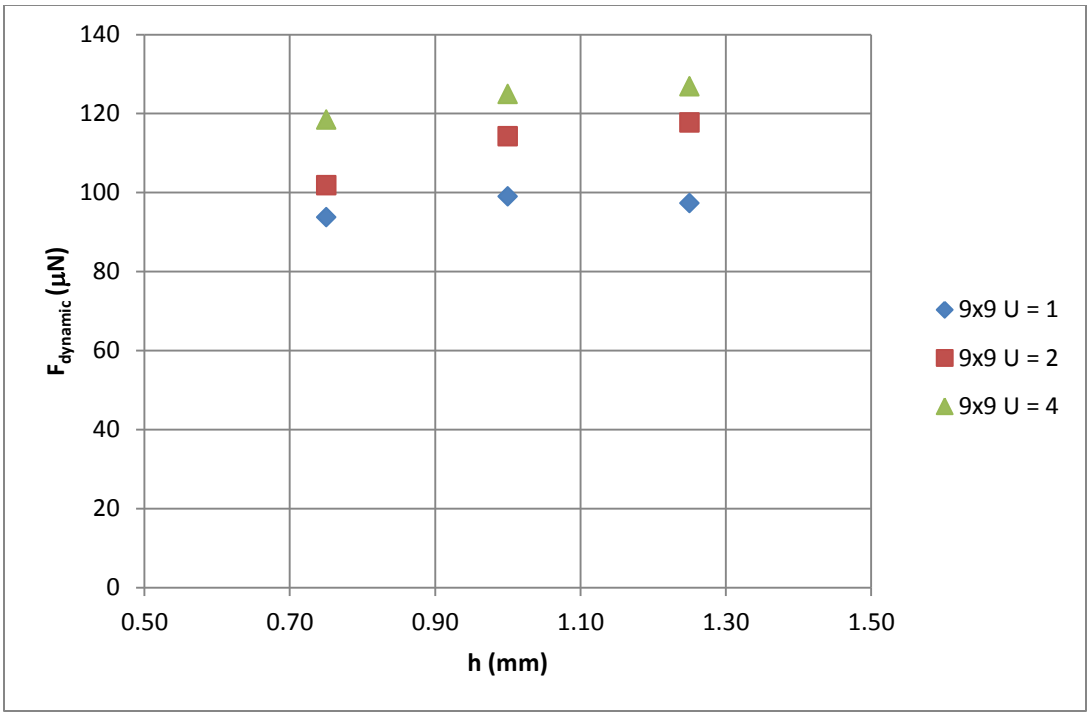

Figure 18: Dynamic force variation with gap height for 9 x 9 mm^2 cover slips showing slight trend of increasing force with gap height for constant velocity data groups. The opposite trend was expected due to increasing viscous loss contribution due to increasing velocity gradient with decreasing height.

Table 5: Dynamic force testing and correlation

Test #	w mm	l mm	h mm	U mm/s	Data µN	Corr. µN	Error %	F_{CA} µN	F_{CA}/F_{dyn} %	F_{CL} µN	F_{CL}/F_{dyn} %	F_{vis} µN	F_{vis}/F_{dyn} %
1	9	9	0.75	1.08	94	107	14.3%	100	93.4%	7	6.6%	0	0.0%
2	9	9	0.75	2.16	102	114	12.1%	100	87.6%	14	12.4%	0	0.0%
3	9	9	0.75	4.32	118	128	8.3%	100	78.0%	28	22.0%	0	0.0%
4	9	9	1	1.08	99	107	8.2%	100	93.4%	7	6.6%	0	0.0%
5	9	9	1	2.16	114	114	-0.1%	100	87.6%	14	12.4%	0	0.0%
6	9	9	1	4.32	125	128	2.7%	100	78.0%	28	22.0%	0	0.0%
7	9	9	1.25	1.08	97	107	10.1%	100	93.4%	7	6.6%	0	0.0%
8	9	9	1.25	2.16	118	114	-3.0%	100	87.6%	14	12.4%	0	0.0%
9	9	9	1.25	4.32	127	128	1.1%	100	78.0%	28	22.0%	0	0.0%
19	4.5	9	1.25	1.08	57	54	-6.0%	50	93.4%	4	6.6%	0	0.0%
20	4.5	9	1.25	2.16	67	57	-15.2%	50	87.6%	7	12.4%	0	0.0%
21	4.5	9	1.25	4.32	78	64	-17.9%	50	78.0%	14	22.0%	0	0.0%
22	9	4.5	1.25	1.08	107	107	0.0%	100	93.4%	7	6.6%	0	0.0%
23	9	4.5	1.25	2.16	121	114	-5.3%	100	87.6%	14	12.4%	0	0.0%
24	9	4.5	1.25	4.32	131	128	-1.8%	100	77.9%	28	22.1%	0	0.0%
28	4.5	4.5	1.25	1.08	65	54	-17.4%	50	93.4%	4	6.6%	0	0.0%
29	4.5	4.5	1.25	2.16	64	57	-11.4%	50	87.6%	7	12.4%	0	0.0%
30	4.5	4.5	1.25	4.31	64	64	0.0%	50	78.0%	14	22.0%	0	0.0%

To verify that the discrete test points accurately represented the relationship between the velocity and the steady-state force a ramping velocity validation test was conducted for the 9 x 4.5 x 1.25 mm^3 droplet. The slope of the correlation line in Figure 19 shows a good correlation to the test data and validation run. The offset between the test and validation data is most likely due to error from the substrate surface properties (Note: the spikes in data sets d and e are due to electrical connection issues not droplet instability).

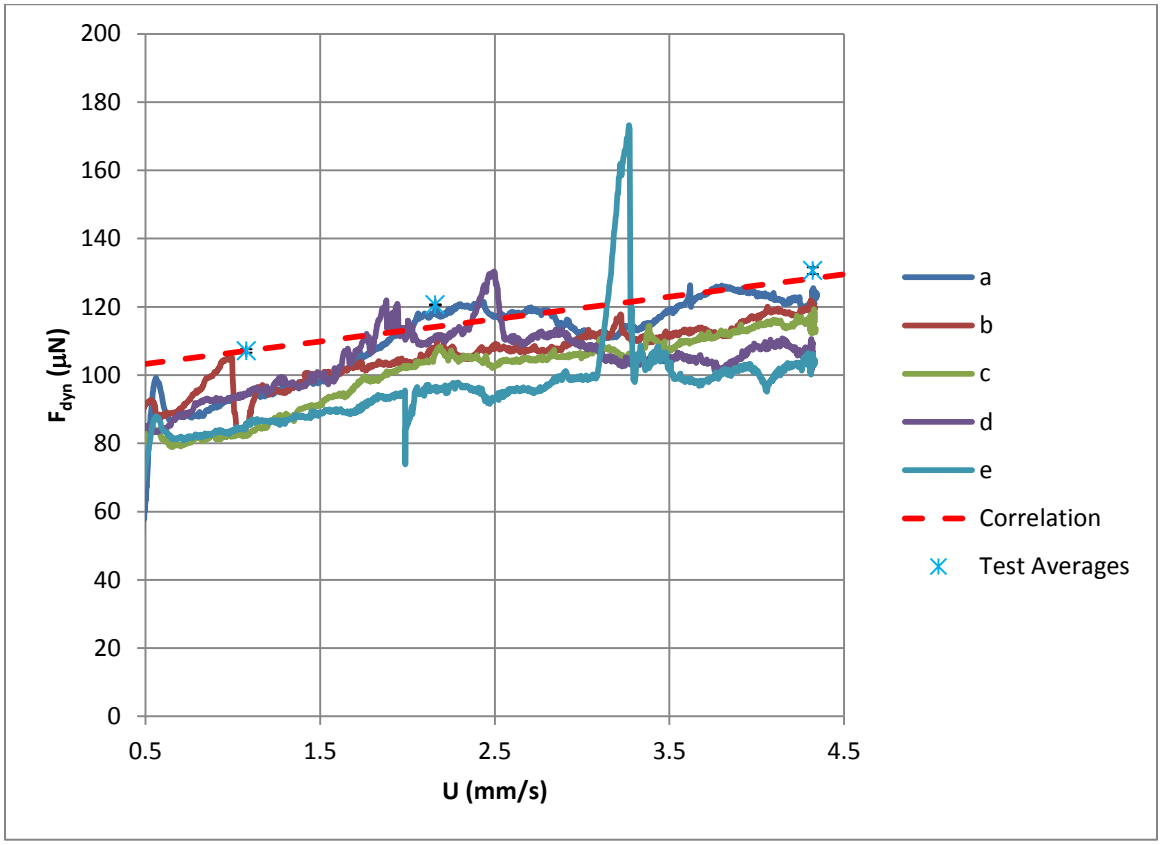

Figure 19: Ramped bulk velocity for 9 x 4.5 x 1.25 mm^3 droplet with test data and correlation showing good agreement with slope.

Equation (38) showed no correlation between the dynamic force and the hypothesized viscous loss. This result can be explained by a simple dimensional analysis. From equation (20), the maximum contribution of the viscous force for the variable system parameters should be:

$$F_{vis} = C_3 \left(1.00 \cdot 10^{-3} \frac{\mu N \cdot s}{mm^2}\right) \frac{4.0 \frac{mm}{s}}{0.75\ mm} (9\ mm)(9\ mm) = 0.432 C_3\ \mu N \tag{39}$$

For the viscous force to approximately equal the smallest force contribution on Table 5 of 4 μN, C_3 would be approximately 9 which is 50% greater than the typical channel flow the velocity gradient factor of 6 [1].

Additionally, the hypothezied dynamic force equation (21) predicted that the force should decrease with increasing height. As shown in Figure 18, the opposite case is true for the range of gap heights tested. The viscous loss component of the dynamic force is not zero but is smaller than the experimenal variation of the force and the equation used to correlate the data did not predict the proper trend with the gap height, therefore the regression found the viscous force constant to be zero.

Data summary for each individual test run and plot of the force versus the displacement can be found in the appendices.

Comparison of Static and Dynamic Friction

As would be expected, the general trend for the friction forces for a droplet is an increase in the dynamic steady-state force with the static breakaway force, as shown in Figure 20. Figure 21 shows the ratio of the dynamic force to the breakaway force as a function of the bulk velocity. As the velocity decreases the ratio of the dynamic force to the breakaway force decreases as expected as would be expected by force equations (9) and (21). As the velocity decreases the dynamic contact angles should approach the critical static contact angle per the relationship (1) and the ratio of the forces should approach unity. However, the dynamic force was less than the measured breakaway force for all but one test group at U = 1 mm/s and for two test groups at U = 2 mm/s. This result suggests that the velocity effect upon the contact angles is greater before contact line motion than after the droplet movement. However, further study with better stage acceleration control is needed before definite conclusions can be drawn.

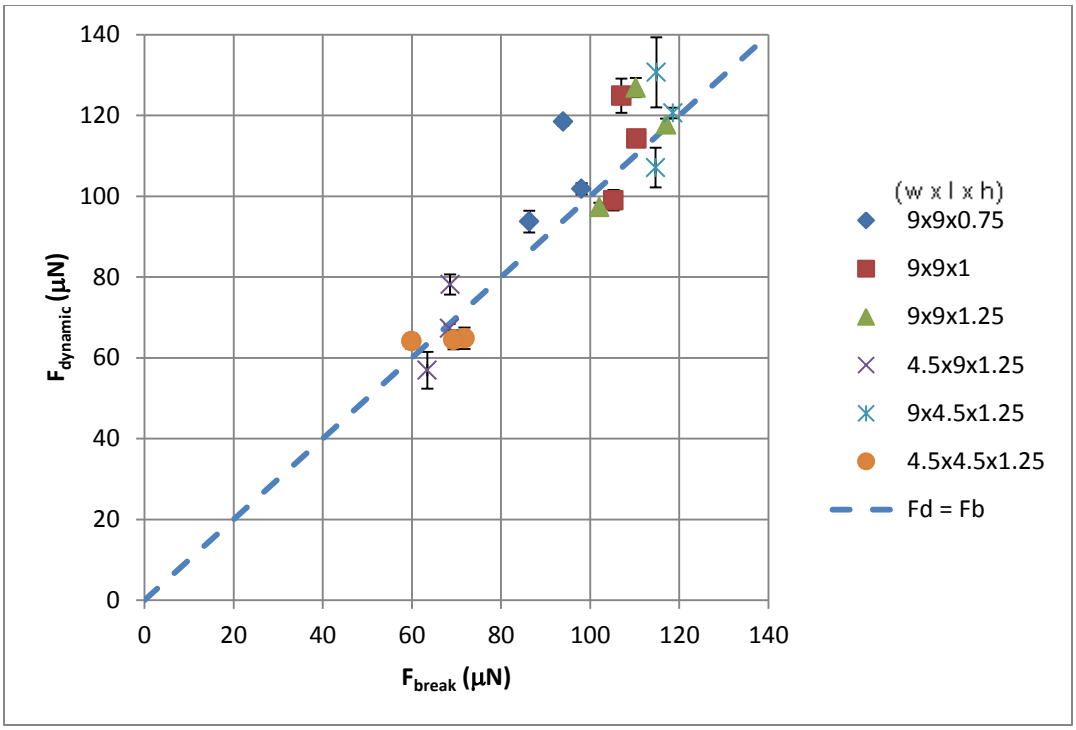

Figure 20: Dynamic versus breakaway force showing the general increasing trend of dynamic force with breakaway force. The grouping of data points near the Fd=Fb line shows that they were nearly equivalent for most tests.

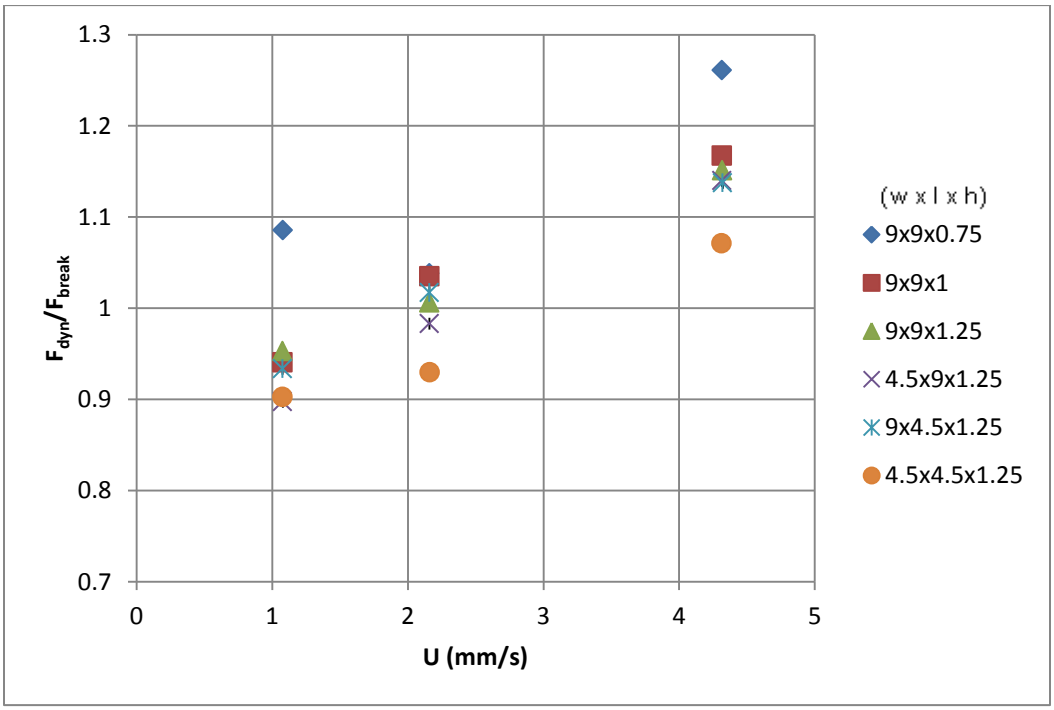

Figure 21: Ratio of dynamic force to breakaway force versus velocity. Several of the test groups go below unity, the expected minimum value due to contact angle velocity relationship.

Comparison to Previous Work

Ren *et al* [2] determined the power dissipation for a droplet between two parallel plates in an oil ambient actuated by electrowetting due to the combined viscous friction force, the viscous drag from the oil, and the contact line friction (equation (4)). By varying the droplet viscosity, oil viscosity, and velocity, they found that the contact line friction coefficient (C_{vis}) to be 0.04 μN*s/mm^2. Though this value is an order of magnitude smaller than the calculated value of 0.728 μN*s/mm^2 found here, the percent contributions of the components of the dynamic friction are similar with approximately 77% due to the dynamic contact angle force (F_{CA}), approximately 14% due to contact line friction (F_{CL}), and 9% due to drag due to the oil ambient, versus 86% due to dynamic contact angle force (F_{CA}), 14% due to contact line friction (F_{CL}), and 0% assumed drag as air is the ambient in this testing. The discrepancy in the contact line friction coefficient could be due to scaling issues as the droplet volumes tested by Ren *et al* were on the order of one magnitude smaller and the velocities one to two orders of magnitude larger.

Stability

As previously noted in the analysis section, for several testing runs large increases in the steady-state force were seen. These spikes in force data were observed after the flow had developed and reached a steady state. The goal of better understanding these phenomena motivated the use of camera to record testing runs. From the video, two instability modes were identified: cover slip tilting (rotation about the y-axis) and cover slip yawing (rotation about the z-axis), as illustrated in Figure 22. It was observed from the test data that the onset of the stability issues would occur at approximately one cover slip length as illustrated in Figure 23 and Figure 24.

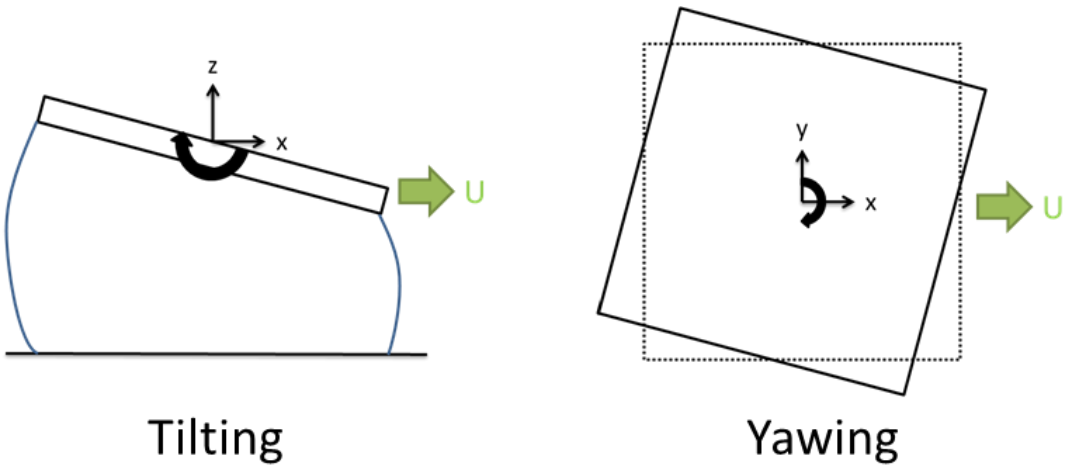

Figure 22: Tilting (rotation around y-axis) and yawing (rotation around z-axis) instability modes

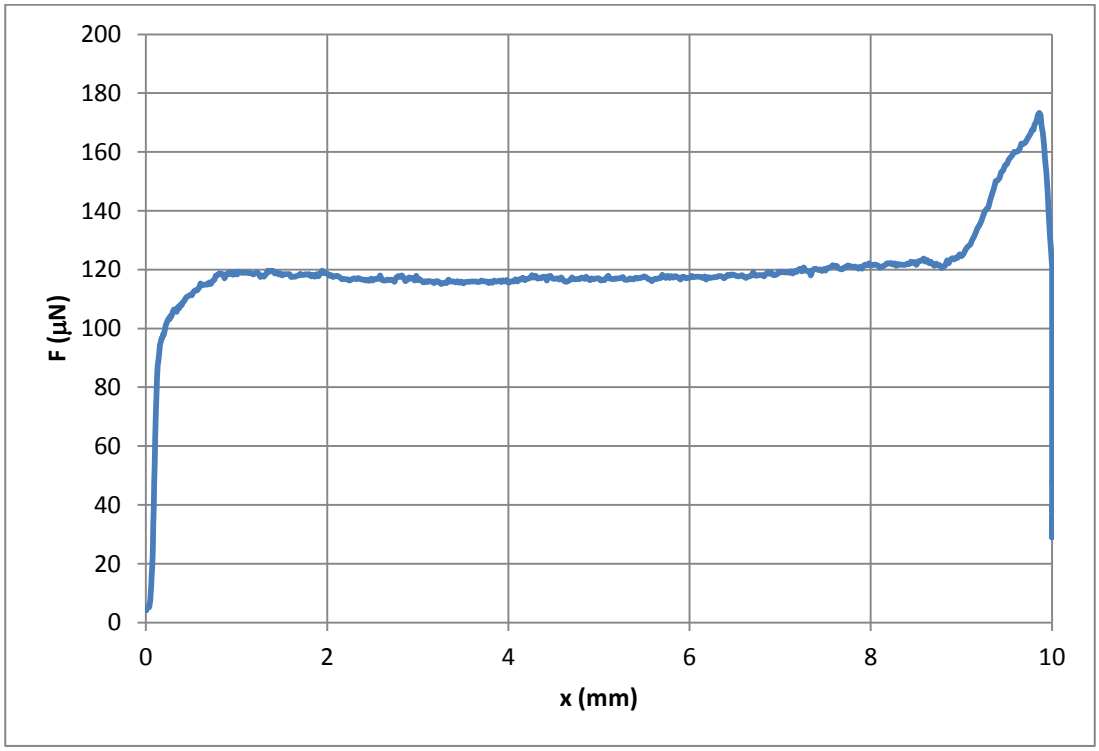

Figure 23: Tilt instability onset at approximately x = 9 mm for 9 x 9 x 0.75 mm^3 droplet

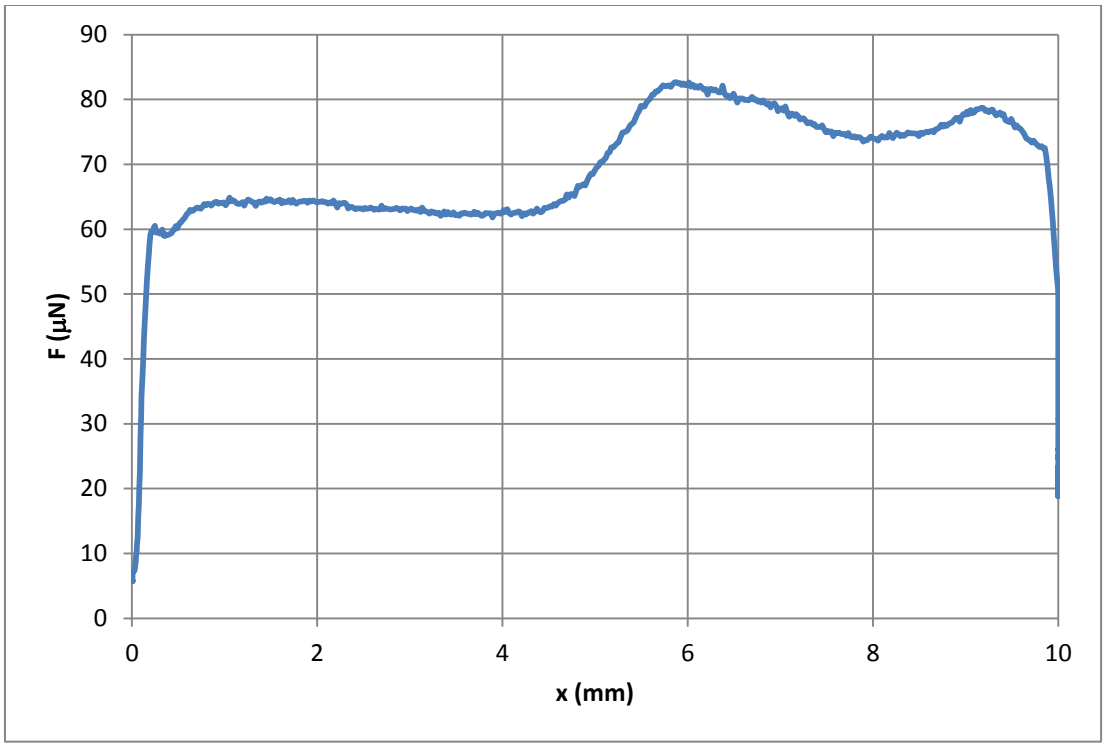

Figure 24: Yaw instability onset at approximately x = 4.5 mm for 4.5 x 4.5 x 1.25 mm^3 droplet

Tilting

The most common mode of instability observed was the tilting of the cover slips on the droplet. Berthier *et al* noted in their paper on self-alignment of silicon chips on fluids, that when height to length ratio is on the order of one, tilting of the chip is more pronounced and more likely to lead to the sliding of the chip to the edge of the fluid [7]. By using an energy analysis of the change in surface areas it was shown that the tilting is slightly unstable [7].

In this testing, even before displacement of the cover slip, small tilt angles were observed when cover slip placed on droplet. However, small changes in tilt angle that occurred during runs had little effect on the force measurements. The large spikes occurred only for large tilt angles with respect to the substrate. For these extreme cases the cover slip would move to the advancing edge of the droplet. It is possible the large forces were due to the cover slip contacting the substrate; however this is inconclusive from the video of the testing.

Yawing

The yawing mode was less common than the tilting mode and resulted in smaller instability forces. The yawing mode oscillatory in nature and it is theorized that it can be attributed to asymmetrical wetting of cover slip as it was mostly eliminated by careful placement of cover slip on droplet, insuring full wetting. The effect of the yawing mode was more pronounced for the smaller cover slips. This is supported by Berthier *et al* as they showed that the restoring torque associated with the twisting action decreases with increase of height to length ratio [7].

Flow Visualization

Motivated by questions about cover slip instability and the underlying causes (possibly related to the internal flow of the droplet) and to help with understanding the velocity gradient for the viscous loss modeling, flow visualization by the use of a visible dye was conducted for a small number of geometries. A small droplet of methyl blue stain was placed in the center of the path of droplet so that the water would pick up the dye after movement had started so that the dye would not diffuse beforehand.

It was originally assumed that the flow inside the droplet could be approximated by a simple two dimensional flow model; however it was readily apparent through the dye testing that the flow was heavily three dimensional in nature. The dye stayed in place on substrate (as would be expected from a boundary condition at a wall) until picked up by trailing contact line. The dye was then rapidly circulated around the free edge of the droplet to front and middle of advancing edge. The forward circulation velocity was observed to be much greater than stage velocity. It was also noted that the dye had a tendency to stick to substrate when it met the receding surface of the fluid, causing the surface to deform. This phenomenon could be related to the relative difference in the wettability of the dye and the water as the static contact angle of the dye was found to be 99 degrees versus 111 for the water.

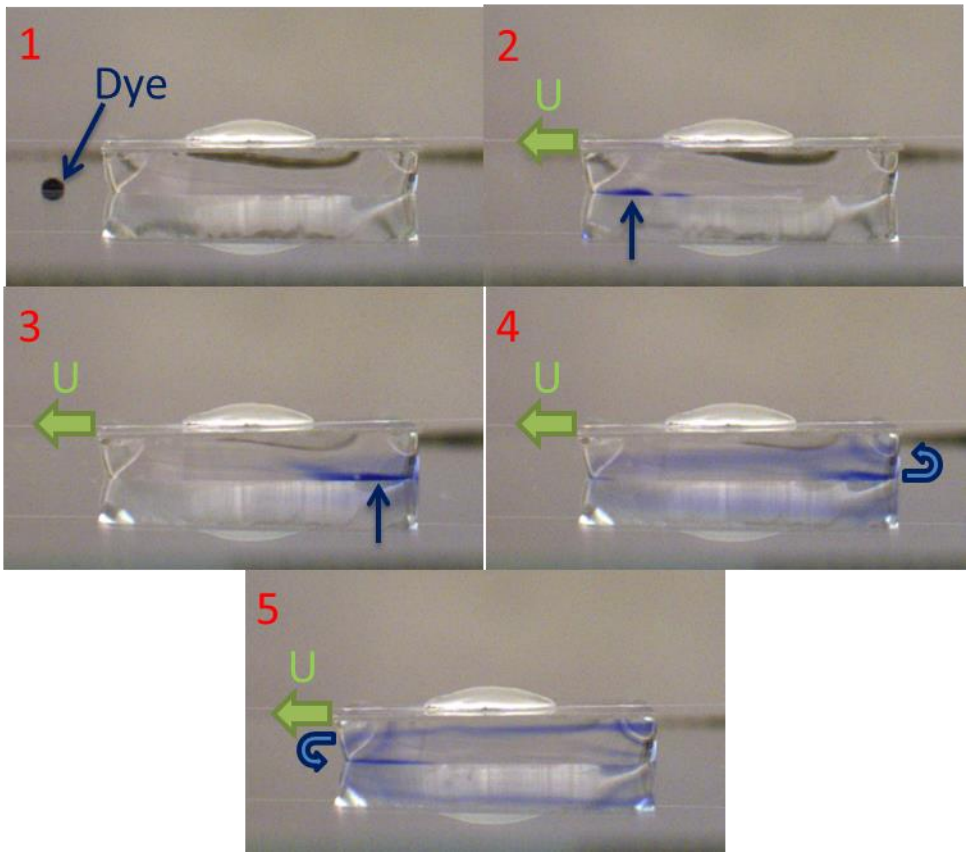

Figure 25: Dye visualization. 1) Initial position with dye in front of droplet, 2) Dye enters droplet and maintains initial position as droplet travels forward, 3) Dye reaches receding contact line, 4) Dye is picked up off of substrate and is circulated to side surface and then forward to advancing edge of droplet, 5) Dye is deposited on to substrate at advancing contact line

Summary

It was found that the hypothesized static and dynamic force equations, (15) & (21) represented the largest component of droplet friction, the contact angle force, adequately. Small errors were seen due to an unexpected dependency on height in both cases, and the velocity for the static force. Both the stiffness and breakaway force models over predicted the test values but showed the proper trends seen in the data.

ERROR SOURCES

The goal of this thesis is to find a simple, one-dimensional model to predict droplet friction. During the testing and analysis phases used to determine the static and dynamic components of the droplet friction, several possible error sources arose. These error sources can be broken down into three groups: underlying assumptions used derive the hypothesized equations, error in the testing procedure, and calculation errors during the analysis.

Assumptions

Inertial Forces

One of the underlying assumptions in this analysis is that the inertial forces are insignificant compared to the forces arising from the surface tension and the viscous losses in the fluid. Two non-dimensional parameters are used to relate these forces: the Weber number and the Reynolds number.

The Weber number is the ratio between the inertial and surface tension forces given by [5], [32]:

$$We = \frac{\rho U^2 l}{\gamma} \tag{40}$$

For the range of velocities and cover slip sizes used in the testing the Weber number was on the order of 10E-2 indicating that the surface tension forces were much larger than those arising from the inertial effects.

The Reynolds number is the ratio between the inertial and viscous forces given by:

$$Re = \frac{\rho U l}{\mu} \tag{41}$$

For the range of velocities and cover slip sizes used in the testing the Reynolds number was on the order of 10E1 indicating that the viscous forces were much larger than those arising from the inertial effects.

Additionally, an approximation of the inertial force on the droplet during acceleration can be found by:

$$F = ma = \rho \forall a \tag{42}$$

For a 100 μL droplet of water at the test acceleration of 10 mm/s^2, the inertial force is approximately 1 μN.

However, it was noted that the instantaneous apparent stiffness of the droplet was affected by the acceleration rate of the stage. As the average acceleration rate was constant, it is assumed that the average stiffness for a run is also constant. This phenomenon will be discussed in further detail later.

Flow Profile

Another underlying assumption used in the analysis of the testing was that of the flow profile inside the droplet and its respective gradient. The velocity used to characterize contact line friction and the viscous losses of the system was that of the bulk droplet velocity. From the dye flow visualization, it was apparent that the 3-D nature of the flow leads to maximum velocity greater than the bulk velocity and is dependent upon the droplet geometry. The flow profile would also suggest that the velocity gradient at the substrate is not constant and can vary significantly due to the circulation around the droplet. However, as shown by the results, the viscous loss is not a significant factor in the total friction force for the configurations tested.

In future testing if the viscous losses are a larger contributing factor, another suitable approximation for the velocity profile will be needed to address these issues [5]. CFD modeling of flow is one avenue which could help create a relationship for a characteristic velocity to the geometry.

Droplet Shape

An assumed droplet shape of a rectangular prism was used throughout the analysis. This assumption was used for calculating the gap height based upon the droplet volume and for the wetted area of the substrate. In actuality, the droplet has curved surfaces which results in errors in these assumed values. The droplet conforms to the contact line equilibrium conditions and to minimize the surface energy may cause the wetted area on the substrate to be different from that of the cover slip. This causes an error in the height calculation. There are also slight errors in the wetted area of the cover slip as the droplet cannot wet to corners [7].

The droplet shape was assumed to maintain the static geometry during the dynamic motion. This assumption is not entirely true as the droplet shape can be deformed by forces acting on it [4] as it tries to satisfy changing contact line conditions and internal flow conditions. However, the droplet shape can be treated as quasi-static as the surface deformations occur at a much faster time scale than that of the bulk motion of the droplet [7, 4].

Displacement Approximation

The varying amounts of initial slack in the fiber caused a lag between the initiation of the relative cover slip displacement and the movement of the substrate. Additionally the slack caused an apparent softening of stiffness of the droplet as tension was gradually applied to the fiber. To account for both of these issues, a linear approximation using the stiffness of the droplet was used to calculate where the initiation of the cover slip displacement would occur if the fiber was perfectly rigid. While this would result in errors in the force/displacement relationship, the calculation of the droplet stiffness should have minimal error as it was calculated after the fiber slack affects had settled.

Testing Error

Fiber Tension

Before each testing run, the fiber connecting the cover slip to the force sensor was slacked to allow the droplet to return to an equilibrium position and to allow the sensor to start as near it zero as possible. However, due to the weight of the fiber, some residual tension will always remain [33]. To correct for this the force data was calculated relative to the sensor zero voltage not the initial sensor voltage. It is assumed that the residual tension and resulting deformation of the droplet does not affect the stiffness or the breakaway force of the droplet. Figure 26 shows a run in which the tension was not released with and without the correction from the zero sensor voltage compared to the rest of the test group data. The error in the stiffness, breakaway force, and steady-state force as compared to the group average was -11%, 2%, and 2% respectively.

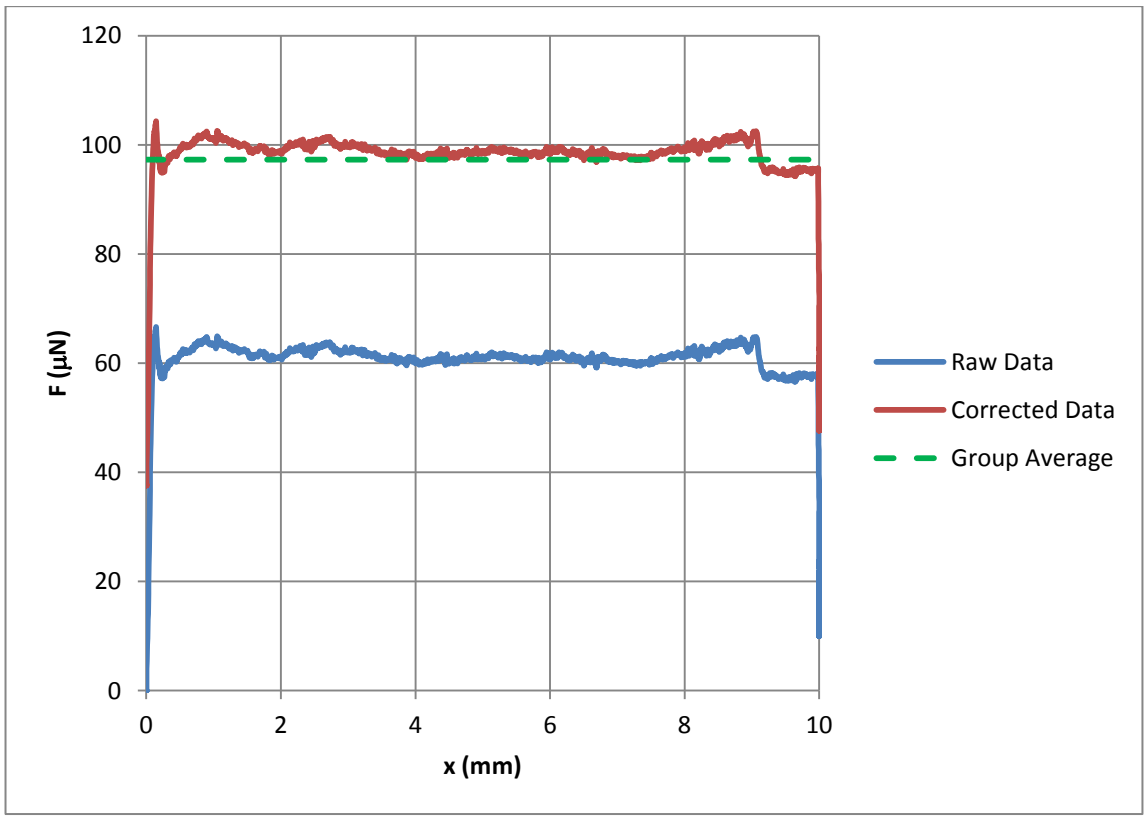

Figure 26: Tension error example showing raw and corrected data.

Acceleration and Velocity Errors

To reduce the number of variables during testing, the acceleration was held a 10 mm/s^2. This selection led to two issues during testing and analysis. First, since the acceleration was held constant while the velocity was varied, the distance the stage travelled before reaching the target velocity varied. This resulted in substrate still accelerating after the droplet broke away during some of the testing runs. This was compensated for during the analysis by adding the flow development regime to separate the effects of the increasing velocity from the steady-state data.

The second consequence of the acceleration selection was that for all of the testing runs the stage would not only be accelerating during the initial displacement of the cover slip before droplet breakaway, but that it would do so in an unsteady manner. While the control routine for the stage would meet the average acceleration target, the instantaneous acceleration could vary from run to run. During the analysis it was noted that the stiffness of the droplet would change as the acceleration rate changed. This is illustrated in Figure 27 at x = 0.1mm where the slope of the force/displacement line changes with the change in slope of the velocity/displacement line. Averaging the stiffness of the test runs was used to account for this.

Validation runs were conducted to see how the variable acceleration rates would affect the breakaway forces. From this testing, it was concluded that an acceleration rate high enough to reach the target velocity within the distance required to take up the fiber slack would have no effect upon the breakaway forces and would keep the stiffness more consistence during the initial droplet deformation. For further testing the maximum acceleration rate of the stage of 160 mm/s^2 should be used.

In addition to the acceleration errors, the control routine would consistently miss the target velocity, resulting in a larger velocity than desired. This error was accounted for by using the actual stage velocity versus the requested velocity in the calculations.

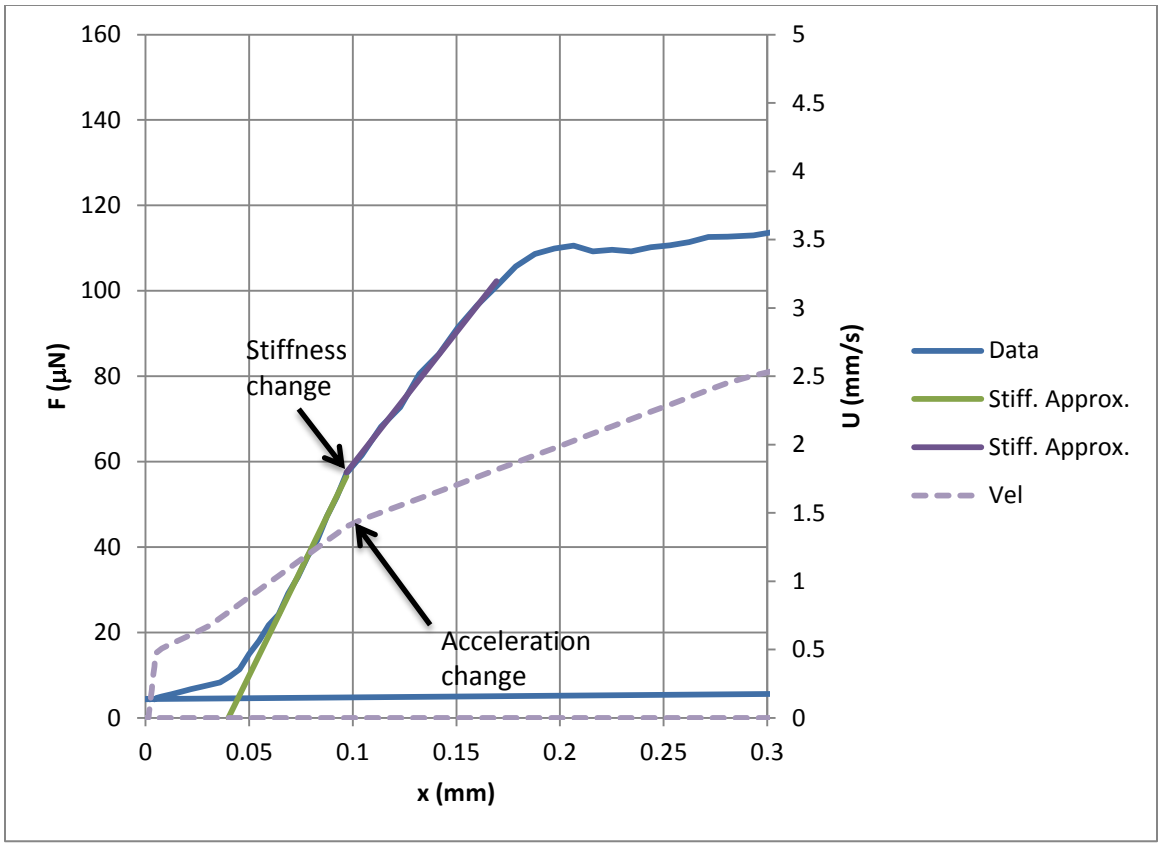

Figure 27: Stiffness versus acceleration rate for 9 x 9 x 1.25 mm^3 droplet with linear data approximations

Volume from Pipet

Since the droplet height was determined by the volume of the droplet, any error in the droplet volume is directly proportional to the error in the height. The volume of water dispensed from the pipet was checked by measuring the mass of the water dispensed versus the indicated volume. An Ohaus Adventurer SL AS214 digital scale accurate to 0.0001 g was used to measure the mass of the water. From Table 6 showing the testing results, the average volume error was within ±1%.

Table 6: Droplet volume error

∀	m	m_1	m_2	m_3	m_4	m_5	m_{avg}	σ	Error
μL	g	g	g	g	g	g	g	g	%
25	0.0250	0.0241	0.0248	0.0247	0.0253	0.0251	0.0248	0.0005	-0.60%
51	0.0509	0.0504	0.0506	0.0505	0.0505	0.0504	0.0505	0.0001	-0.82%
61	0.0609	0.0603	0.0604	0.0606	0.0610	0.0610	0.0607	0.0003	-0.36%
81	0.0808	0.0805	0.0803	0.0810	0.0799	0.0863	0.0816	0.0027	0.94%
91	0.0908	0.0906	0.0907	0.0917	0.0917	0.0919	0.0913	0.0006	0.55%
101	0.1008	0.1009	0.1022	0.1013	0.1022	0.1018	0.1017	0.0006	0.88%
122	0.1218	0.1215	0.1212	0.1215	0.1210	0.1204	0.1211	0.0005	-0.52%
152	0.1517	0.1507	0.1511	0.1512	0.1510	0.1520	0.1512	0.0005	-0.33%

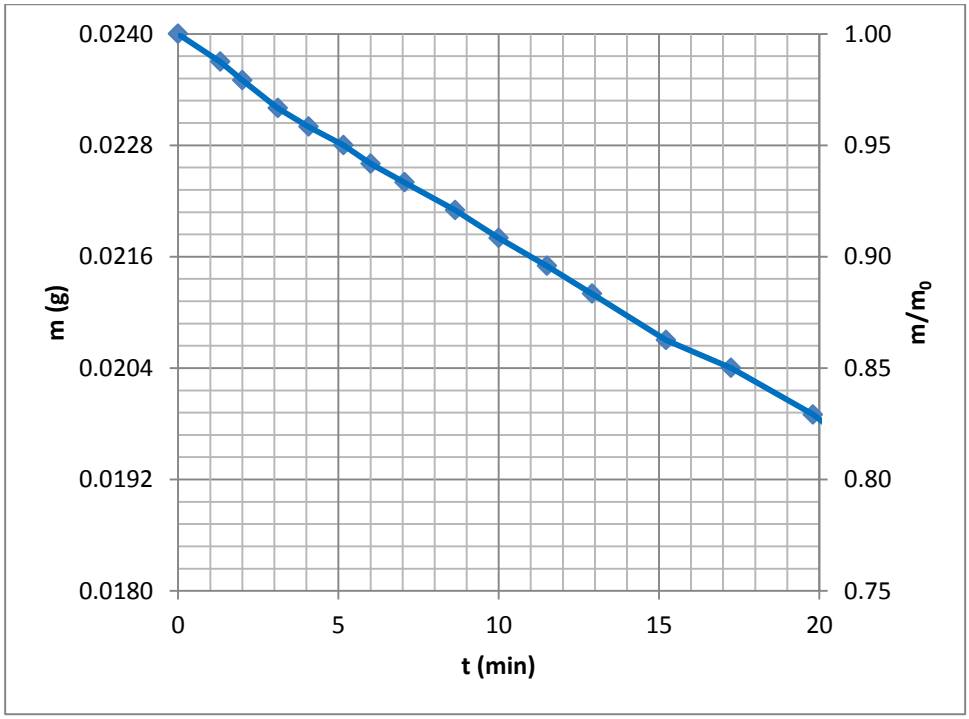

Figure 28: Mass versus time for 25 μL droplet under 4.5 x 4.5 mm^2 cover slip

Droplet Evaporation

As described in the testing routine, the same droplet was used over multiple runs. This led to the possibility of a change in the volume and therefore the geometry of the droplet due to evaporation. To determine the possible error, the evaporation rate of a 25 μL droplet under a 4.5 x 4.5 mm^2 cover slip was tested by measuring the mass versus time. This configuration was selected as it would be the worst case for the testing schedule due to the ratio of the droplet free

surface area to volume [34, 35, 36, 37]. Figure 28 shows the mass of the droplet for the first 20 minutes of testing. The typical time between runs was approximately 1 minute with 4 to 5 runs per droplet. From Figure 28, during the typical 5 minute period the droplet would be used, approximately 5% of its initial mass would be lost. As the stiffness is inversely proportional to the height, this would correspond to a 5% increase in the stiffness.

Cover Slip Stability

As previously mentioned, the stability of the cover slip/droplet system could have large effects upon the force data. Figure 29 shows one example of this case where the increase in the force can be seen. The main method to account for this phenomenon was to eliminate it as much as possible by careful placement of the cover slip on the droplet, insuring full wetting of the cover slip, and proper cover slip/fiber alignment. Additionally, as previously mentioned in the analysis section, if a large portion of the steady-state data was unaffected by stability issues, the unstable data was eliminated.

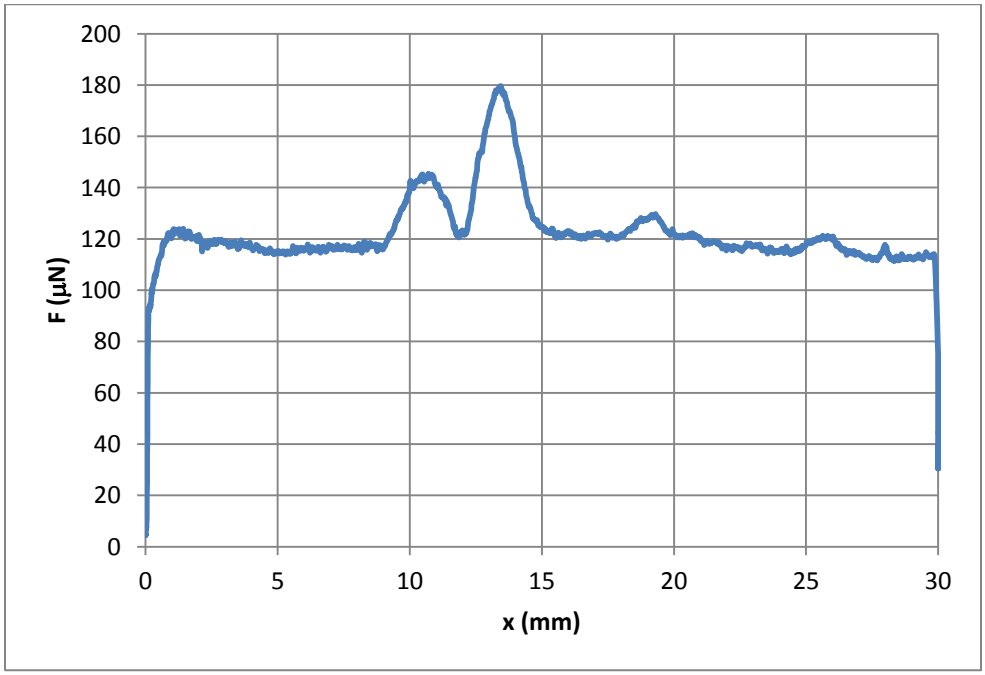

Figure 29: Force spike due to yaw instability for 9 x 9 x 0.75 mm^3 droplet. Also, shows onset at approximately one cover slip length and the return to the steady-state average after perturbation.

Alignment

Two types of alignment error were encountered during testing. The first was the misalignment of the fiber to the cover slip. This resulted in the advancing edge of the cover slip be skewed to the direction of the velocity, which effectively increased the advancing and receding contact lines by the length of the cover slip and therefore the dramatically increasing the force data. To help eliminated this type of error the procedure for attaching the fiber to the cover slip was changed to the method described above in the testing procedure section.

The second type of misalignment was of the initial position of the droplet/cover slip to the sensor such that the fiber would be at a slight angle to the direction of the stage velocity. This causes droplet to have velocity component in y-direction as it would come back into proper alignment with the sensor. Figure 30 shows a sample force/displacement plot for this kind of error (Note: data in Figure 30 is from test run before change in test procedure and is not part of the data set used in analysis). This alignment error resulted in a decreasing steady state force as droplet centered on sensor. This was fixed with by using a setup run to have droplet self-align itself with sensor.

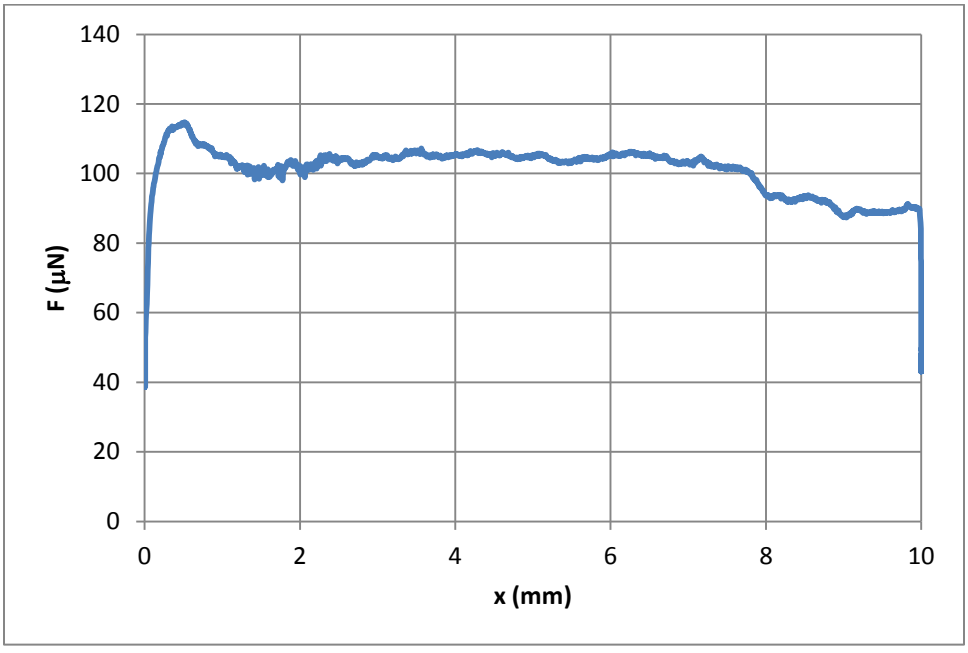

Figure 30: Cover slip alignment error with self-correction for 9 x 9 x 1.25 mm^3 droplet showing the characteristic decrease in force

Substrate Surface Properties

After testing was completed for each substrate the static contact angle was measured optically using the goniometer. Table 7 summarizes the results of the testing and analysis by the DropSnake program with the measured contact angle for each side of the test drop listed, the droplet average, and the average across all the test substrates.

Constant substrate properties between testing runs is a major underlying assumption in the analysis of the forces and the subsequent data correlation. From Table 7, deviation as much as 4.3° was seen from the group average. To what degree this deviation represents error in the substrate properties and the subsequent effects of the force is hard to predict as the mechanisms of the contact line motion are still not understood [9, 13] and deviations of up to 10° in the dynamic contact angle have been observed experimentally for the same system [13].

Table 7: Substrate static contact angles

Substrate #	θ_{left} deg	θ_{right} deg	θ_{avg} deg
5b	109.2	107.7	108.4
6b	109.9	108.3	109.1
7b	109.0	109.2	109.1
8b	109.5	109.1	109.3
9b	111.7	111.6	111.7
10b	112.3	111.5	111.9
11b	108.0	107.0	107.5
12b	111.0	110.6	110.8
13b	114.2	112.0	113.1
14b	108.7	107.9	108.3
15b	115.4	114.7	115.1
16b	112.0	111.8	111.9
17b	113.9	113.1	113.5
Average			110.7
σ			2.3

Fiber Stiffness

It was assumed during the calculation of the droplet stiffness that the glass fiber was rigid. The stiffness of the fiber can be calculated from the cross-sectional area, the length, and the Young's modulus of the glass by:

$$k_{fiber} = \frac{EA}{L} \tag{43}$$

The Young's modulus for E-glass fiber can vary between 72 to 85 GPa [38]. For the minimum estimated fiber diameter of 10 μm and Young's modulus of 72 GPa and a fiber length of 200 mm, the fiber stiffness is approximately 28,000 μN/mm. The measured stiffness is a function of the linear spring system of the droplet and fiber:

$$\frac{1}{k_{measured}} = \frac{1}{k_{fiber}} + \frac{1}{k_{droplet}} \tag{44}$$

For the maximum measured droplet stiffness of approximately 1500 μN/mm, which represents the worst case error scenario, the error due to the fiber stiffness acts to soften the droplet stiffness by approximately 5%.

Calculation Errors

Regression

Half of the data used in the correlation was for the 9 x 9 mm^2 plate geometry. This results in skewing the effects of the width on regression towards this geometry, most notably for the stiffness as seen in Figure 12. Also, as this was the only geometry for which the height was varied in the current testing, statistically meaningful correlation of the height to the force data is not possible.

Regime Selection

One of the greatest challenges in the analysis of the test data was selecting the dividing point for the regimes. The dividing point between the regimes was difficult to discern due to several causes. As noted previously, the local acceleration had an effect upon the slope of the force/displacement data. This caused problems determining where the slack in the fiber was fully taken up and when the contact lines began movement as the change in the slope was used to determine these points. Figure 27 shows an example where the sharp change in the force/displacement slope associated with droplet motion is softened by the increasing bulk velocity.

The sampling also caused difficulties in some cause. As noted previously in the analysis section, subdivisions of the regimes were used to help in fitting the data and accounting for the changes in acceleration. In some cases due to the sampling rate only two points of data would be used in a sub-regime. This would lead to local error in the fit of the data. However, as the system data was calculated over the total regime, the error was minimal. Also, improvements in the FT-S1000 sensor versus the older model FT-S540 allow for higher sampling rate without a decrease in resolution of the force voltage.

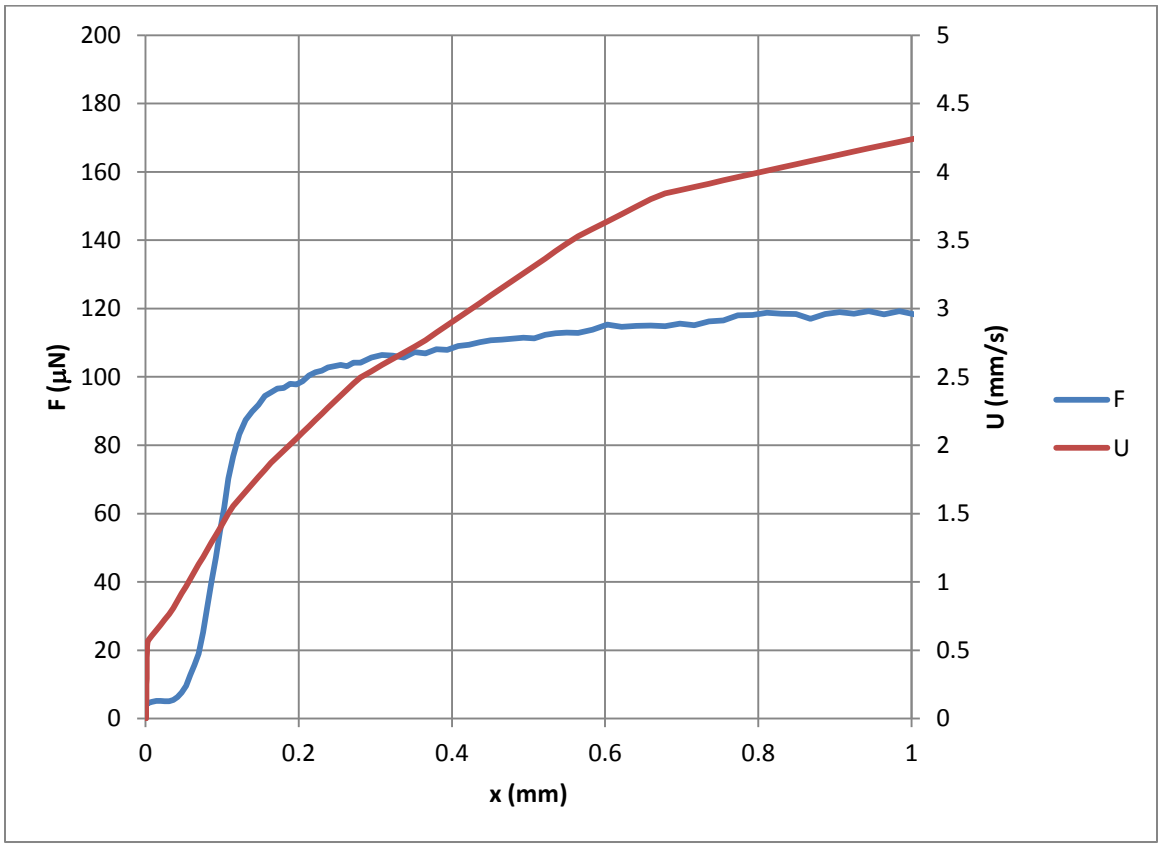

Figure 31: Regime selection error example for 9 x 9 x 0.75 mm^3 droplet showing smooth transition of force due to stage acceleration not typical of normal droplet breakaway.

FUTURE RESEARCH

During the testing and analysis phases to determine the static and dynamic components of droplet friction, several avenues for further research became apparent.

Height Variation

The biggest question that needs to be addresses is how the height affects the breakaway and dynamic forces as this phenomenon was not anticipated. Additional testing varying the height and width is needed to find the proper correlation. The lack of a factor proportional with the height in the hypothesized dynamic force equation resulted in the viscous term be dismissed by the data regression. Smaller gap heights should have a twofold effecting in determining the viscous force contribution as factor proportional to the height will be diminished and velocity gradient should increase amplifying the viscous loss.

Stability

Much of the testing routine and setup procedures were designed to avoid stability issues that were encountered in testing. The exact causes and triggers are not fully understood at this time. Further test could explore the geometry and velocity limits and relationship which are more likely to lead to stability issues such as the aspect ratio between the length and width and between the height and plate area. Also of interest would be how the plate mass affects the stability as this would be a key limitation for the use of this technology for part transportation or assembly.

As noted previously, the onset of both instabilities seen was usually in the area of one cover slip length displacement. It is possible that the droplet setting in one location could affect

the substrate properties, causing the instability modes as the contact lines become pinned at one cover slip length. How surface defects lead to instabilities would be another key area of interest.

Dynamic Modeling

While two simple models were proposed for the droplet stiffness and breakaway force, the dynamic force was only treated empirically. Several theories and model exist which address the contact line friction phenomenon and could be used to create a similar dynamic model [9]. Several challenges exist to this. There is not one unified model as of yet for the contact line friction and the competing theories often are based upon differing physical scales [9]. Additionally the apparent contact angle can sensitive to the velocity [9].

3-D Flow Modeling

Originally it was planned to create a simple 2-D analytical model of the flow to help determine the appropriate velocity gradients. However a simple analytical model for the flow is difficult to formulate due to the complex nature of the boundary conditions: velocity conditions at cover slip and substrate, free surfaces, slip condition at contact line [6]. 3-D model would help understand instabilities and where viscosity would play a role. Additionally, a flow model would help determine shape factors to correlate the force data with and help determine what role the height plays.

Different Cover Slip Geometries

With the role of the gap height playing an unexpected role in the breakaway and dynamic force, additional geometries are needed to correlate this effect in a meaningful way. Smaller heights and higher velocities are also needed to get into a range were viscosity would take effect and to determine where this effect will dominate the other height/force relationship. Additional cover slip geometries besides the rectangular geometry are also needed to determine how this data can be applied to all geometries. Of particular interest would be round cover slips as these would most closely mimic the geometry of other tests.

Surface and Fluid Property Affects

Throughout the testing the substrate, fluid, and ambient were held constant. However variations in the static contact angles of up to 4.3° were notice between substrates which could lead to significant error, as previously noted in the error section. It is assumed the force data scales directly with the system surface tensions and the resulting contact angle hysteresis. However this assumption should be tested by changing the substrate and fluid properties to verify this assumption and determine how variations in the properties affect the friction forces. To this end, the advancing and receding contact angles should be measured for each substrate tested to verify the consistency of the contact angle hysteresis.

Additionally better comparison to previous works could be facilitated by some system property changes. By use of a more viscous liquid the contribution of the viscous losses to be better represented. Also, the use of air as an ambient allowed for neglecting the effect of external drag on the droplet. Frequently oils are used as ambient in other systems and this assumption is not valid [1, 2].

Velocity Variation

The effect of droplet deceleration was not addressed in this study as inertial forces were deemed negligible and therefore the contact line friction force would dominate. While this may be true due to the low mass of the droplet, confirming that the contact line friction varies only with the velocity and not the acceleration would be of interest. Additionally, how the force varies when the droplet is brought to rest and then accelerated in another direction would be pertinent information for using droplets for positioning of parts.

Contact Line Relative Movement

When determining when the droplet motion began and in selecting the different sub-regimes, it was noted that there was a change in stiffness before the apparent droplet bulk motion. It was assumed that this phenomenon was due to the advancing and receding contact

lines not begin motion at the same time. The displacement and the force at which this occurred were recorded for further study and for the use of modeling this phenomenon.

While the current results capture the dominant effects upon the breakaway and steady-state dynamic forces due the contact line motion, error and uncertainty still exist that need to be addressed to fully comprehend the force components involved and provide more accurate models. The future research should be primarily focused on the effect of the height on the static and dynamic friction forces. Deriving a more robust model will allow for application of this data for a larger range of droplet sizes and allow for more accurate capture of the viscous effects.

REFERENCES

[1] V. Bahadur and S. V. Garimella, "An energy-based model for electrowetting-induced droplet actuation," *Journal of Micromechanics and Microengineering,* pp. 1494-1503, 2006.

[2] H. Ren, R. B. Fair, M. G. Pollack and E. J. Shaughnessy, "Dynamics of electro-wetting droplet transport," *Sensors and Actuartors B,* pp. 201-206, 2002.

[3] E. S. Baird and K. Mohseni, "A Unified Velocity Model for Digital Microfluidics," *Nanoscale and Microscale Thermophysical Engineering,* pp. 109-120, 2007.

[4] M. J. Schertzer, S. I. Gubarenko, R. Ben-Mrad and P. E. Sullivan, "An Empirically Validated Analytical Model of Droplet Dynamics in Electrowetting on Dielectric Devices," *Langmuir,* pp. 19230-19238, 2010.

[5] J. Berthier, Micro-drops and Digital Microfluidics, Waltham, MA: Elsevier Inc., 2013.

[6] A. Ahmadi, H. Najjaran, J. F. Holzman and M. Hoorfar, "Two-dimensional flow dynamics in digital microfluidic systems," *Journal of Micromechanical and Microengineering,* vol. 19, no. 6, 2009.

[7] J. Berthier, K. Brakke, F. Grossi, L. Sanchez and L. Di Cioccio, "Self-alignment of silicon chips on wafers: A capillary approach," *Journal of Applied Physics,* p. 108, 2010.

[8] V. Bahadur and S. V. Garimella, "Electrical actuation-induced droplet transport on smooth and superhydrophobic surfaces," *International Journal of Micro-Nano Scale Transport,* vol. 1, no. 1, 2010.

[9] T. D. Blake, "The physics of moving wetting lines," *Journal of Colloid and Interface Science,* 2006.

[10] H. B. Eral, D. J. C. M. 't Mannetje and J. M. Oh, "Contact angle hysteresis: a review of fundamentals and applications," *Colloid and Polymer Science,* no. 291, pp. 247-260, 2013.

[11] W. C. Nelson and C.-J. Kim, "Droplet Actuation by Electrowetting-on-Dielectric (EWOD): A Review," *Journal of Adhesion Science and Technology,* vol. 26, pp. 1747-1771, 2012.

[12] T. D. Blake and J. De Coninck, "The influence of solid-liquid interactions on dynamic wetting," *Advances in Colloid and Interface Science,* vol. 96, pp. 21-36, 2002.

[13] R. L. Panton, Incompressible Flow, Hoboken: John Wiley & Sons, Inc., 2005.

[14] H. B. Eral, D. J. C. M. Mannetje and J. M. Oh, "Contact angle hysteresis: a review of fundamentals and applications," *Colloid and Polymer Science,* vol. 291, pp. 247-260, 2013.

[15] N. Kumari, V. Bahadur and S. V. Garimella, "Electrical Actuation of Dielectric Droplets," *Journal of Micromechanical and Microengineering,* vol. 18, 2008.

[16] N. B. Crane, P. Mishra and A. A. Volinsky, "Characterization of electrowetting processes through force measurements," *Review of Scientific Instruments,* vol. 81, 2010.

[17] Q. Ni, T. Marschke, S. Steele, N. Seyed and N. B. Crane, "Studying of Contact Angle Friction and Contact Angle Hysteresis (CAH) Through Force Measurements," in *Proceeding of the ASME 2012 International Mechanical Engineering Congrees & Exposition*, Houston, 2012.

[18] S. K. Najafi, *Design of Contact Line Friction Measurement Machine Apparatus,* Tampa: University of South Florida, 2012.

[19] E. J. De Souza, M. Brinkmann, C. Mohrdieck, A. Crosby and E. Arzt, "Capillary Forces between Chemically Different Substrates," *Langmuir,* vol. 24, pp. 10161-10168, 2008.

[20] E. J. De Souza, L. Goa, T. J. McCarthy, E. Arzt and A. J. Crosby, "Effect of Contact Angle Hysteresis on the Measurement of Capillary Forces," *Langmuir,* vol. 24, pp. 1391-1396, 2008.

[21] H. Kusumaatmaja and R. Lipowsky, "Equilibrium Morphologies and Effective Spring Constants of Capillary Bridges," *Langmuir,* vol. 26, no. 24, pp. 18734-18741, 2010.

[22] S. Gao and Y. Zhou, "Self-alignment of micro-parts using capillary interactions: Unified modeling and misalignment analysis," *Microelectronics Reliability,* vol. 53, pp. 1137-1148, 20113.

[23] K. A. Brakke, "The Surface Evolver," *Experimental Mathematics,* vol. 1, pp. 141-165, 1992.

[24] J. M. Hyman, "Numerical Methods for Tracking Interfaces," *Physica,* pp. 396-407, 1984.

[25] S. R. Annapradgada, S. Dash, S. V. Garimella and J. Y. Murthy, "Dynamics of Droplet Motion under Electrowetting Actuation," *Langmuir,* vol. 27, pp. 8198-8204, 2011.

[26] A. Frohn and N. Roth, Dynamics of Droplets, New York: Springer-Verlag, 2000.

[27] nanoScience Instruments, *FT-S540 Force Sension Probe.* www.nanoscience.com

[28] nanoScience Instruments, *FT-S1000 Microforce Sensing Probe.* www.nanoscience.com

[29] IDS Imaging Development Systems Gmbh, "IDS: It's so easy!," IDS Imaging Development Systems Gmbh, [Online]. Available: http://en.ids-imaging.com/manuals-ueye.html. [Accessed 13 October 2013].

[30] ImageJ, "ImageJ: Image Processing and Analysis in Java," [Online]. Available: http://rsbweb.nih.gov/ij/. [Accessed 13 October 2013].

[31] Ecole Polytechnique Federale De Lausanne, "Biomedical Imaging Group: Download Algorithms," [Online]. Available: http://bigwww.epfl.ch/demo/dropanalysis/. [Accessed 13 10 2013].

[32] M. J. Schertzer, S. I. Gubarenko, R. Ben-Mrad and P. E. Sullivan, "An Empirically Validated Anayltical Model of Droplet Dynamics in Electrowetting on Dielectric Devices," *Langmuir,* vol. 26, no. 24, pp. 19230-19238, 2010.

[33] E. J. Routh, A Treatise on Analytical Statics, Cambridge: University Press, 1891.

[34] K. S. Birdi, D. T. Vu and A. Winter, "A Study of the Evaporation Rates of Small Water Drops Placed on a Solid Surface," *Journal of Physical Chemistry,* vol. 93, pp. 3702-3703, 1989.

[35] S. Tonini and G. E. Cossali, "An analytical model of liquid drop evaporation in gaseous environment," *International Journal of Thermal Science,* vol. 57, pp. 45-53, 2012.

[36] H. Y. Erbil, "Evaporation of pure liquid sessile and spherical suspended drops: A review," *Advances in Colloid and Interface Science,* vol. 170, pp. 67-86, 2012.

[37] J. C. Kent, "Quasi-Steady Diffusion-Controlled Droplet Evaporation and Condensation," *Applied Science Research,* pp. 315-360, 1973.

[38] www.azom.com, "E-Glass Fibre," [Online]. Available: http://www.azom.com/properties.aspx?ArticleID=764. [Accessed 13 11 2013].

APPENDICES

Nomenclature

English Symbols

Symbol	Definition	Units
a	Acceleration	mm/s^2
A	Area	mm^2
C	Constant	-
D	Diameter	mm
d	Distance	mm
F	Force	µN
f	Force per unit length	µN/mm
g	Gravity	m/s^2
h	Gap height	mm
k	Stiffness	µN/mm
l	Cover slip length	mm
m	Mass	mg
r	Radius	mm
Re	Reynolds number	-
t	Time	s
U	Bulk velocity	mm/s
u	Local velocity	mm/s
V	Volume	µL
We	Weber number	-
w	Cover slip width	mm

Greek Symbols

Symbol	Definition	Units
μ	Dynamic viscosity	Pa*s
ρ	Density of water	kg/m^3
σ	Standard deviation	-
γ	Surface tension	N*mm

Subscripts

Symbol	Definition
a	Advancing
break	Breakaway force
CA	Contact angle
CL	Contact line friction
dyn	Dynamic
fl	Fluid
hys	Contact angle hysteresis
r	Receding
s	Side
st	Static
sur	Surface
T	Total
vis	Viscous friction

Test Data

Data summary for testing divided in test groups of constant height, width, length, and velocity. Tables list the breakaway, steady-state dynamic, and maximum recorded force for each run with the group average and standard deviation. The droplet stiffness and linear regression fit is also provided. Plots of the force versus stage displacement are shown which illustrate the dynamics seen in testing; notably instability onsets and flow development after droplet breakaway.

TEST 1

Run	-	avg	std	a	b	c	d	e
h	mm	0.75	0.00	0.75	0.75	0.75	0.75	0.75
w	mm	9.00	9.00	9.00	9.00	9.00	9.00	9.00
l	mm	9.00	9.00	9.00	9.00	9.00	9.00	9.00
U	mm/s	1.079	0.002	1.082	1.078	1.078	1.077	1.082
F_{break}	μN	86.3	8.3	86.3	82.0	82.0	80.6	100.7
F_{dyn}	μN	93.7	2.7	94.6	91.2	96.4	90.5	95.9
F_{max}	μN	102.6	6.1	100.9	97.0	111.4	97.7	106.0
k	μN/mm	1455	58	1548	1449	1463	1406	1409
r	-	0.997	0.004	0.999	0.998	0.998	0.998	0.990

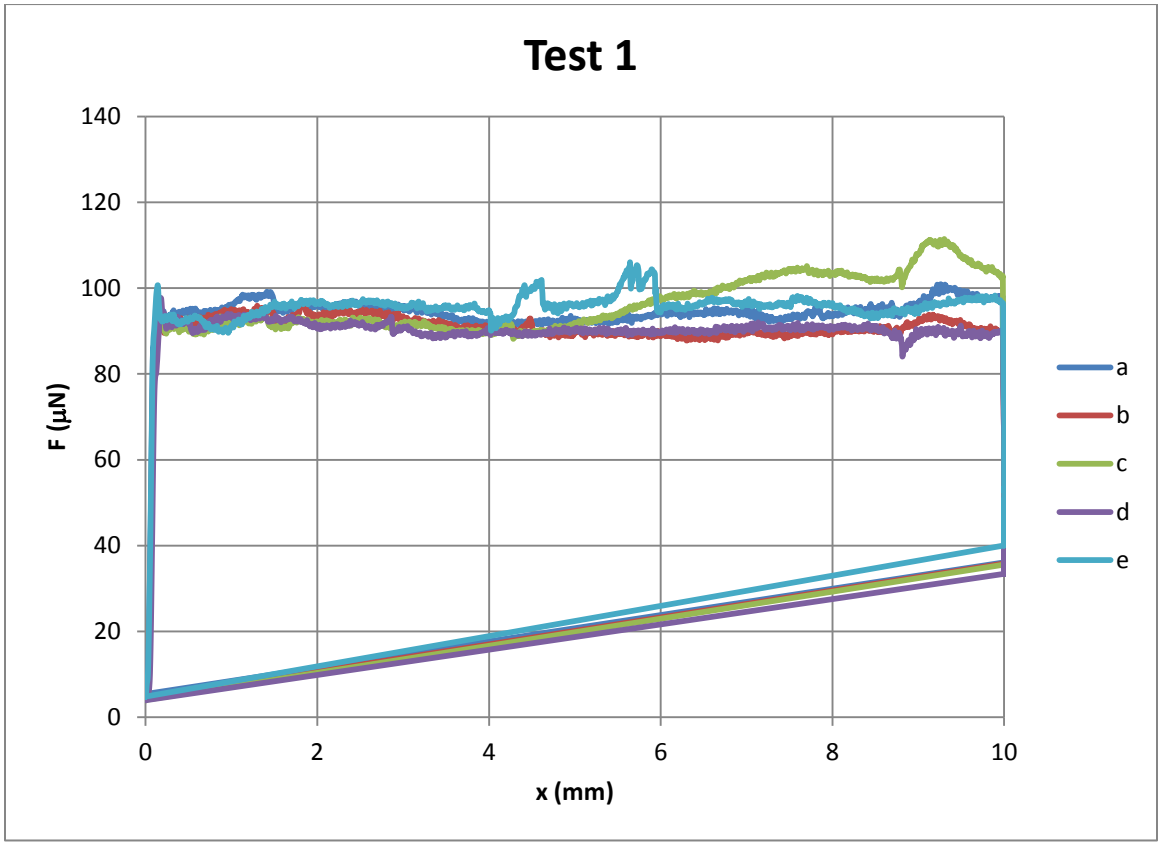

TEST 2

Run	-	avg	std	a	b	c	d	e	f
h	mm	0.75	0.00	0.75	0.75	0.75	0.75	0.75	0.75
w	mm	9.00	9.00	9.00	9.00	9.00	9.00	9.00	9.00
l	mm	9.00	9.00	9.00	9.00	9.00	9.00	9.00	9.00
U	mm/s	2.16	0.00	2.16	2.16	2.16	2.16	2.16	2.158
F_{break}	μN	98.05	2.67	96.33	95.51	102.15	99.45	95.61	99.3
F_{dyn}	μN	101.81	1.40	100.48	99.81	102.48	102.85	103.38	101.8
F_{max}	μN	117.49	10.03	129.03	104.99	125.39	113.21	108.13	124.2
k	μN/mm	1263.41	205.41	1541.75	1394.03	1230.20	943.16	1160.71	1311
r	-	0.99	0.01	1.00	1.00	0.97	1.00	0.98	0.988

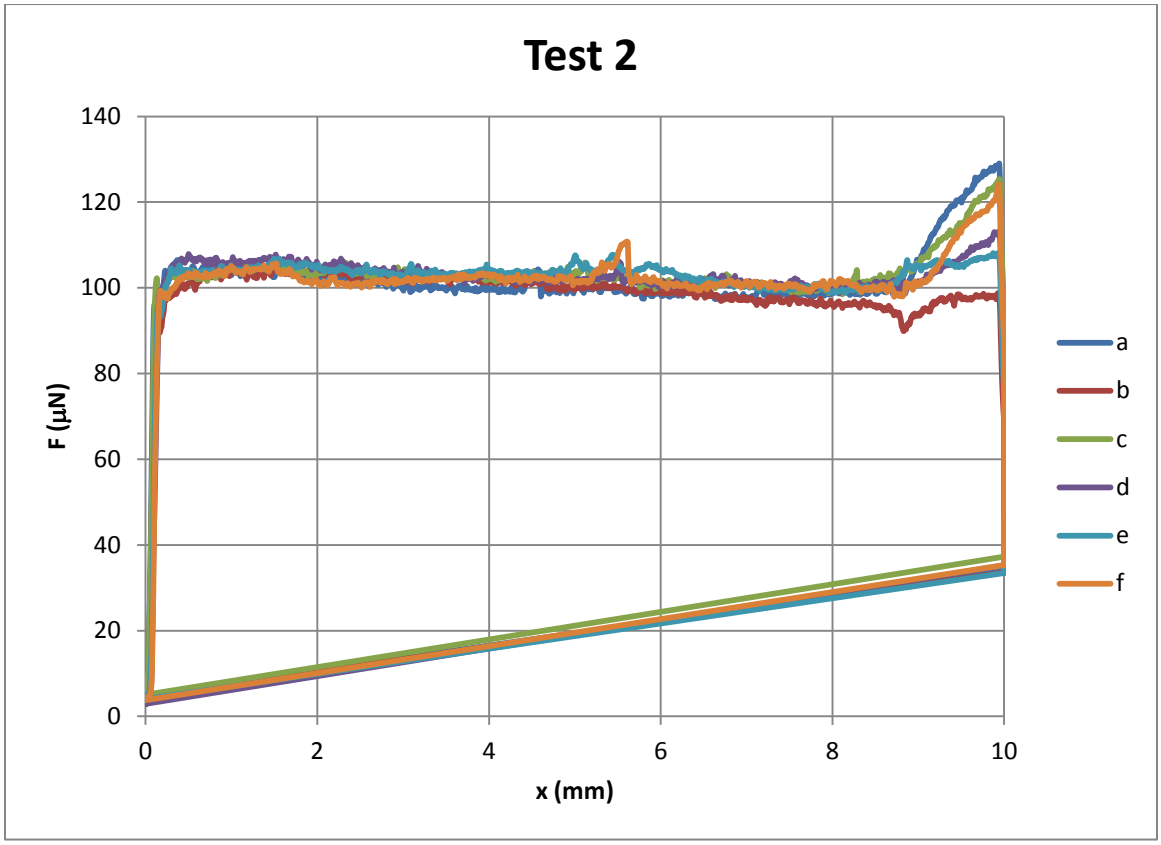

TEST 3

Run	-	avg	std	a	b	c	d	e	f
h	mm	0.75	0.00	0.75	0.75	0.75	0.75	0.75	0.75
w	mm	9.00	9.00	9.00	9.00	9.00	9.00	9.00	9.00
l	mm	9.00	9.00	9.00	9.00	9.00	9.00	9.00	9.00
U	mm/s	4.32	0.00	4.33	4.31	4.32	4.31	4.31	4.317
F_{break}	μN	93.93	1.66	92.58	96.64	94.42	94.30	93.77	91.9
F_{dyn}	μN	118.46	1.00	120.10	118.90	118.19	117.55	118.63	117.4
F_{max}	μN	160.10	17.30	144.37	147.34	173.26	174.22	141.81	179.6
k	μN/mm	1273.86	114.01	1429.22	1181.52	1171.72	1397.11	1271.59	1192
r	-	0.98	0.02	1.00	0.99	0.98	1.00	0.99	0.938

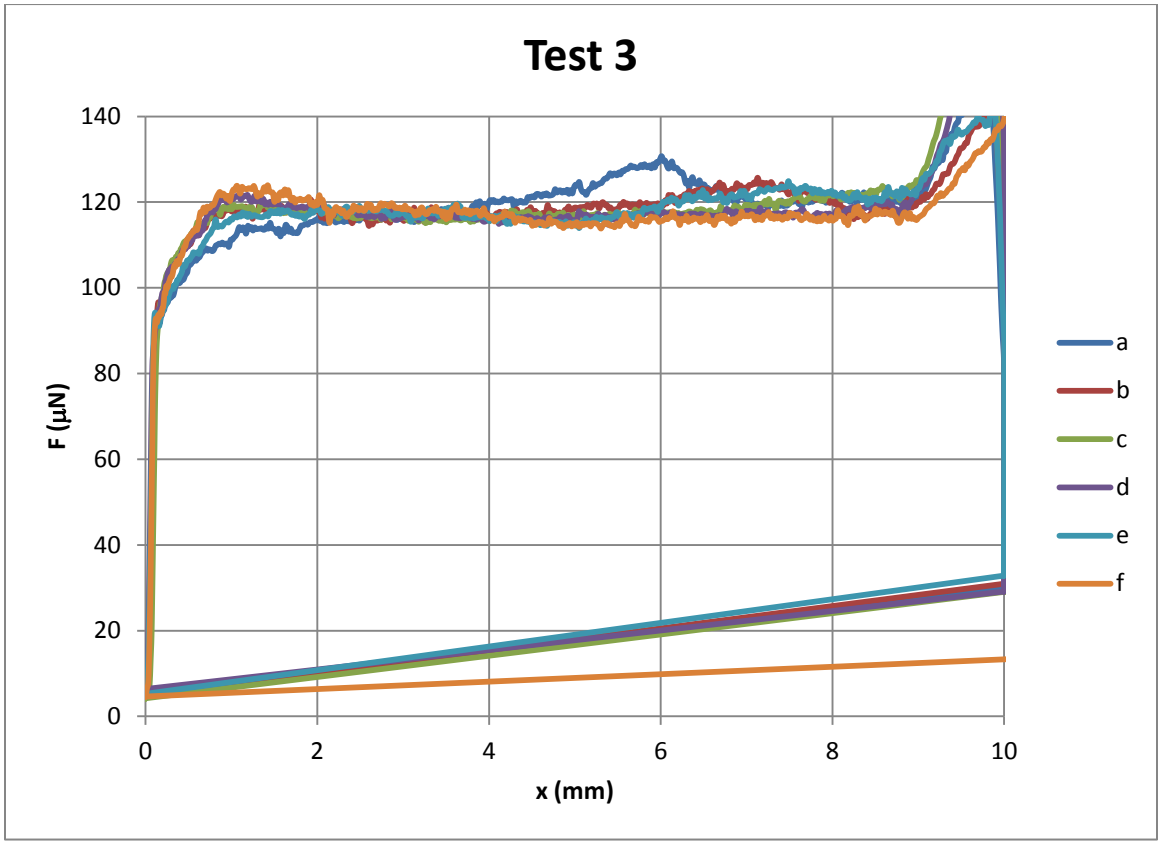

TEST 4

Run	-	avg	std	a	b	c	d	e
h	mm	1.00	0.00	1.00	1.00	1.00	1.00	1.00
w	mm	9.00	9.00	9.00	9.00	9.00	9.00	9.00
l	mm	9.00	9.00	9.00	9.00	9.00	9.00	9.00
U	mm/s	1.077	0.001	1.076	1.077	1.078	1.077	1.076
F_{break}	μN	105.2	3.4	103.6	101.2	104.3	109.8	107.4
F_{dyn}	μN	99.0	2.6	100.4	97.7	95.8	102.4	98.7
F_{max}	μN	106.2	3.1	107.7	101.8	104.3	109.8	107.4
k	μN/mm	1063	81	1056	1092	1105	1135	926
r	-	0.993	0.005	0.995	0.995	0.994	0.998	0.986

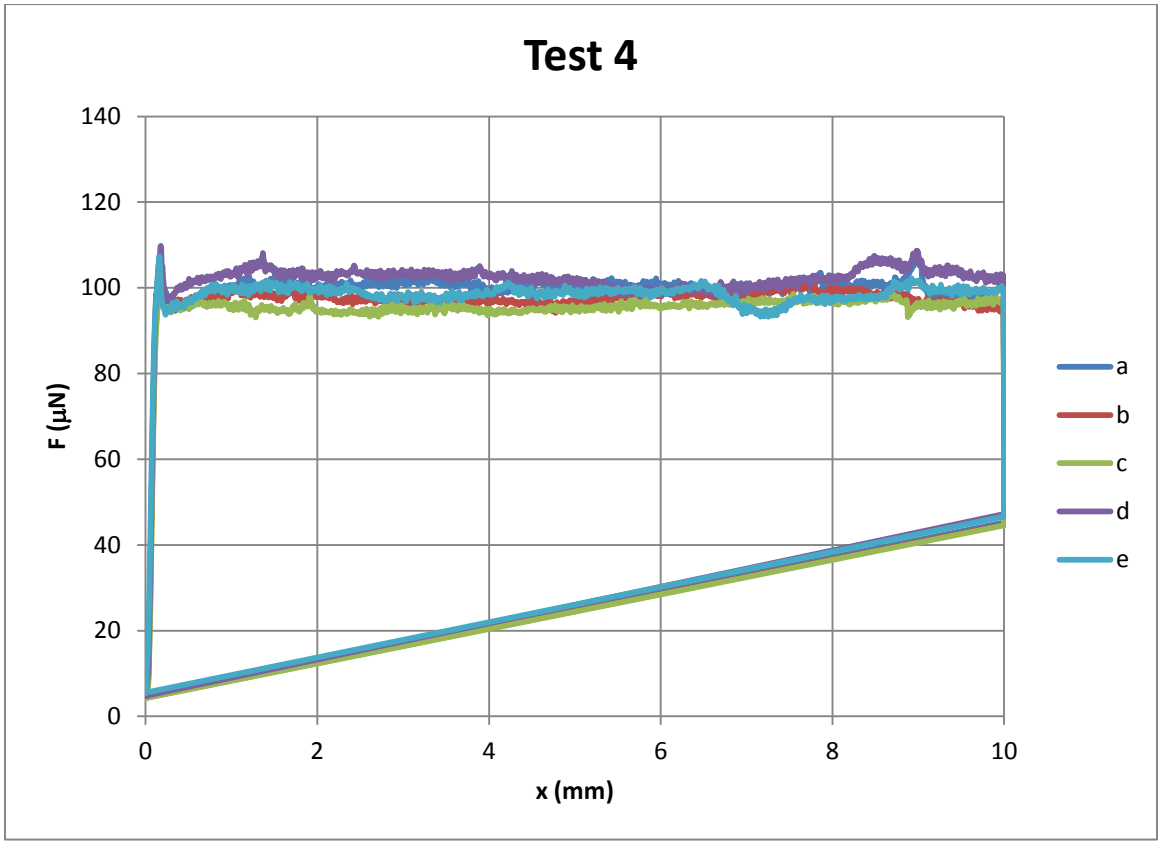

TEST 5

Run	-	avg	std	a	b	c	d	e
h	mm	1.00	0.00	1.00	1.00	1.00	1.00	1.00
w	mm	9.00	9.00	9.00	9.00	9.00	9.00	9.00
l	mm	9.00	9.00	9.00	9.00	9.00	9.00	9.00
U	mm/s	2.160	0.001	2.159	2.161	2.158	2.160	2.161
F_{break}	μN	110.4	5.8	115.0	111.9	108.7	101.1	115.1
F_{dyn}	μN	114.2	1.1	113.4	115.4	115.4	113.0	114.0
F_{max}	μN	126.8	6.0	117.8	130.0	123.6	130.4	132.4
k	μN/mm	929	152	824	714	1008	1053	1046
r	-	0.960	0.026	0.952	0.920	0.969	0.975	0.987

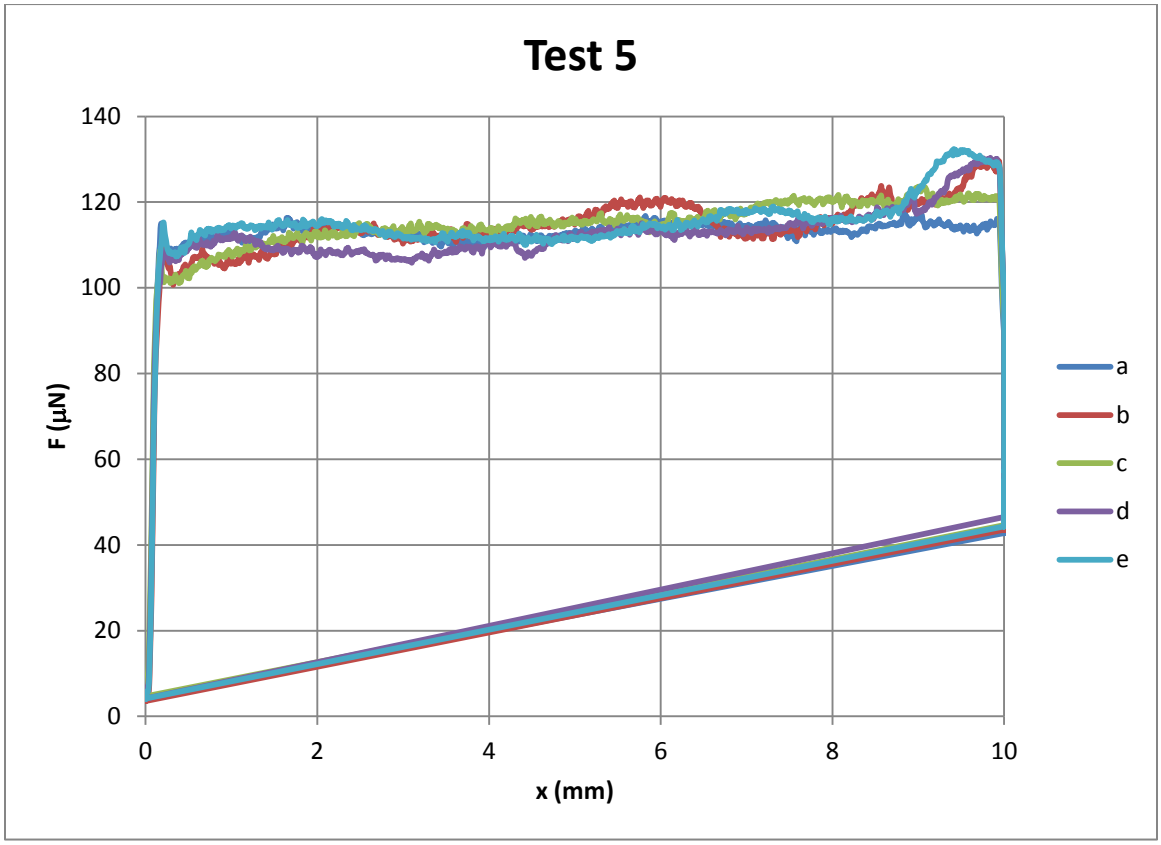

TEST 6

Run	-	avg	std	a	b	c	d	e
h	mm	1.00	0.00	1.00	1.00	1.00	1.00	1.00
w	mm	9.00	9.00	9.00	9.00	9.00	9.00	9.00
l	mm	9.00	9.00	9.00	9.00	9.00	9.00	9.00
U	mm/s	4.316	0.001	4.314	4.317	4.317	4.315	4.317
F_{break}	μN	107.0	3.5	110.7	107.7	101.5	108.7	106.4
F_{dyn}	μN	124.9	4.2	131.8	125.7	123.8	121.8	121.4
F_{max}	μN	145.6	33.3	204.9	136.7	128.4	128.5	129.7
k	μN/mm	950	108	894	986	1125	872	873
r	-	0.992	0.006	0.996	0.996	0.996	0.982	0.993

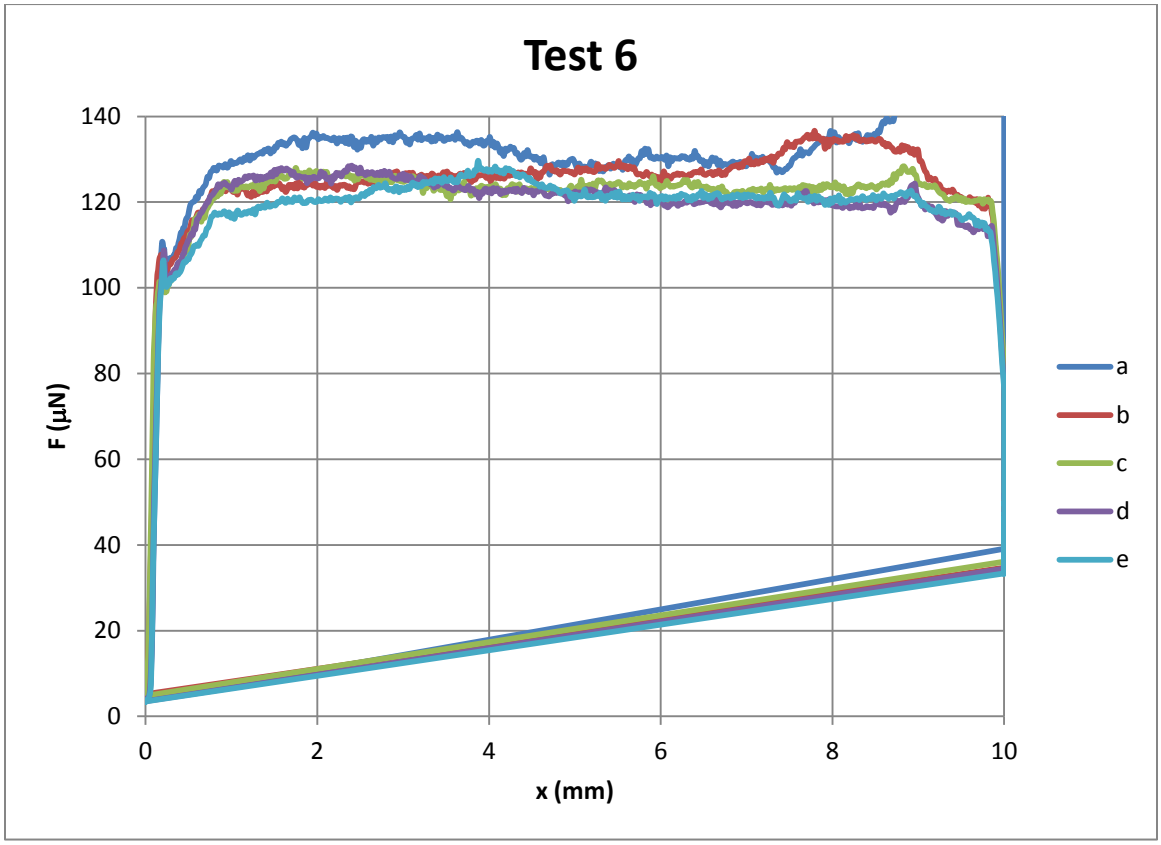

TEST 7

Run	-	avg	std	a	b	c	d	e	f
h	mm	1.25	0.00	1.25	1.25	1.25	1.25	1.25	1.25
w	mm	9.00	0.00	9.00	9.00	9.00	9.00	9.00	9.00
l	mm	9.00	0.00	9.00	9.00	9.00	9.00	9.00	9.00
U	mm/s	1.08	0.00	1.08	1.08	1.08	1.08	1.07	1.076
F_{break}	μN	102.08	1.54	104.30	102.24	103.95	100.79	101.23	99.9
F_{dyn}	μN	97.28	1.14	99.15	97.74	96.15	95.52	98.30	96.8
F_{max}	μN	103.42	2.57	104.30	102.24	103.95	100.79	107.37	101.9
k	μN/mm	798.38	45.49	707.79	877.24	749.70	822.74	822.95	810
r	-	1.00	0.00	0.99	1.00	0.99	1.00	1.00	0.996

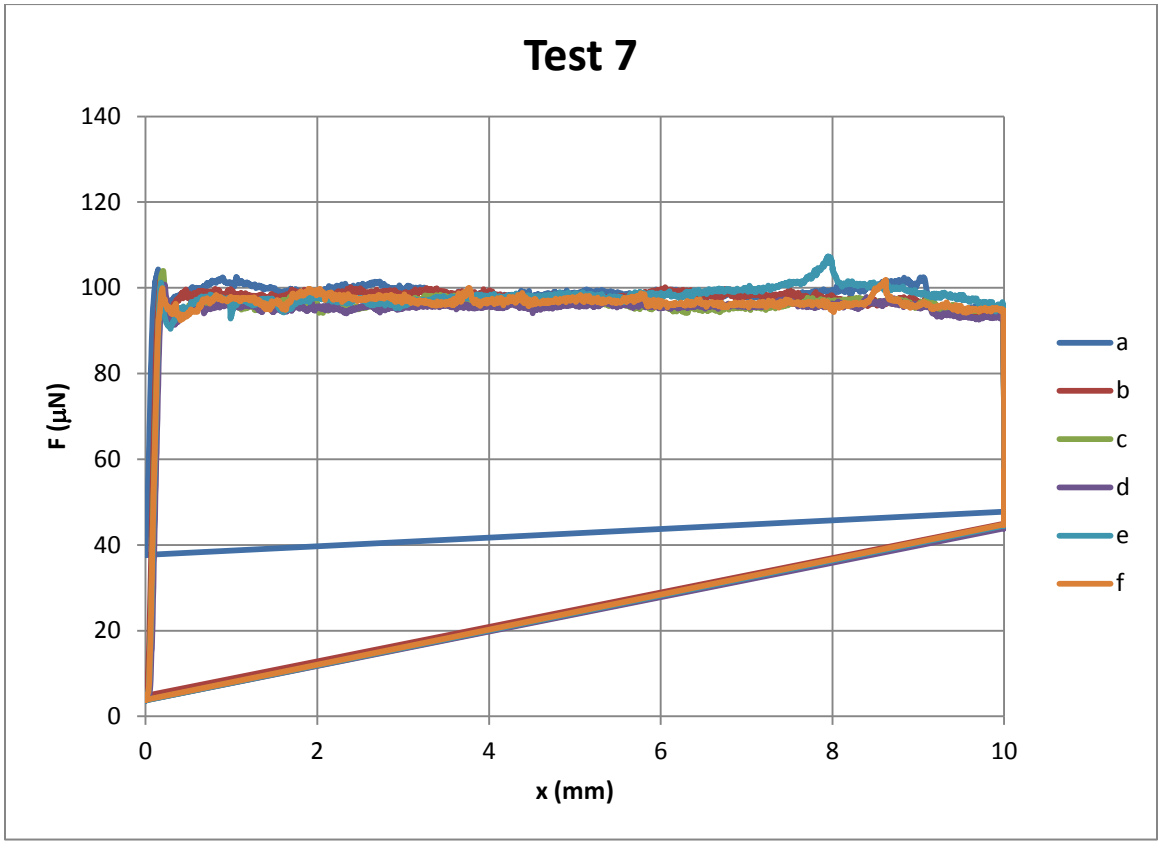

TEST 8

Run	-	avg	std	a	b	c	d	e
h	mm	1.25	0.00	1.25	1.25	1.25	1.25	1.25
w	mm	9.00	0.00	9.00	9.00	9.00	9.00	9.00
l	mm	9.00	0.00	9.00	9.00	9.00	9.00	9.00
U	mm/s	2.161	0.001	2.161	2.161	2.161	2.162	2.161
F_{break}	μN	117.0	2.2	119.2	113.6	116.6	118.4	117.4
F_{dyn}	μN	117.8	1.4	118.1	116.4	119.4	118.7	116.2
F_{max}	μN	126.1	4.5	124.5	131.9	122.9	129.7	121.5
k	μN/mm	728	65	665	716	691	733	835
r	-	0.995	0.003	0.997	0.994	0.990	0.994	0.998

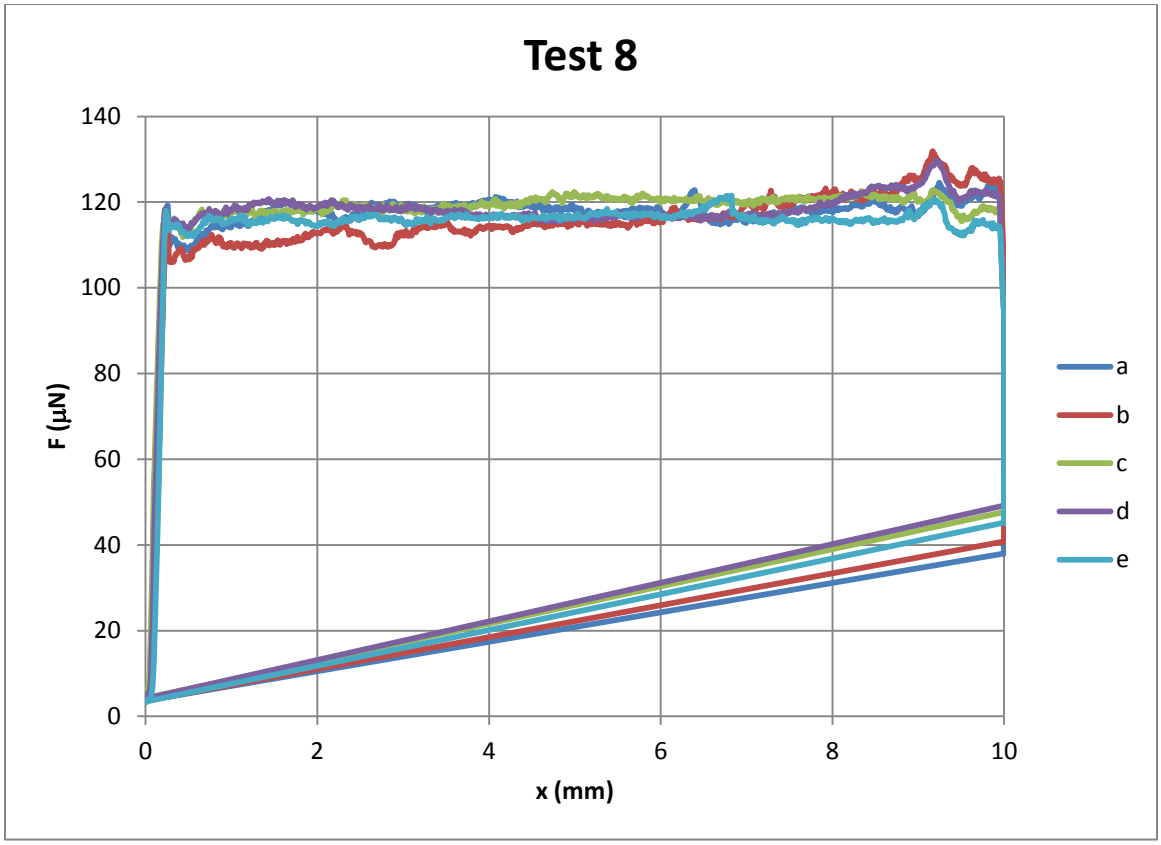

TEST 9

Run	-	avg	std	a	b	c	d	e
h	mm	1.25	0.00	1.25	1.25	1.25	1.25	1.25
w	mm	9.00	0.00	9.00	9.00	9.00	9.00	9.00
l	mm	9.00	0.00	9.00	9.00	9.00	9.00	9.00
U	mm/s	4.319	0.002	4.322	4.318	4.319	4.319	4.310
F_{break}	µN	110.2	3.8	116.3	110.6	112.0	109.7	99.4
F_{dyn}	µN	126.9	2.4	128.8	129.1	127.4	125.3	124.0
F_{max}	µN	157.3	45.8	134.5	136.5	167.2	132.5	128.0
k	µN/mm	702	36	691	730	669	754	660
r	-	0.992	0.007	0.981	0.987	0.995	0.999	0.994

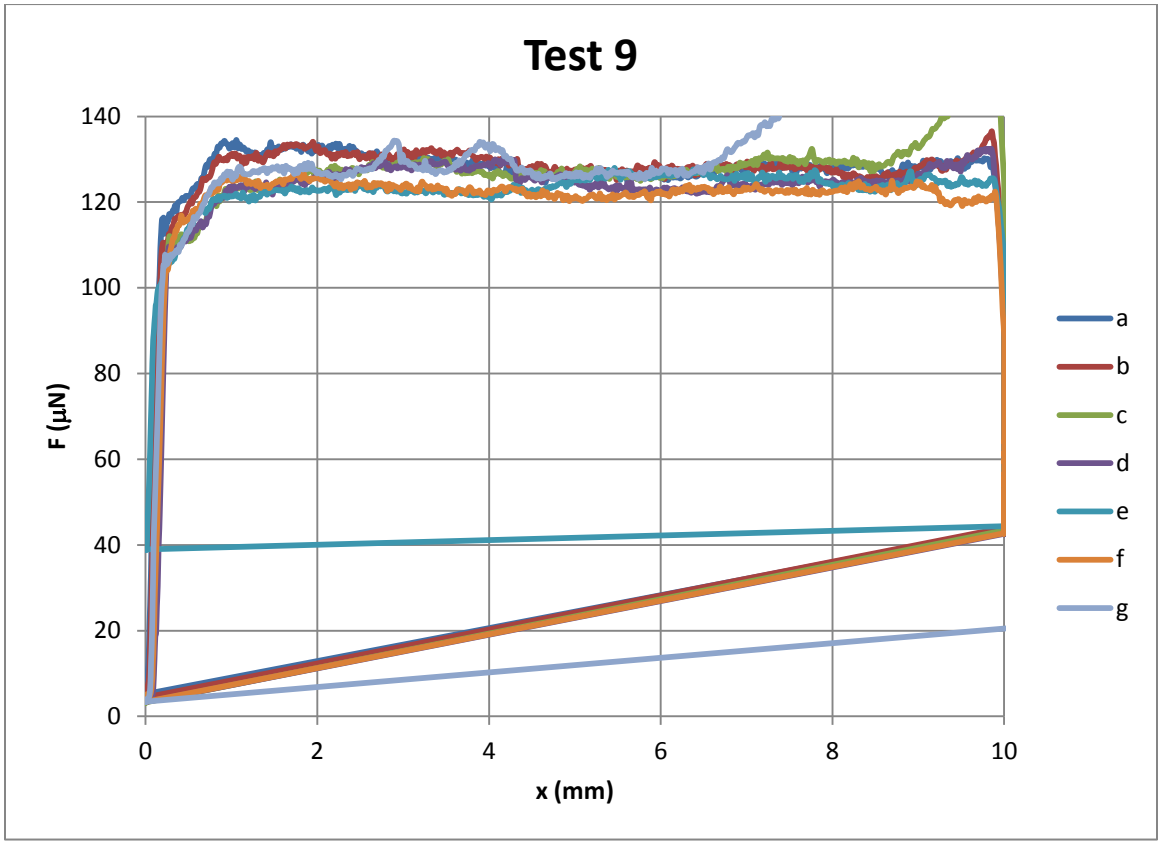

TEST 19

Run	-	avg	std	a	b	c	d	e
h	mm	1.25	0.00	1.25	1.25	1.25	1.25	1.25
w	mm	9.00	0.00	4.50	4.50	4.50	4.50	4.50
l	mm	9.00	0.00	9.00	9.00	9.00	9.00	9.00
U	mm/s	1.078	0.001	1.077	1.078	1.077	1.078	1.077
F_{break}	μN	63.4	4.6	61.5	68.4	60.9	56.5	66.6
F_{dyn}	μN	56.9	4.5	56.1	53.9	52.9	53.5	63.1
F_{max}	μN	66.3	5.2	68.5	68.4	63.1	57.4	70.8
k	μN/mm	432	40	466	407	405	390	493
r	-	0.999	0.001	0.997	0.998	0.999	0.999	0.999

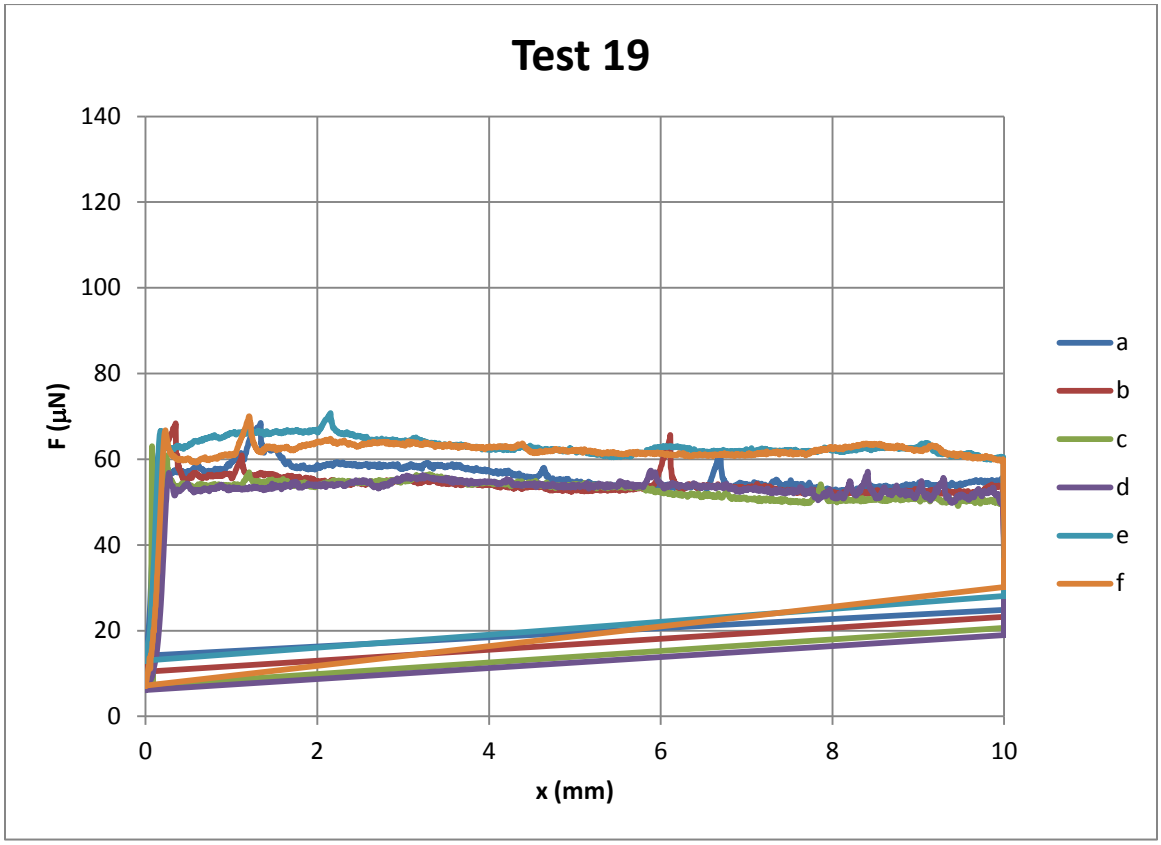

TEST 20

Run	-	avg	std	a	b	c	d	e
h	mm	1.25	0.00	1.25	1.25	1.25	1.25	1.25
w	mm	4.50	0.00	4.50	4.50	4.50	4.50	4.50
l	mm	9.00	0.00	9.00	9.00	9.00	9.00	9.00
U	mm/s	2.159	0.001	2.161	2.158	2.159	2.161	2.157
F_{break}	μN	68.4	4.5	76.8	65.2	68.3	69.4	65.2
F_{dyn}	μN	67.3	1.1	68.7	66.8	67.9	67.4	67.4
F_{max}	μN	76.6	7.2	76.8	71.8	89.4	79.5	72.8
k	μN/mm	413	72	434	348	406	376	366
r	-	0.986	0.011	0.999	0.978	0.976	0.973	0.992

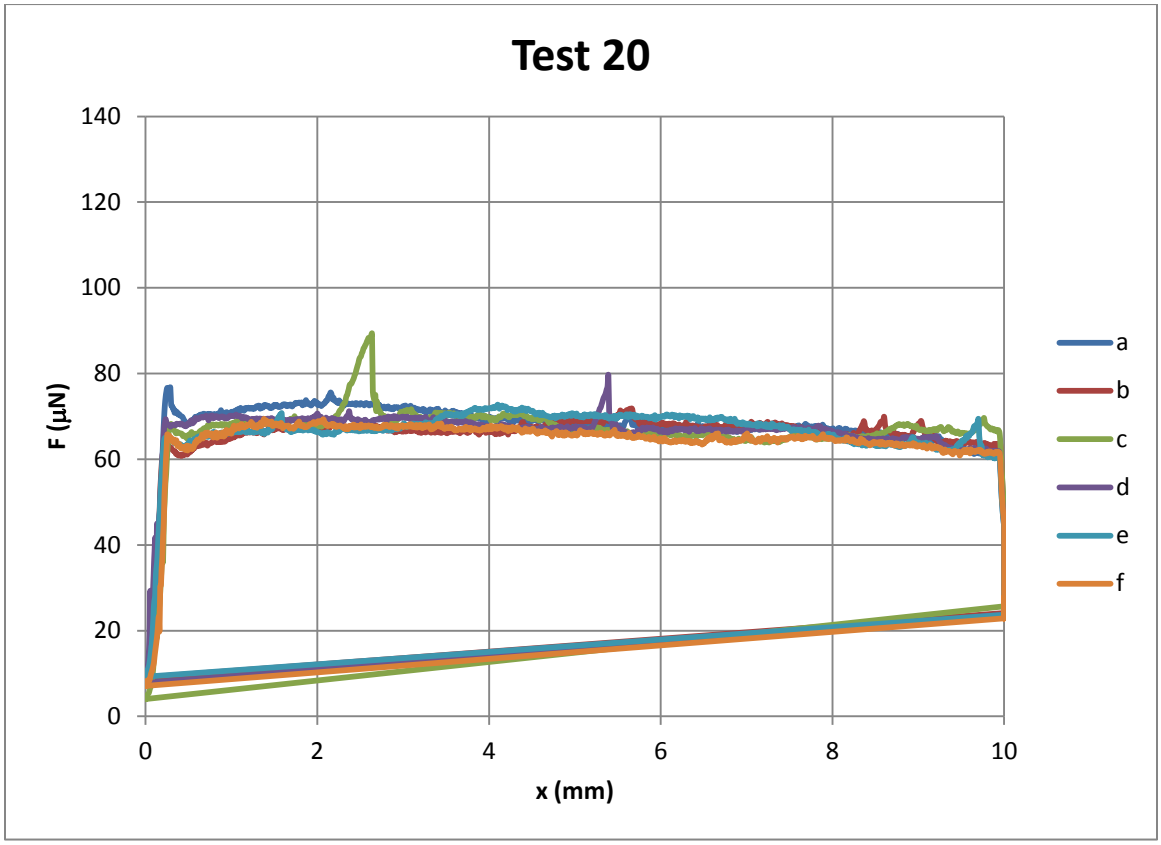

TEST 21

Run	-	avg	std	a	b	c	d	e
h	mm	1.25	0.00	1.25	1.25	1.25	1.25	1.25
w	mm	4.50	0.00	4.50	4.50	4.50	4.50	4.50
l	mm	9.00	0.00	9.00	9.00	9.00	9.00	9.00
U	mm/s	4.316	0.003	4.312	4.319	4.316	4.320	4.316
F_{break}	μN	68.6	3.0	65.2	66.2	69.0	70.8	73.3
F_{dyn}	μN	78.2	2.5	76.1	77.1	78.1	75.4	81.9
F_{max}	μN	84.2	4.1	80.9	84.1	83.1	80.7	91.8
k	μN/mm	449	48	402	398	517	455	432
r	-	0.999	0.001	0.999	0.999	1.000	0.998	0.999

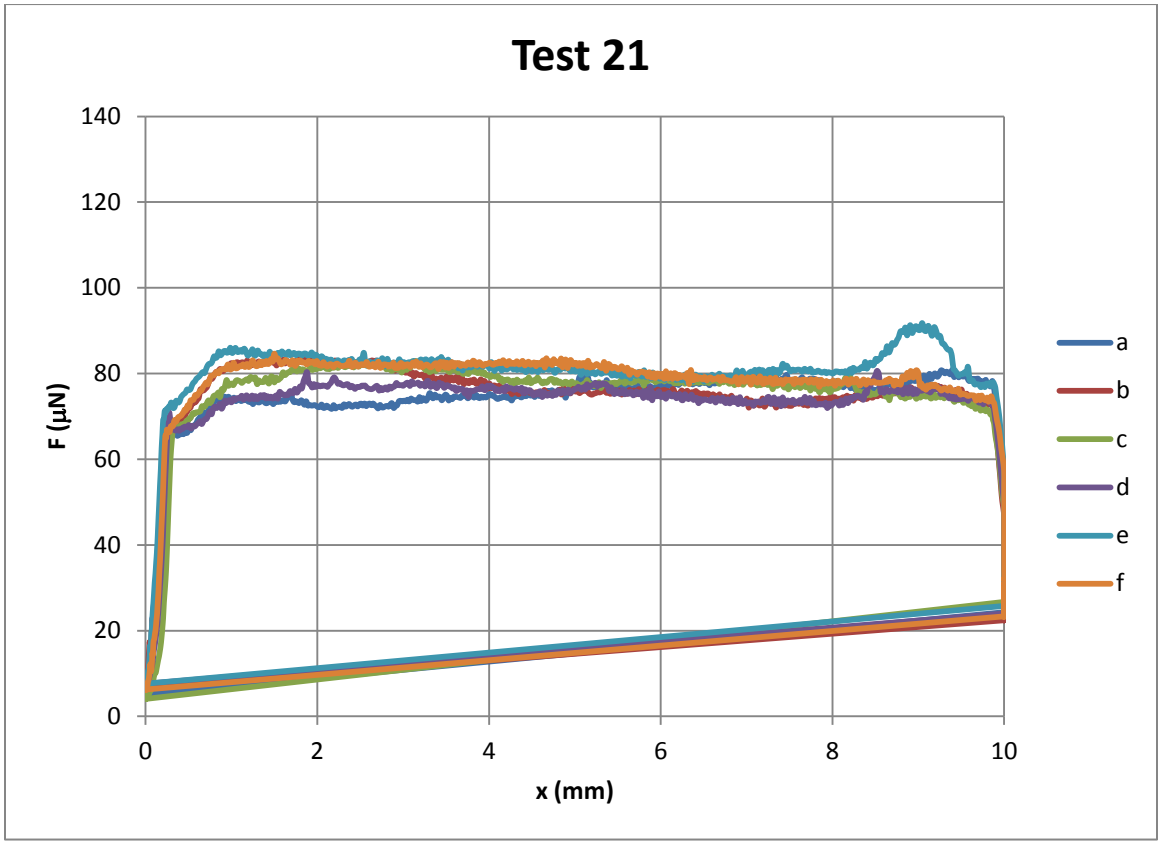

TEST 22

Run	-	avg	std	a	b	c	d	e
h	mm	1.25	0.00	1.25	1.25	1.25	1.25	1.25
w	mm	9.00	0.00	9.00	9.00	9.00	9.00	9.00
l	mm	4.50	0.00	4.50	4.50	4.50	4.50	4.50
U	mm/s	1.077	0.001	1.077	1.077	1.077	1.078	1.077
F_{break}	µN	114.7	1.8	117.3	115.6	113.9	114.1	115.3
F_{dyn}	µN	107.1	4.9	115.9	108.9	104.7	102.4	106.5
F_{max}	µN	116.9	5.0	126.1	118.4	113.9	114.3	117.0
k	µN/mm	736	33	743	730	740	794	703
r	-	0.998	0.001	0.999	0.997	0.998	0.999	0.999

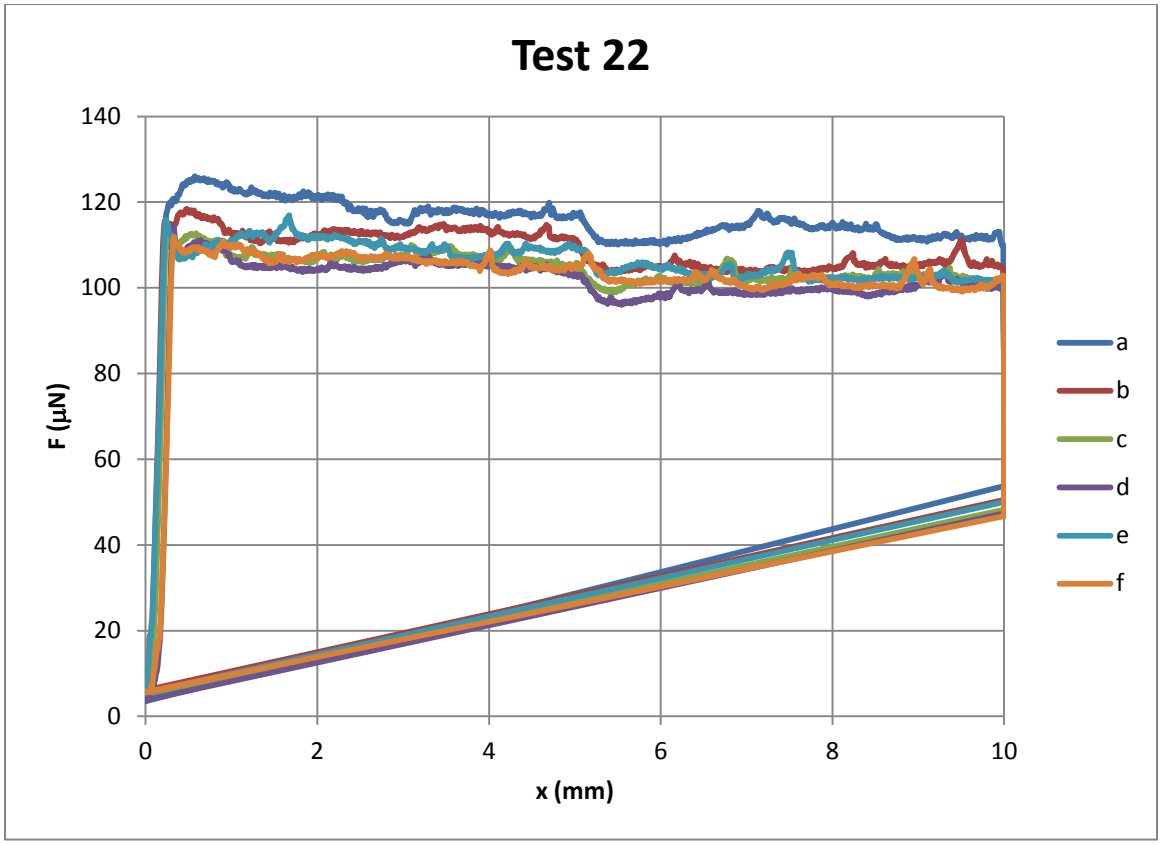

TEST 23

Run	-	avg	std	a	b	c	d	e
h	mm	1.25	0.00	1.25	1.25	1.25	1.25	1.25
w	mm	9.00	0.00	9.00	9.00	9.00	9.00	9.00
l	mm	4.50	0.00	4.50	4.50	4.50	4.50	4.50
U	mm/s	2.159	0.002	2.158	2.157	2.158	2.162	2.162
F_{break}	μN	118.5	2.2	120.8	120.9	115.1	117.4	118.3
F_{dyn}	μN	120.6	1.3	120.7	118.2	121.9	121.5	121.1
F_{max}	μN	129.8	2.5	130.8	125.6	131.2	132.9	129.4
k	μN/mm	714	89	843	699	579	670	735
r	-	0.993	0.011	0.999	0.995	0.972	0.997	0.999

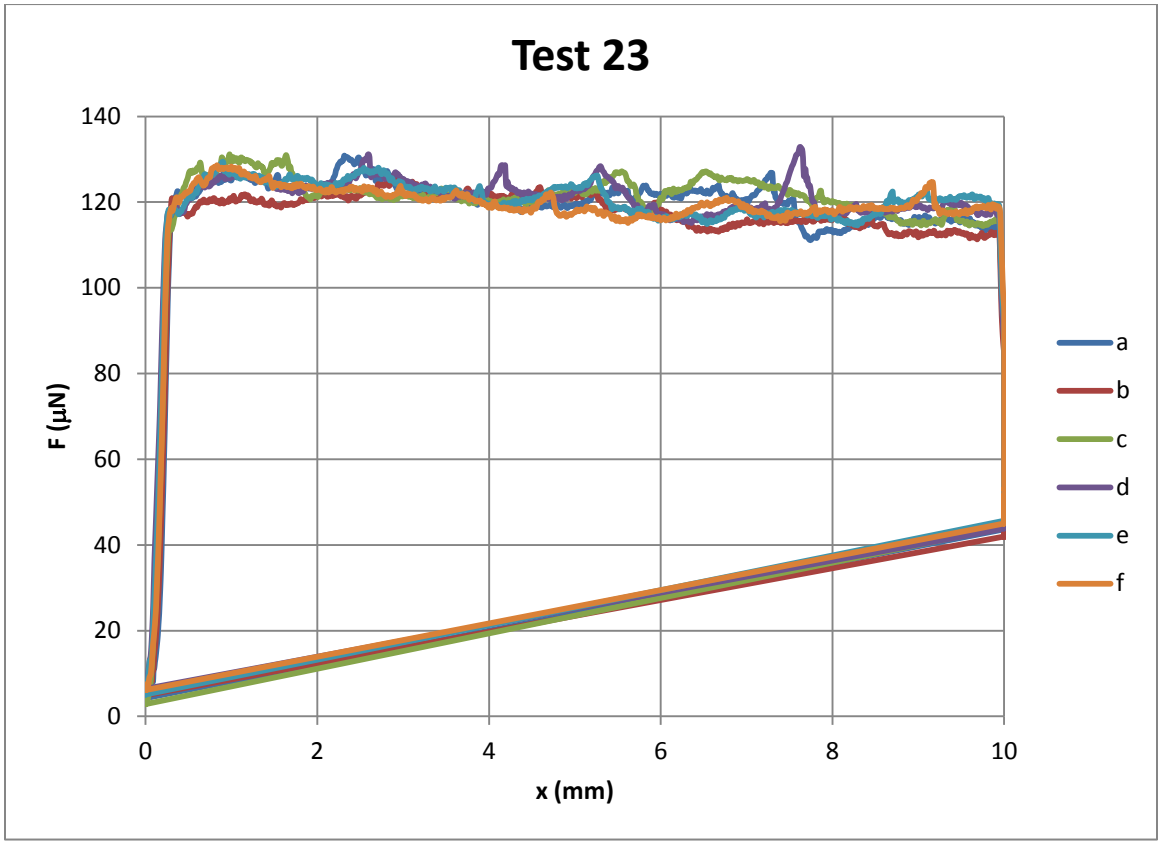

TEST 24

Run	-	avg	std	a	b	c	d	e
h	mm	1.25	0.00	1.25	1.25	1.25	1.25	1.25
w	mm	9.00	0.00	9.00	9.00	9.00	9.00	9.00
l	mm	4.50	0.00	4.50	4.50	4.50	4.50	4.50
U	mm/s	4.321	0.003	4.316	4.320	4.323	4.323	4.325
F_{break}	µN	114.8	5.8	123.4	118.6	118.3	119.0	118.4
F_{dyn}	µN	130.6	8.7	137.4	140.5	139.2	135.5	132.5
F_{max}	µN	144.9	12.6	154.6	169.1	153.4	151.7	143.6
k	µN/mm	742	232	657	623	698	663	708
r	-	0.998	0.003	0.999	0.999	0.999	0.998	0.989

Run	-	f	g	h	i	j
h	mm	1.25	1.25	1.25	1.25	1.25
w	mm	9.00	9.00	9.00	9.00	9.00
l	mm	4.50	4.50	4.50	4.50	4.50
U	mm/s	4.327	4.318	4.319	4.320	4.323
F_{break}	µN	107.5	111.2	112.8	104.6	114.8
F_{dyn}	µN	128.4	122.6	117.7	117.3	135.2
F_{max}	µN	136.8	133.8	129.2	130.9	145.4
k	µN/mm	578	751	721	1385	635
r	-	0.998	0.999	0.999	1.000	0.995

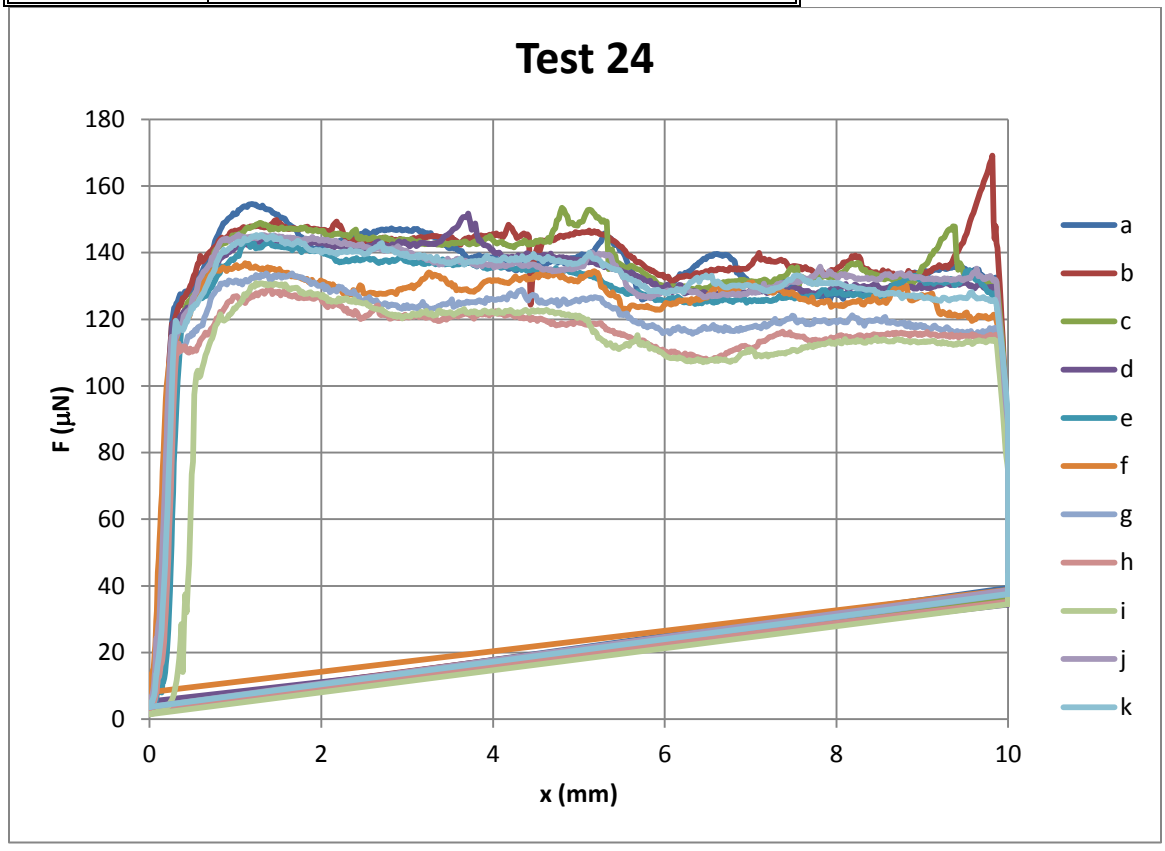

TEST 28

Run	-	avg	std	a	b	c	d	e	f
h	mm	1.25	0.00	1.25	1.25	1.25	1.25	1.25	1.25
w	mm	4.50	0.00	4.50	4.50	4.50	4.50	4.50	4.50
l	mm	4.50	0.00	4.50	4.50	4.50	4.50	4.50	4.50
U	mm/s	1.08	0.00	1.08	1.08	1.08	1.08	1.08	1.076
F_{break}	μN	71.79	1.72	71.60	73.23	73.44	72.11	71.69	68.6
F_{dyn}	μN	64.81	2.65	66.35	67.21	67.26	64.92	61.84	61.3
F_{max}	μN	71.79	1.72	71.60	73.23	73.44	72.11	71.69	68.6
k	μN/mm	430.17	32.15	422.45	440.01	474.73	453.39	399.84	391
r	-	1.00	0.00	1.00	1.00	1.00	1.00	1.00	1.000

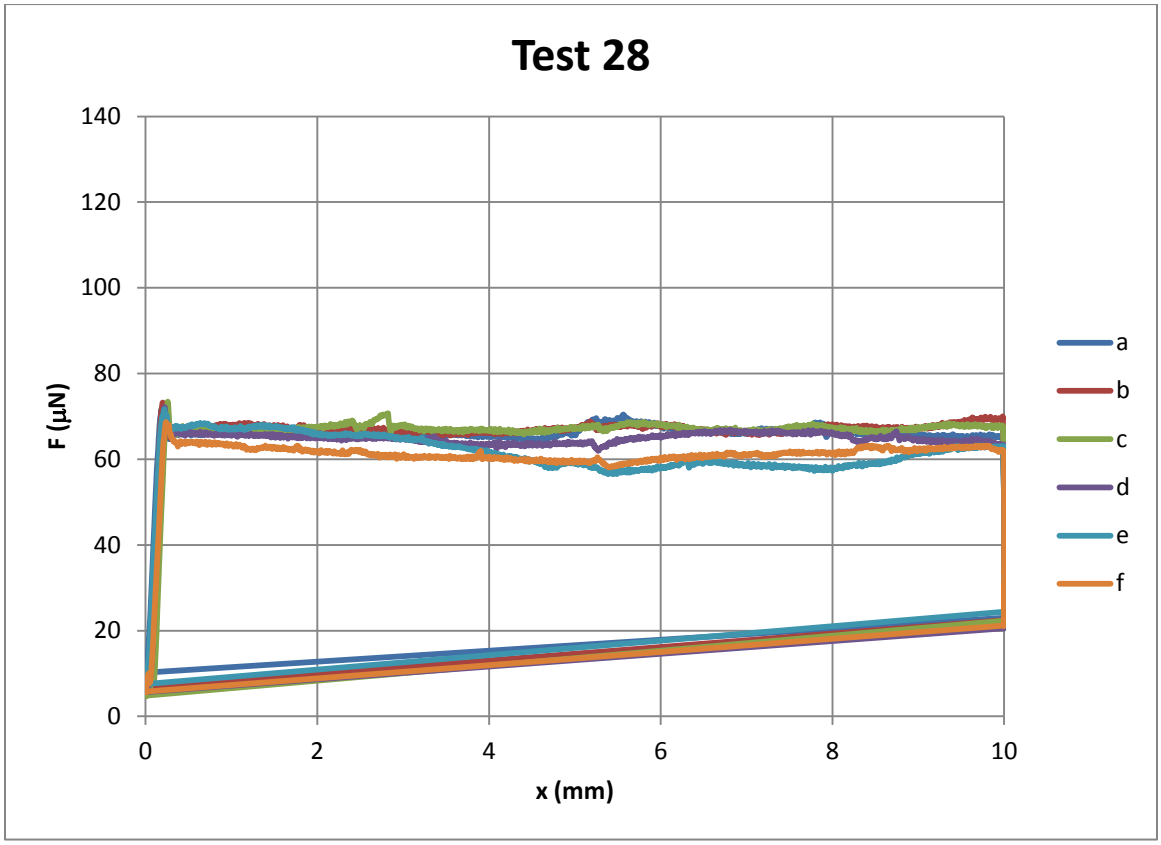

TEST 29

Run	-	avg	std	a	b	c	d	e
h	mm	1.25	0.00	1.25	1.25	1.25	1.25	1.25
w	mm	4.50	0.00	4.50	4.50	4.50	4.50	4.50
l	mm	4.50	0.00	4.50	4.50	4.50	4.50	4.50
U	mm/s	2.163	0.002	2.164	2.161	2.163	2.164	2.161
F_{break}	μN	69.3	2.8	72.6	72.1	66.7	67.3	67.9
F_{dyn}	μN	64.4	2.3	65.3	62.1	62.4	64.5	67.9
F_{max}	μN	77.2	6.8	84.3	72.1	70.8	74.0	84.8
k	μN/mm	426	28	445	394	406	424	461
r	-	0.997	0.003	0.999	0.995	0.992	0.999	1.000

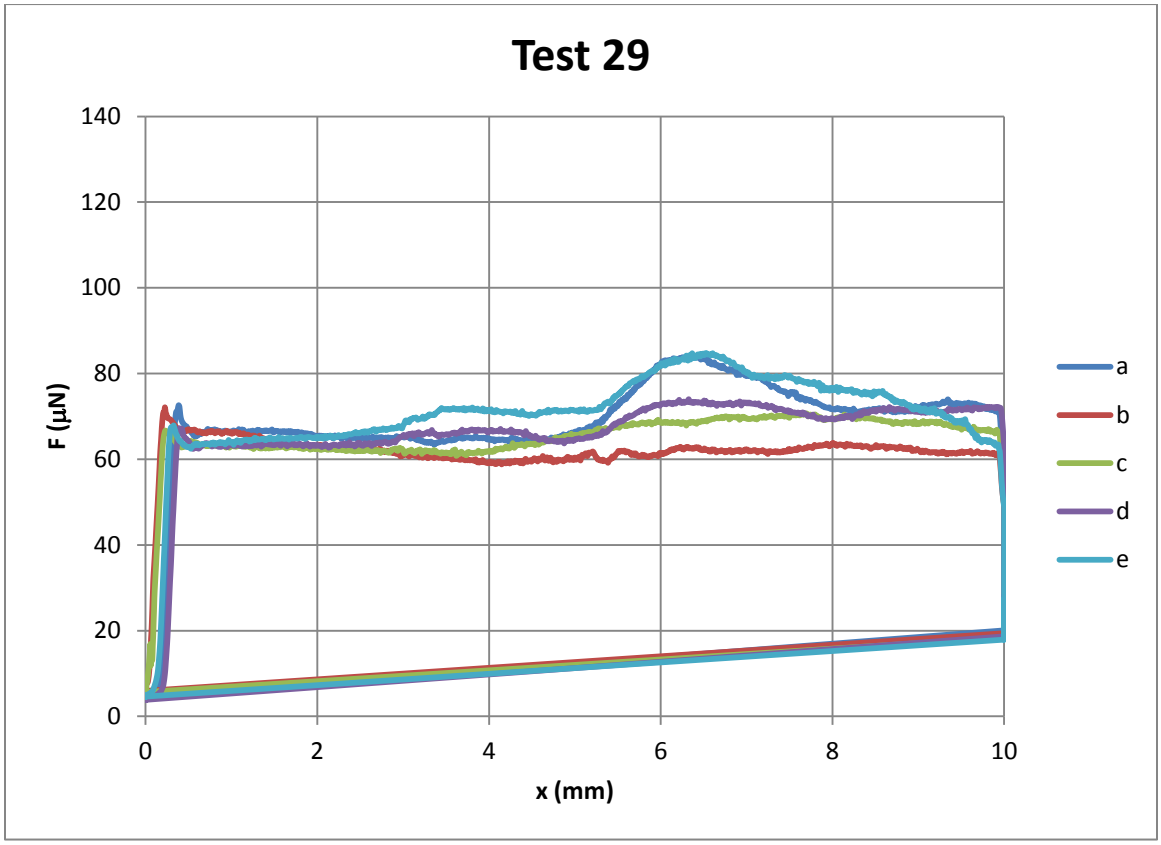

TEST 30

Run	-	avg	std	a	b	c	d	e	f	g
h	mm	1.25	0.00	1.25	1.25	1.25	1.25	1.25	1.25	1.25
w	mm	4.50	0.00	4.50	4.50	4.50	4.50	4.50	4.50	4.50
l	mm	4.50	0.00	4.50	4.50	4.50	4.50	4.50	4.50	4.50
U	mm/s	4.31	0.01	4.31	4.32	4.33	4.31	4.32	4.31	4.305
F_{break}	μN	59.88	1.46	61.98	60.38	59.70	60.65	60.35	58.57	57.5
F_{dyn}	μN	64.14	1.86	67.41	66.05	63.33	63.03	63.88	62.67	62.6
F_{max}	μN	74.49	9.08	76.73	80.34	82.66	85.92	66.18	64.27	65.3
k	μN/mm	359.79	52.32	425.93	304.69	396.22	414.87	339.80	297.96	339
r	-	0.97	0.02	0.94	0.97	0.98	1.00	0.97	0.98	0.983